Development of a Load-Managing Photovoltaic System Topology

by

Joseph A. Azzolini

A Dissertation Presented in Partial Fulfillment
of the Requirements for the Degree
Doctor of Philosophy

Approved June 2020 by the
Graduate Supervisory Committee:

Meng Tao, Chair
Bertan Bakkaloglu
Jiangchao Qin
Matthew J. Reno

ARIZONA STATE UNIVERSITY

August 2020

ABSTRACT

Nearly all solar photovoltaic (PV) systems are designed with maximum power point tracking (MPPT) functionality to maximize the utilization of available power from the PV array throughout the day. In conventional PV systems, the MPPT function is handled by a power electronic device, like a DC-AC inverter. However, given that most PV systems are designed to be grid-connected, there are several challenges for designing PV systems for DC-powered applications and off-grid applications. The first challenge is that all power electronic devices introduce some degree of power loss. Beyond the cost of the lost power, the upfront cost of power electronics also increases with the required power rating. Second, there are very few commercially available options for DC-DC converters that include MPPT functionality, and nearly all PV inverters are designed as "grid-following" devices, as opposed to "grid-forming" devices, meaning they cannot be used in off-grid applications.

To address the challenges of designing PV systems for high-power DC and off-grid applications, a load-managing photovoltaic (LMPV) system topology has been proposed. Instead of using power electronics, the LMPV system performs maximum power point tracking through load management. By implementing a load-management approach, the upfront costs and the power losses associated with the power electronics are avoided, both of which improve the economic viability of the PV system. This work introduces the concept of an LMPV system, provides in-depth analyses through both simulation and experimental validation, and explores several potential applications of the system, such as solar-powered commercial-scale electrolyzers for the production of hydrogen fuel or the production and purification of raw materials like caustic soda, copper, and zinc.

ACKNOWLEDGMENTS

First and foremost, I would like to express my sincerest gratitude to Dr. Meng Tao who has provided continuous support and guidance for my academic and professional development. In addition to serving as a trusted advisor and mentor, Dr. Tao cultivated an environment that encouraged independent thought, intellectual curiosity, and the exploration of new ideas. I am truly grateful to have had the opportunity to work with and learn from Dr. Tao over the years. I would also like to acknowledge all the past and present members of Dr. Tao's research group who have helped me in countless ways throughout my time at Arizona State University.

I would also like to thank all the staff members at the university that have helped me throughout my graduate studies. Specifically, I would like to thank Lynn Pratte for keeping me on track with my degree requirements and for providing support and guidance on everything from class selections to funding opportunities.

I would like to acknowledge the funding supplied by the ASU Dean's Fellowship, the ASU Fulton Fellowship, the ASU Graduate College Completion Fellowship, the ASU UGF Award, and the National Science Foundation (grant no. 1336297) which have supported my research.

Lastly, I would like to acknowledge NEL Hydrogen for providing the data required to accurately model their M200 hydrogen electrolyzer and for their collaboration efforts.

TABLE OF CONTENTS

Page

CHAPTER Page

LIST OF TABLES

Table Page

Table Page

LIST OF FIGURES

Figure Page

Figure Page

Figure Page

Figure Page

Figure Page

Figure Page

1 INTRODUCTION

Deriving electricity from renewable sources, like solar PV systems, provides significant environmental benefits over using fossil fuels. However, the cost of PV systems has been one of the largest roadblocks to its widespread adoption; as of 2018, solar PV generation accounted for just over 2% of global electricity production (EIA, 2019). This work introduces the concept of a load-managing photovoltaic (LMPV) system, and its accompanying load-matching maximum power point tracker (MPPT), which can be implemented to reduce the cost of PV electricity for many practical applications. Instead of managing the PV power using power electronics, the proposed system matches the loads to the PV array throughout the day to perform maximum power point tracking and voltage regulation. In other words, the system tracks the maximum power point without a conventional MPPT and controls the output voltage without a DC/DC converter, resulting in a reduction in upfront costs and an improvement in energy yield. The compounding benefits of cost reductions and energy yield improvements contribute to an overall reduction in the levelized cost of electricity (LCOE) for many applications. Furthermore, this system allows for a secondary power source to accommodate applications that require continuous access to power, eliminating the intermittency of the system.

The underlying theory of the LMPV system is introduced in Chapter 3. A model of the LMPV system was developed and simulated in MATLAB to highlight the conceptual benefits of the system and explore the various parameters that affect the performance of the system. The LMPV system, with a photodetector-based load-matching controller, was

then constructed in hardware and multiple experiments were conducted to investigate the practical challenges of the system.

Based on the conclusions drawn from the simulation and hardware results in Chapter 3, improvements were made to the implementation of the load-matching MPPT algorithm. Instead of relying on an estimation of maximum available PV power provided by a photodetector, the LMPV system was implemented with a feedback-based controller that measured the output power of the PV array before and after the load changed. This feedback-based LMPV system is introduced in Chapter 4. An updated model of the system was developed and simulated in Simulink to analyze and test the improved load-matching MPPT algorithm. Once the performance of the load-matching algorithm had been verified, the feedback-based LMPV system was constructed in hardware and multiple experiments were conducted to validate the performance of the system.

Several practical applications of the LMPV system are presented in Chapter 5. The application of hydrogen production through electrolysis was found to be highly compatible with the LMPV system and was explored in detail through additional modeling and simulations. Multiple opportunities for future work are summarized in Chapter 6 and the main conclusions from this work are discussed in Chapter 7.

2 BACKGROUND

Renewable energy resources have continued to play an increasing role in global energy production to reduce dependence on fossil fuel sources that contribute significantly to greenhouse gas emissions. Since 1970, global CO_2 emissions have increased by 90%, with fossil fuel combustion and industrial processes contributing to 78% of the total greenhouse gas emissions increase from 1970 to 2011 (Boden, Andres *et al.*, 2017). To combat the environmental impacts of using fossil fuels, energy infrastructures around the world have started to incorporate an increasing amount of renewable energy to satisfy demand. In 2018, 28% of global electricity was generated from renewable energy resources, and of all the renewable energy sources, solar photovoltaic (PV) energy is expected to grow the fastest over the next 30 years (Bowman, 2019).

Cost is one of the main barriers to the widespread adoption of PV energy. In 2017, solar PV generators ($2,343/kW), on-shore wind energy ($1,647/kW), and natural gas generators ($920/kW) accounted for 97% of the total installed generation capacity in the U.S.; while solar PV was the most expensive of the three, it was the only generating source that experienced a decrease in costs from the previous year (Mey, 2019). As of 2018, the installed costs of PV systems in the U.S. were \$3.11/W_{AC} (\$2.70/W_{DC}) for residential systems, \$2.10/W_{AC} (\$1.83/W_{DC}) for commercial systems, \$1.44/W_{AC} (\$1.06/W_{DC}) for fixed-tilt utility-scale systems, and \$1.47/W_{AC} (\$1.13/W_{DC}) for one-axis-tracking utility-scale systems (Fu, Feldman *et al.*, 2018). In terms of hardware costs for installed PV systems, the inverter costs represent a significant percentage of the total system costs; the inverters are responsible for synchronizing the PV system with the electrical grid, performing maximum power point tracking, and power conditioning. As the cost of PV

modules decreases, the cost of power electronics becomes more important, which can account for 8-12% of the total lifetime PV system cost (Nagarajan, Thiagarajan *et al.*, 2019).

For the cost of solar PV energy to continue to decline, all aspects of the PV system should be analyzed. Some of the main drivers of the recent cost reductions for PV energy include increased module efficiencies, reduced inverter prices, and reduced soft costs, such as permitting and interconnection costs (Fu, Feldman *et al.*, 2018). Specifically, the reliability of power electronics has shown to be a key price driver. While PV modules typically have long lifetimes with warranties up to 30 years, the reliability of inverters has not been up to par. One study found that over 27 months, inverter failures accounted for 36% of lost energy compared to just 5% attributed to PV module failures (Golnas, 2013).

In addition to the upfront costs, PV inverters also represent a source of power loss and power under-utilization. The efficiency of an inverter is a function of the input power and voltage, and while PV inverters typically have peak efficiencies in the range of 95-98%, their weighted efficiencies over a range of different operating conditions can be considerably lower (Pearsall, 2017). In general, PV inverters are undersized compared to the DC rating of the PV array, i.e., the DC/AC ratio of PV systems is typically greater than 1, which results in clipping losses anytime the PV array output power exceeds the inverter rating. PV inverters also require a certain level of DC power from the PV array before they turn on, resulting in an under-utilization of available PV power in the early mornings and late afternoons.

PV system costs can also be reduced by analyzing the end-use applications. While the majority of PV systems are grid-connected and thus require an inverter, many DC applications can be powered by PV systems without the need for an inverter. However, nearly all PV systems require an MPPT to extract the maximum amount of energy from the PV array throughout the day. In conventional PV systems, the MPPT function is handled by a power electronic device, like a DC-AC inverter (Santhoshi, Sundaram *et al.*, 2019). However, given that most PV systems are designed to be grid-connected, there are several challenges for designing PV systems for DC-powered applications and off-grid applications. The first challenge is that all power electronic devices introduce some degree of power loss; most PV inverters have peak efficiencies of 95% to 98% (Pearsall, 2017). Beyond the cost of the lost power, the upfront cost of power electronics also increases with the required power rating. Wide bandgap power electronics have the potential to drive down the cost for high-power applications, but currently only make up 1% of the market (Armstrong, Das *et al.*, 2016). Second, there are very few commercially available options for DC-DC converters that include MPPT functionality, especially at higher power ratings, and nearly all PV inverters are designed as "grid-following" devices, as opposed to "grid-forming" devices, meaning they cannot be used in off-grid applications (Pattabiraman, Lasseter *et al.*, 2018). To address the challenges of designing PV systems for high-power DC and off-grid applications, an LMPV can be implemented to provide MPPT capability through a load-matching algorithm that does not require any power electronics.

The following subsections highlight the various MPPT algorithms that have been proposed in the literature, as well as the potential for improvements to direct-coupled PV systems by incorporating a load-matching MPPT controller.

2.1 Maximum Power Point Tracking

The MPPT function for PV systems is typically implemented as a control loop within the DC stage of the inverter, or within DC/DC converter for DC applications. Figure 2.1 shows the current-voltage (I-V) and power-voltage (P-V) curves of a typical PV module under a certain irradiance level and operating temperature (Ram, Babu *et al.*, 2017), where only one operating point represents the maximum power point (MPP) of the module. Therefore, the MPPT is responsible for making sure the PV system operates at this point as the atmospheric conditions vary throughout the day.

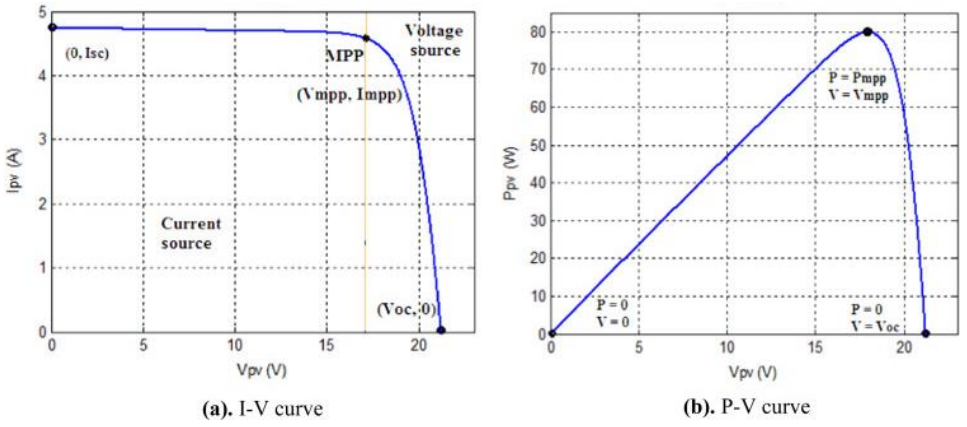

(a). I-V curve **(b).** P-V curve

Figure 2.1. Current-voltage and Power-voltage Curves of a PV Module (Ram, Babu *et al.*, 2017).

The need for including an MPPT in PV systems has been well documented in the existing literature, and many different MPPT algorithms have been proposed and implemented. The two most popular methods for conventional MPPT include the perturb and observe (P&O) method (Wasynezuk, 1983), and the incremental conductance method (Hussein, Muta *et al.*, 1995). The P&O method operates by continuously changing the operating point of the PV array and monitoring the change in output PV power; when a

change in operating point increases the output PV power, the algorithm continues to change the operating point in the same direction until the PV power decreases (Wasynezuk, 1983). This method results in a continuous oscillation of the PV array operating point around the MPP. In contrast, the incremental conductance method measures the change in power compared to the change in voltage (*dP/dV*); when the value of $dP/dV = 0$, the MPP has been found and thus no oscillations will be observed around the MPP (Hussein, Muta *et al.*, 1995). An improved approach to the incremental conductance algorithm, proposed in (Yeong-Chau, Tsorng-Juu *et al.*, 2001), incorporated the instantaneous conductance to track the MPP more accurately during rapid changes in atmospheric conditions.

Many other MPPT algorithms have also been proposed. An improved P&O algorithm was proposed in (Ahmed & Salam, 2015) that enhanced the steady-state performance and minimized the probability of losing tracking direction which resulted in an average energy yield increase of 2%. In (Radjai, Rahmani *et al.*, 2014), the use of a fuzzy logic estimator was implemented that reduced the error between the instantaneous and incremental conductance, resulting in improved steady-state and dynamic performance as well as the efficiency. Soft-computing techniques have also been applied to improve the performance of MPPT algorithms due to their high reliability and fast convergence for solving non-linear problems. In (Syafaruddin, Karatepe *et al.*, 2009), an artificial neural network with three-layer feed-forward was proposed to address the challenge of tracking the global MPP under partially shaded conditions. Many genetic algorithms have also been explored and applied to the MPPT problem, such as using particle swarm optimization (Daraban, Petreus *et al.*, 2014), ant colony optimization (Jiang, Maskell *et al.*, 2013), firefly optimization (Sundareswaran, Peddapati *et al.*, 2014), etc.

Each class of MPPT algorithms has several benefits and shortcomings, as outlined in (Ram, Babu *et al.*, 2017). The P&O method is simple and straightforward to implement but result in oscillations around the MPP and are undesirable in dynamic weather conditions due to their tracking speed. Increment conductance algorithms are simple, robust, and reliable but cannot guarantee optimal tracking under partial shading conditions. Artificial neural network approaches require significant computational resources and are therefore preferred in hybrid algorithms. Genetic algorithms also require notable computational resources but often converge very quickly and accurately.

The commonality amongst each class of MPPT algorithms discussed above is that they are all implemented through power electronics. While power electronics provide a great deal of flexibility for PV systems, they represent a significant cost (4-5% of the total installed cost of the system) and introduce power losses and additional points of failure into the system. One study, conducted by Sandia National Laboratories, tracked 244 PV across four different portfolios and found that inverters accounted for over 76% of the total recorded faults and failures (Klise, Lavrova *et al.*, 2018).

For DC applications, instead of using power electronics, the MPPT algorithm can be implemented by adjusting the load that is connected to the PV array throughout the day, i.e., a load-matching MPPT algorithm. A PV system that incorporates a load-matching MPPT algorithm is henceforth referred to as a load-managing PV system, or LMPV system. Other studies have investigated the use of load matching for DC applications, but in those cases, only static load matching was used. For example, in (García-Valverde, Espinosa *et al.*, 2011), a polarization curve of a water electrolyzer was optimized to match

the expected maximum power points of a PV array, but once the design was completed, the load remained static. As of this writing, the general concept of dynamically changing the load to track the MPP of a PV array (i.e., a load-matching MPPT) has not been explored in the existing literature.

The load-matching MPPT algorithm is similar to the P&O method, whereby the load connected to the PV is changed, or perturbed, and the effect on the output PV power is monitored; if increasing the load caused the power to increase, then more load is added, and vice versa. Being that the LMPV system does not contain any power electronic devices, the size of the perturbation is limited by the number of loads available to the system to manage. In other words, an LMPV system with hundreds of loads can make very small perturbations to the operating point of the PV array, similar to the conventional P&O algorithm, but when there are only a handful of loads being managed, the perturbations become much larger. Intuitively, the performance of the load-matching MPPT algorithm is expected to improve with the number of loads being managed by the system. A detailed description of the load-matching MPPT algorithm will be presented in a later chapter.

In general, the load-matching MPPT algorithm was modeled after the P&O algorithm based on its simplicity and proven performance. Given that the concept of an LMPV system is fairly unconventional, a simpler MPPT algorithm was chosen such that the underlying benefits of the system would be clear. It is expected that in future work, more sophisticated algorithms may be applied to the load-matching MPPT algorithm to improve its tracking speed, energy yield, and/or reliability under partial shading conditions.

2.2 Direct-coupled PV Systems

The simplest and lowest-cost PV system is the direct-coupled system, in which the load is directly connected to the PV array. By definition, direct-coupled systems do not contain an MPPT or any form of power management or conversion, thus the initial cost is low. Without an MPPT, the operating point of these systems can deviate considerably from the maximum power point, resulting in underutilization of the available PV power. When the load resistance is equal to the characteristic resistance of the PV array, the maximum available power from the array is extracted (Green, 1982). Changes in operating conditions shift the maximum power point as well as the characteristic resistance of the PV array. Therefore, the major challenge in designing efficient direct-coupled systems is to match the characteristic resistance of the PV array and the resistance of the load such that the system operates as close as possible to the maximum power point throughout any given day, which is the objective of the load-matching MPPT algorithm.

Many methods have been proposed to develop practical direct-coupled PV systems for various applications. One application for direct-coupled PV systems is water pumping, typically for irrigation purposes in remote areas. A method for predicting the long-term performance of direct-coupled PV pumping systems was proposed in (Kou, Klein *et al.*, 1998), while a review of performance studies of direct-coupled PV pumping systems was provided in (Chandel, Naik *et al.*, 2017). Without an MPPT the efficiency of these systems is greatly reduced. One study found that motor-pump efficiencies are in the range of 12–30% (Mokeddem, Midoun *et al.*, 2011). Another study found that efficiency can be improved by adjusting the PV array orientation, as compared to a fixed-tilt orientation (Kolhe, Joshi *et al.*, 2004). Several studies considered various PV array configurations to

optimize the performance of the direct-coupled pumping system. One study examined serial and parallel connections of the PV array to determine the optimal configuration to power a DC helical pump (Benghanem, Daffallah *et al.*, 2013). Another study concluded that the optimization of the array configuration increases the efficiency of the PV pumping system (Tiwari & Kalamkar, 2016). Wang et al (Wang, Ji *et al.*, 2016) found that a PV array with a section matched to the start-up characteristics of the pump and a section matched to the operational characteristics of the pump requires 25% fewer PV modules as compared to a conventional array.

Another application of direct-coupled PV systems is the production of hydrogen through water electrolysis. Optimization of these systems typically involves finding the best match between the serial and parallel connections of water electrolyzers and PV modules. One study found that directly coupling a PV module to a proton exchange membrane (PEM) electrolyzer increases the solar to hydrogen efficiency to 12.4% as compared to 6% in previous studies (Gibson & Kelly, 2008). Clarke et al (Clarke, Giddey *et al.*, 2009) achieved an energy transfer efficiency in a PV-driven PEM electrolyzer that is close to the theoretical maximum under perfect maximum power point matching conditions. Another study showed that the optimal sizing of a PV-driven electrolyzer can achieve a power transfer efficiency of up to 99% (Atlam, Barbir *et al.*, 2011). Garcia-Valverde et al (García-Valverde, Espinosa *et al.*, 2011) proposed a method for optimal sizing by fitting a normalized polarization curve to a cloud of expected maximum power points. Maroufmashat et al (Maroufmashat, Sayedin *et al.*, 2014) applied an imperialist competitive algorithm for multi-objective optimization that minimizes energy loss and maximizes hydrogen production. Sayedin et al (Sayedin, Maroufmashat *et al.*, 2016)

considered the effects of climate conditions in their optimization of electrolyzer size in different cities. Adding a V-through concentrator to direct-coupled PV-driven electrolyzers was explored as well (Su, Ding *et al.*, 2016).

The commonality amongst all the direct-coupled systems discussed above is the lack of a control system. However, it is possible to adjust the operating point of the PV array without a conventional MPPT by controlling the loads connected to it. Maeda et al (Maeda, Ito *et al.*, 2012) proposed a control system for direct-coupled PV-driven electrolyzers that adjusts the number of electrolyzers connected in series to the PV array, showing the feasibility of adding control to direct-coupled PV systems. After a thorough literature review, no other studies have implemented a control system in direct-coupled PV systems. However, the concept of adjusting the loads to manipulate the operating point of a PV array, i.e., through a load-matching MPPT algorithm, can improve the efficiency in direct-coupled PV systems.

3 LMPV SYSTEM WITH PHOTODETECTOR-BASED CONTROL

This chapter describes an LMPV system with a photodetector-based control strategy, originally proposed in (Azzolini & Tao, 2018). Specifically, the concept of maximum power point tracking through load-matching is explained, which represents the fundamental basis for the LMPV system. To evaluate the proposed LMPV system, a model of the system was developed and implemented in MATLAB to simulate the system under a variety of practical scenarios. These simulations provided key insights into how the system operates and revealed which parameters of the system affected its efficiency. The simulation program also served as a design tool that was utilized to develop an experimental prototype of the LMPV system. The prototype system then served as experimental validation to the various simulation results.

3.1 Maximum Power Point Tracking Through Load-Matching

The load-matching MPPT function of the LMPV system is introduced in its simplest, most fundamental form, i.e., powering ohmic loads. An ohmic load is one that follows the Ohm's law, such as a resistor. While the proposed system can certainly be adapted to support many different types of loads, this simplification is made to highlight its conceptual benefits and tradeoffs. The load-line analysis in Figure 3.1 illustrates the principle of the maximum power point tracking through load-matching. Several current-voltage (I-V) curves of a commercial 60-cell silicon module are plotted at different levels of irradiance (200, 350, 500, 670, 800, and1000 W/m^2). The module has a peak power of 275 watts peak (W_p), an open-circuit voltage of 38 V and a short-circuit current of 9.45 A.

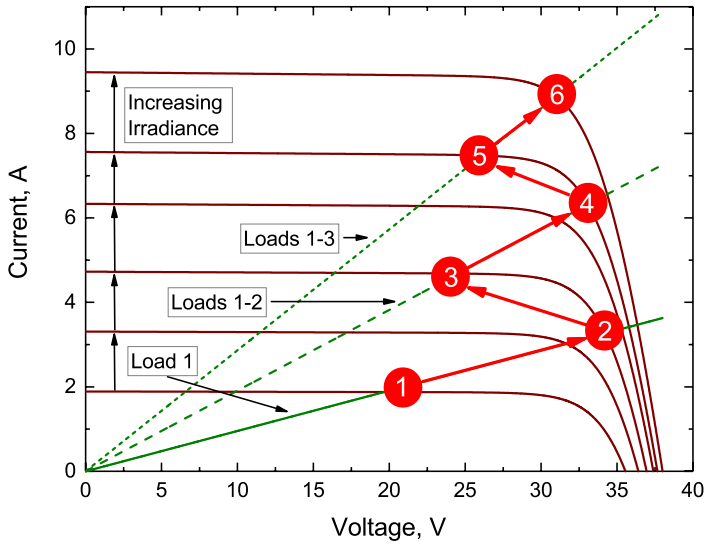

Figure 3.1. Load Line Analysis of an LMPV Aystem with 3 Equal-resistance Ohmic Loads.

To simplify the illustration of the MPPT functionality through load-matching, it is assumed that the system has only three ohmic loads with equal resistances. The ohmic loads appear as straight lines crossing the origin, where the slope of each line is equal to the reciprocal of the combined resistance of the connected loads. The three load lines in Figure 3.1 represent one load, two loads in parallel, and three loads in parallel connected to the PV array and the system can only operate along these straight lines. As the irradiance increases throughout the morning, the I-V curve gradually shifts up.

In Figure 3.1, the first load is connected to the PV array at point 1. The Load 1 line intersects the I-V curve to the left of the maximum power point, indicating that the resistance of the load is less than the characteristic resistance of the PV array at that moment. As the irradiance increases, the characteristic resistance of the PV array decreases. Meanwhile, the operating point of the system moves along the Load 1 line and passes through the maximum power point until it reaches point 2. At this moment, the load

resistance is greater than the characteristic resistance of the PV array. The system switches from point 2 to point 3 by connecting load 2 in parallel with load 1, cutting the load resistance in half. This critical point is referred to as a switch point (SP). The optimal switch point to maximize the utilization efficiency of the available PV power occurs when the power at point 3 is equal to that at point 2. The system will then operate along the Loads 1-2 line until it reaches the next switch point, and so on. In the afternoon, this process will happen in reverse as the irradiance decreases.

In Figure 3.1, the operating voltage of the system varies widely between point 1 and point 2 for one load, between point 3 and point 4 for two loads, and between point 5 and point 6 for three loads. The voltage variation is larger for fewer connected loads. The voltage variation can be limited by adjusting the SP settings, but the tradeoff is a reduced energy yield. In Figure 3.1, point 1 and point 3 can be delayed to higher voltages to reduce the voltage variations for one and two loads. The concept of voltage regulation is introduced to restrict how much the operating voltage can vary both above and below the maximum power output voltage. For example, if the voltage at maximum power output was 100 V, the system would only be allowed to operate between 90–110 V for a voltage regulation of ±10%. The relationship between voltage regulation and energy yield will be discussed in more detail in a later section.

In an LMPV system, the PV power is delivered directly to the loads through the relays, i.e., without going through any power management or conversion devices. There are two sources of power loss in this system, the conduction loss in the relays and the power required to run the controller and relays; the conduction losses in relays are generally small

as compared to the losses in power management or conversion devices because the number of switching events is much lower. The power consumed by the controller and relays is on the order of hundreds of milliamperes. So, for a commercial-scale PV system of 50 kilowatts peak (kW_p), the power lost to the relays and controller is negligible.

A major difference between the LMPV system and a conventional PV system is that it has multiple loads to manage, not just one load. Each combination of connected loads represents a moment during a day at which the load resistance is perfectly matched to the characteristic resistance of the PV array. Intuitively, the larger the number of loads, the more potential operating points the system has, resulting in an improved energy yield. As more loads are connected in parallel, their combined resistance is reduced, which continues to match the characteristic resistance of the PV array as the irradiance increases. A previous study implemented a similar strategy in which the number of loads (series-connected electrolyzers in that case) was modified (Maeda, Ito *et al.*, 2012). However, while the control objective in that study was not to perform maximum power point tracking, it does provide evidence that the operating point of the PV array can be modified by changing the load connected to it.

The controllable parameters for the LMPV system include the number of loads, resistance of each load, and switch point for each load. The effect of the number of loads and switch point is quantified through simulation in this chapter. The resistances of the loads were chosen to match the maximum power output of the PV array under standard test conditions (STC) with the combined power demand of all the loads in the system for a maximum utilization efficiency. If a single load is to match the maximum power output of

a PV array under STC, its resistance must be equal to the characteristic resistance (R_{CH}) of the PV array at the maximum power output:

$$R_{CH} = \frac{V_{MP}}{I_{MP}} \quad (1)$$

where V_{MP} and I_{MP} are the voltage and current at maximum power point under STC irradiance. It follows that for a system with n parallel loads of an equal resistance R_L, the resistance of each load would be:

$$R_{PerLoad} = R_{CH} \times n \quad (2)$$

If all n loads have the same resistance value, this equation ensures that their combined resistance is equal to the characteristic resistance of the PV array under STC irradiance. In practice, the value of the highest irradiance level may be available from historical data at the installed location. In this paper, the STC value of 1,000 W/m^2 irradiance is used, for which the values for V_{MP} and I_{MP} are readily available from PV module manufacturers.

3.2 Photodetector-Based Control

The load-matching MPPT algorithm for an LMPV system can be implemented in various ways. In this chapter, the load-matching MPPT algorithm relies on an estimation of maximum available PV power through the use of a photodetector circuit. A basic, stand-alone LMPV system is shown in Figure 3.2. The components of the stand-alone LMPV system include a PV array, a photodetector, a controller, a set of relays, and several DC loads. In Figure 3.2, there are five DC loads available to the system. The photodetector is installed near the PV array and it is used to estimate the instantaneous maximum available PV power, given the approximately linear relationship between the short-circuit current

and maximum power point of the PV array. The controller determines the number of loads that can be driven by the available PV power based on the information provided by the photodetector and then connects that number of loads to the PV array through the relays. Changes in available PV power caused by changes in operating conditions throughout a day result in the system adjusting the number of loads connected to the PV array. For example, in Figure 3.2, the controller determined that there was enough power to support the first 4 loads, while the fifth load remained disconnected until PV power increased. Overall, this system utilizes the maximum available PV power without a conventional MPPT.

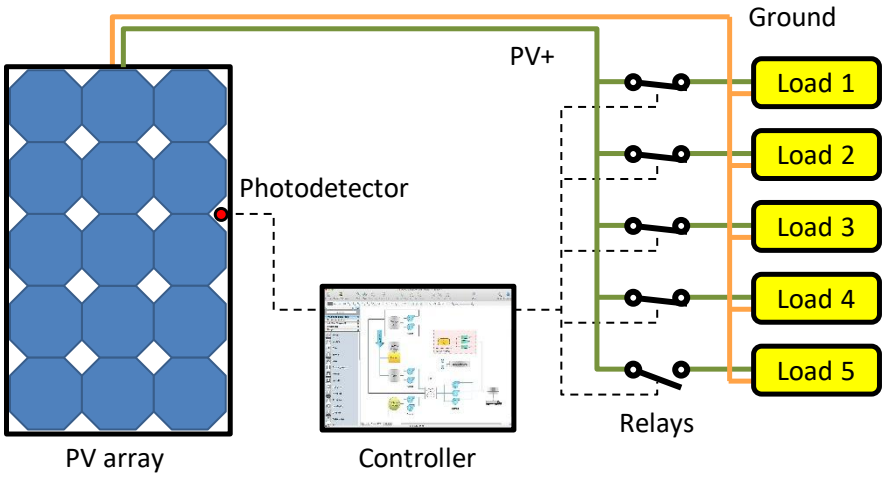

Figure 3.2. Stand-alone LMPV System with 5 DC Loads.

3.3 LMPV Simulation Program

A simulation program for the load-managing system in Figure 3.2 was developed in MATLAB. The simulation program can model a PV array of any size and a load-managing system with any number of loads. A cosine function with its amplitude set equal to the maximum power output of the PV array provides the maximum available PV power

on a sunny day; an incident angle of zero represents solar noon. In the simulation, all loads are assumed to be ohmic, i.e., they have linear I-V relations. The resistances of the loads satisfy (1) and (2), ensuring perfect power matching in the simulation at solar noon. The simulation program calculates all the possible operating points of the system throughout a day. With that information, the program determines the optimal switch points, variations in operating voltage, and daily utilization efficiency of the system.

The module specifications from the datasheet of a commercial 60-cell silicon module under STC were used to calculate the I-V curves over a range of irradiance levels, using the PV_LIB toolbox developed at Sandia National Laboratories (Stein, 2012). The module has a peak power of 275 W_p, an open-circuit voltage of 38 V, a short-circuit current of 9.45 A, a series resistance of 0.276 Ω, and a shunt resistance of 301.58 Ω. The effect of temperature on the PV module was accounted for by adjusting the operating temperature in simulation. Although the simulation employed a one-module PV array, larger PV arrays can also be simulated in the program by modeling any number of connected modules in series and/or parallel.

3.3.1 Simulated LMPV System with 4 Loads

The simulation program and PV module described in Chapter 3.3 was used to analyze the behavior of the LMPV system under several scenarios, such as changing the number of loads available to the system. All simulations assumed that there were no restrictions on the voltage applied to the loads, such that the energy extracted from the PV

module was maximized. The effects of incorporating voltage restrictions will be discussed in a later section.

First, a simulation was conducted with four loads, where the combined resistance of all loads in parallel is equal to the characteristic resistance (R_{CH}) at solar noon, using (1) and (2). The results from this simulation are presented in Figure 3.3, in which the four curves represent one, two, three, and four loads connected in parallel throughout the day. In other words, the "Load 1" curve represents the operating points if only one load was connected to the PV module for the entire day, and so on. The "Load 1" curve extracted the maximum power from the PV array in the early morning and late afternoon but was significantly lower than the other curves in the middle of the day. Therefore, by changing the number of loads connected to the PV module throughout the day, the maximum power point can be tracked, i.e., the load-matching controller provides the MPPT function as opposed to using a power electronic device.

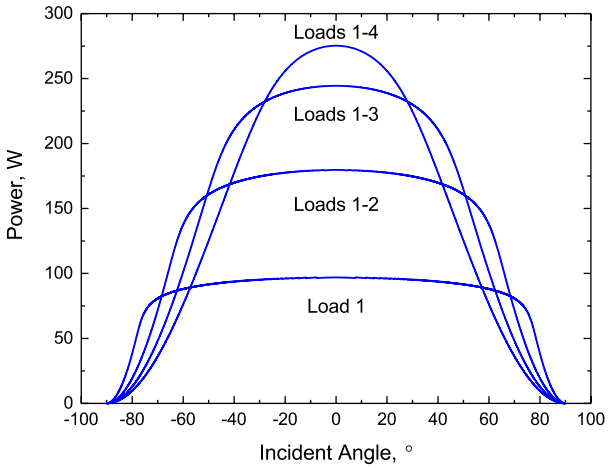

Figure 3.3. All Possible Operating Points of the LMPV System with 4 Loads.

By finding the curve that provided the maximum power for each point on the x-axis, the optimal performance of the LMPV system can be identified and compared to the maximum available power from the PV module, as shown in Figure 3.4. The points at which the number of loads changes to track the maximum power point are referred to as switch points (SPs); the SPs are circled in red in Figure 3.4 and are numbered according to how many loads are connected in parallel.

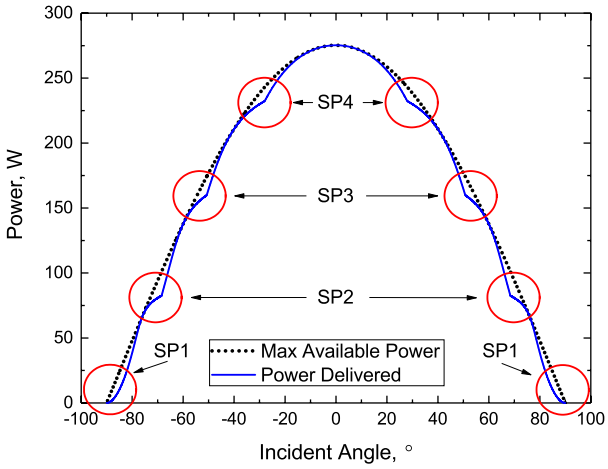

Figure 3.4. Optimal Power Delivered by the LMPV System with 4 Loads.

By comparing the energy delivered by the LMPV system to the maximum available energy from the PV array, the energy yield of the LMPV system can be determined:

$$Energy\ Yield\ (\%) = \frac{\int Energy\ Delivered}{\int Energy\ Available} \times 100\% \quad (3)$$

For the simulation results in Figure 3.4, the energy yield of the system was 97.12%. In Figure 3.4, the regions in which the maximum available power was greater than the power delivered represent the energy from the PV array that was underutilized by the LMPV system. These regions generally appear around the SPs, as those points represent the

transition periods where the LMPV system must wait for enough power to be available to switch in the next load.

Being that the SP values are associated with regions of underutilization of available power, they are an integral part of designing an efficient LMPV system. One of the benefits of the LMPV simulation program is that the optimal SP values can be determined and then programmed into the PLC of the prototype system. First, the SP values must be converted to voltage values corresponding to the output of the photodetector circuit. This conversion is achieved by dividing each simulated SP power values by the maximum power point at solar noon. Then, since the maximum photodetector output voltage at solar noon is 10 V, the SP power ratios can be translated to photodetector voltages by:

$$V_{SP} = \frac{P_{SP}}{P_{SolarNoon}} \times 10\ V \tag{4}$$

Once the SP values are converted to voltages, they can be programmed into the PLC which uses those values as thresholds for when the loads should be connected and disconnected from the PV array. For example, if SP2 is equal to 25% of the maximum PV power at solar noon, then the PLC would connect the second load in parallel to the first load when the photodetector output signal is above 2.5 V. The V_{SP} values calculated from Figure 3.4 are presented in the first row of Table 3.1.

Table 3.1. VSP Values for Figure 3.4 and Figure 3.6.

	V_{SP} Values (V)			
	SP1	***SP2***	***SP3***	***SP4***
Unregulated	0.00	3.67	6.29	8.80
Nominal ±12% Regulation	1.98	4.19	6.29	8.80

For the simulation in Figure 3.4, there were no restrictions placed on the voltages being applied to the loads, and the voltage was allowed to swing freely, as shown in the bottom plot of Figure 3.5. The exact voltage values for each combination of loads is presented in the "unregulated" section of Table 3.2, where the voltage fluctuated between 0 V and 33.93 V. In general, the voltage variation is much larger with fewer connected loads, i.e., in early mornings and late afternoons. For example, the voltage variation is from 0 V to 33.93 V for one load, but from 28.47 V to 31.00 V for four loads.

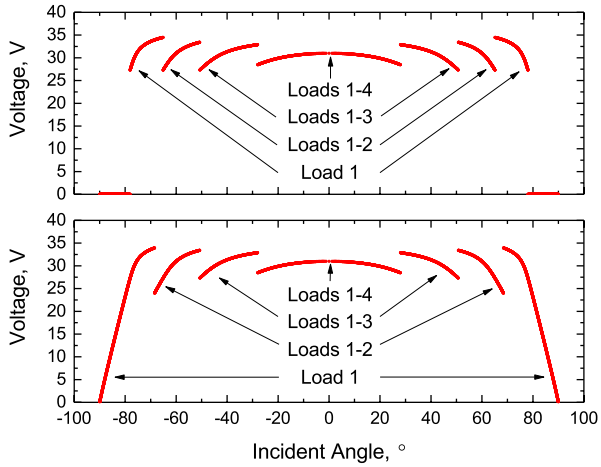

Figure 3.5. Operating Voltages of LMPV System with 4 Loads Both With (Top) and Without (Bottom) Regulation.

Table 3.2. Voltage Variations for an LMPV System With and Without Regulation.

	Loads			
	1	***1-2***	***1-3***	***1-4***
Unregulated				
Min (V)	0.00	24.00	27.28	28.47
Max (V)	33.93	33.41	32.88	31.00
Nominal ±12% Regulation				
Min (V)	27.28	27.28	27.28	28.47
Max (V)	34.48	33.41	32.88	31.00
Midrange (V)	30.88	30.35	30.08	29.74
Variation	±11.7%	±10.1%	±9.3%	±4.3%

For practical applications of an LMPV system, the voltage applied to the loads may be required to remain within certain limits. In these cases, the LMPV system can be designed to include voltage regulation. To reduce the voltage variation of the simulation results from Figure 3.4, a regulation of ±12% was imposed on the operating voltage by adjusting the SP settings. The value of ±12% regulation was the tightest constraint that could be applied to a system with just four loads without significantly deteriorating the energy yield. Table 3.1 includes the new SP settings that resulted in a voltage regulation of ±12%, revealing that SP1 and SP2 needed to be delayed, but SP3 and SP4 remained the same. The top plot of Figure 3.5 shows the new operating voltages for the regulated case, where the voltage variation for load 1 is greatly reduced. The exact voltage values are presented in Table 3.2 for the system under ±12% regulation. However, even though the voltage regulation was set to ±12%, the maximum voltage only reaches 11.2% above the maximum power output voltage. Therefore, voltage regulation mainly constrains the minimum operating voltage. The maximum voltage is 34.48 V and the minimum voltage

27.28 V in Table 2, resulting in a midrange voltage of 30.88 V for the regulated case and an actual voltage regulation of ±11.7% from the midrange value.

The power delivered to the loads by the LMPV system with ±12% voltage regulation is shown in Figure 3.6. Due to the voltage regulation, the first two SP values had to be delayed, which caused the regions of underutilization to increase and thus the energy yield decreased from 97.12% in the unregulated case to 95.49% with regulation. If a tighter voltage regulation was implemented, the energy yield would drop even further.

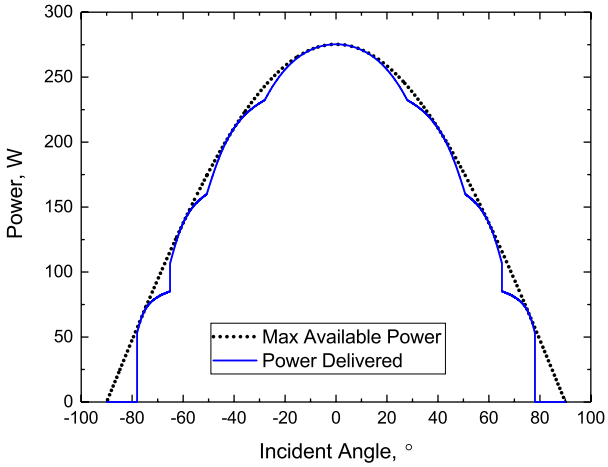

Figure 3.6. Power Delivered by the LMPV System with 4 Loads and ±12% Voltage Regulation.

3.3.2 Simulated LMPV System with 10 Loads

Similar analyses were performed on a system with ten available loads, in which the resistance of each load was adjusted according to (1) and (2). Figure 3.7 shows the power delivered by the LMPV system without any voltage regulation and Figure 3.8 shows the results of the same system with ±12% voltage regulation. The energy yield for the unregulated, 10-load system is 99.35% compared to 97.12% for the 4-load, unregulated

system. The ±12% regulation used in Figure 3.8 is the same as for the four-load case in Figure 3.6. In Figure 3.8, the energy yield drops slightly from 99.35% to 99.07% after including the voltage regulation, which is a less severe reduction than when voltage regulation was added to the LMPV system with only 4 loads.

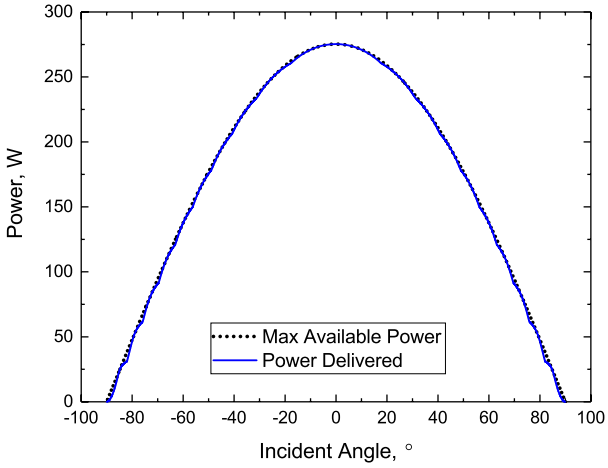

Figure 3.7. Power Delivered by an LMPV System with 10 Loads, Without Voltage Regulation.

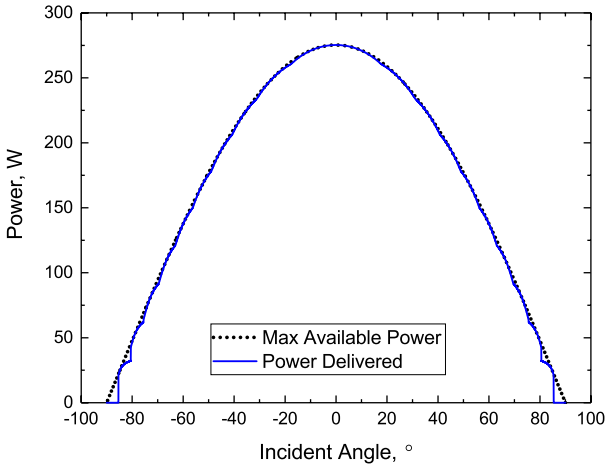

Figure 3.8. Power Delivered by an LMPV System with 10 Loads and with ±12% Voltage Regulation.

Figure 3.9 shows the voltages applied to the loads for the case of 10 available loads both with and without voltage regulation. Again, the main difference between the two plots of Figure 3.9 is the range of voltages applied to the loads in the early morning and late afternoon.

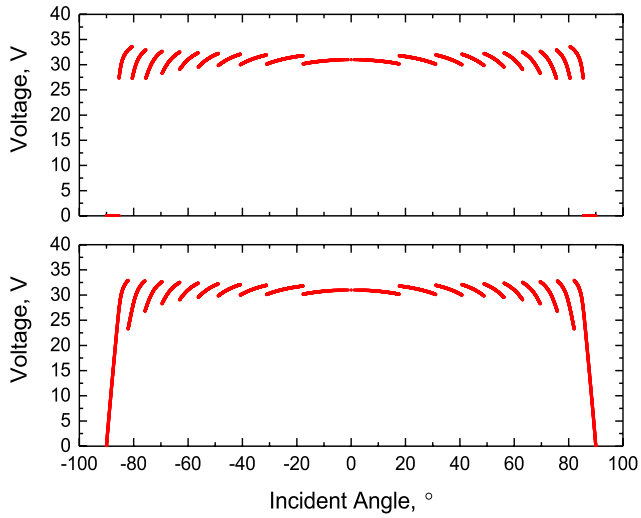

Figure 3.9. Operating Voltages of LMPV System with 10 loads Both With (Top) and Without (Bottom) Regulation.

Table 3.3 lists the ranges of operating voltage for the ten-load system without regulation and with ±12% nominal regulation. For the regulated case, the maximum voltage is 33.58 V and the minimum voltage is 27.28 V, resulting in a midrange voltage of 30.43 V and an actual voltage regulation of ±10.4% from the midrange value. It is noted that the voltage variation decreases with more connected loads, as shown in the last row of Table 3.3. Between Table 3.2 and Table 3.3, it can also be concluded that more loads in the system lead to smaller voltage variations.

Table 3.3. Voltage Variations for an LMPV System with 10 loads, With and Without Regulation.

	Loads									
	1	***1-2***	***1-3***	***1-4***	***1-5***	***1-6***	***1-7***	***1-8***	***1-9***	***1-10***
Unregulated										
Min (V)	0.00	23.27	26.77	28.27	29.07	29.53	29.82	30.00	30.11	30.16
Max (V)	32.90	32.79	32.64	32.49	32.35	32.21	32.07	31.93	31.79	31.00
Nominal ±12% Regulation										
Min (V)	27.30	27.28	27.29	28.27	29.07	29.53	29.82	30.00	30.11	30.16
Max (V)	33.58	32.92	32.64	32.49	32.35	32.21	32.07	31.93	31.79	31.00
Midrange (V)	30.44	30.10	29.97	30.38	30.71	30.87	30.95	30.97	30.95	30.58
Variation	±10.3%	±9.4%	±8.9%	±6.9%	±5.3%	±4.3%	±3.6%	±3.1%	±2.7%	±1.4%

3.3.3 Simulated LMPV System with Unequal Loads

Chapter 3.3.1 and Chapter 3.3.2 explored LMPV systems with different numbers of loads (both with and without voltage regulation), but in each case, the loads in the system always had equal resistance values to simplify the analyses and discussions. However, the only requirement is that when all the loads are connected in parallel, their combined resistance is equal to the characteristic resistance of the PV array under full irradiance, as in (1).

An additional simulation was performed to provide an example of the case in which the loads do not all have the same resistance. For this simulation, the first, second, and fourth loads were set to 17.45 Ω, while the third load was set to 8.73 Ω (roughly half the resistance of the other loads). Therefore, under full irradiance, the third load would consume roughly twice as much power as each of the other loads. Similar to Figure 3.3,

Figure 3.10 shows all of the possible operating points for the 4 different connections of loads: 1 load, first two loads in parallel, first 3 loads in parallel, and all four loads in parallel.

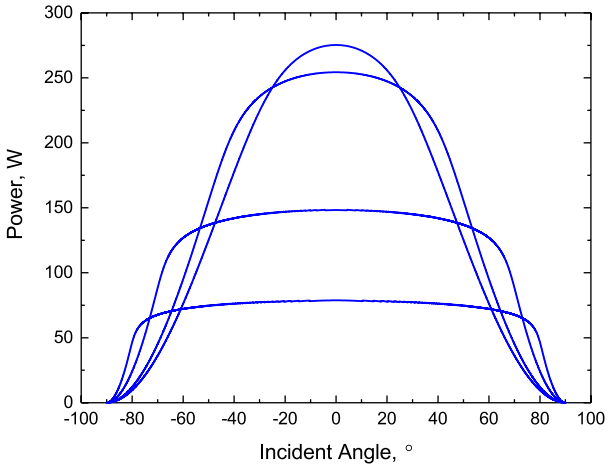

Figure 3.10. All Possible Operating Points of the LMPV System with 4 Loads, Where the 3rd Load is Half the Resistance of the Other Loads.

Since the third load is roughly half the resistance of the other loads, the section of Figure 3.10 with the first 3 loads connected in parallel appears much larger than the others, compared to Figure 3.3. Similar to Figure 3.4, the optimal operating points represent the maximum value of all of the load curves at each point on the x-axis, as shown in Figure 3.11. The energy yield for the simulation in Figure 3.11 was found to be 96.44%.

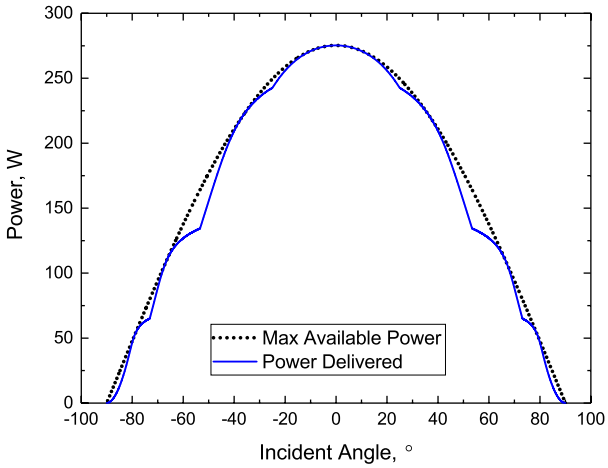

Figure 3.11. Optimal Power Delivered by the LMPV System with 4 Loads, Where the 3rd Load is Half the Resistance of the Other Loads.

3.3.4 Effect of System Parameters on Energy Yield

Overall, the energy yield for the 4-load case increased from 97.12% to 99.35% for the 10-load case. Intuitively, these results are in line with expectations because as the number of loads increases, there are more operating points to choose from for tracking the maximum power point throughout the day. Additional simulations were performed after adjusting the number of loads (as well as their resistance values) from 2 to 16 loads to further investigate the relationship between the number of loads and energy yield. The results from these simulations are presented in Figure 3.12, which shows the energy yield as a function of the number of loads in the system (without any voltage regulation).

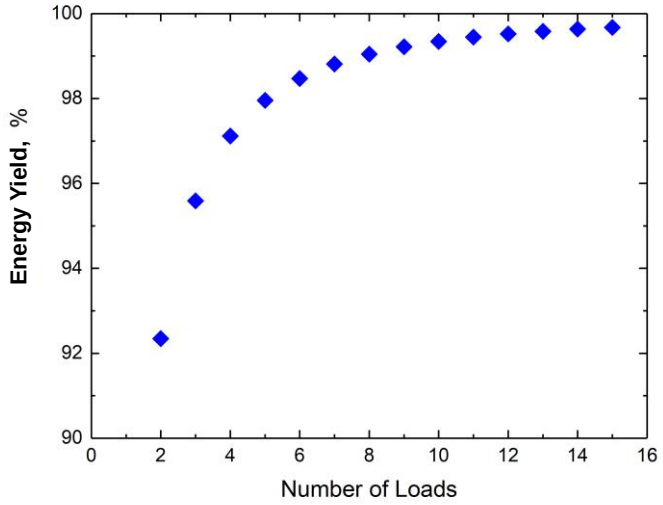

Figure 3.12. Effect of the Number of Loads on Energy Yield (Without Voltage Regulation).

The results in Figure 3.12 agree with a previous study conducted on a system with one ohmic load that found the energy yield to be 81.99% (Applebaum, 1987). The energy yield of the LMPV system exceeds 99% when managing just eight ohmic loads. For tens of ohmic loads, the energy yield is practically 100%. This relationship represents an incentive to scale up the system for an improved energy yield, i.e., by adding more loads, and demonstrates that load-matching significantly improves the energy yield for direct-coupled systems.

When the ±12% voltage regulation was added to the 4-load case, the energy yield dropped from 97.12% to 95.49%, i.e., an absolute reduction of 1.63%. However, the energy yield for the 10-load case only dropped from 99.35% to 99.07%, i.e., an absolute 0.28% drop, for the same ±12% voltage regulation. Therefore, voltage regulation has less of an effect on energy yield as the number of loads increases. This relationship was further explored by running a batch of simulations for four different scenarios: an LMPV system

with 5 loads, 10 loads, 20 loads, and 40 loads. For each of these scenarios, the voltage regulation was swept from ±12% down to 0.25%. To reiterate, a lower value of voltage regulation means a tighter limit on the voltages that can be applied to the loads. If none of the available operating points can satisfy the voltage requirement, then no loads are connected, which significantly reduces the energy yield. The results from these additional simulations are shown in Figure 3.13.

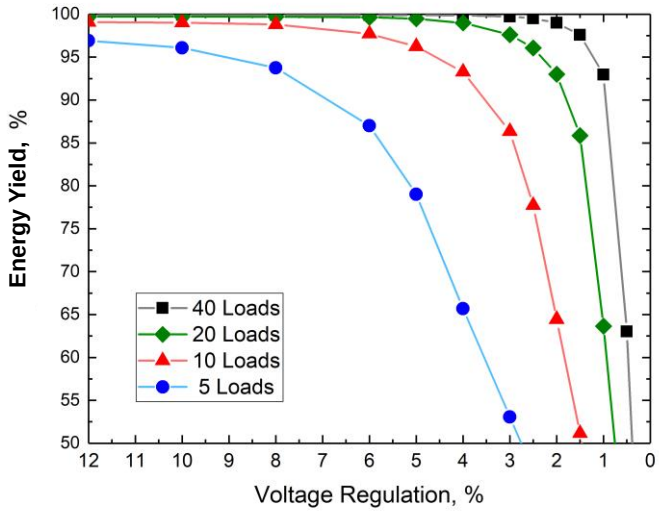

Figure 3.13. Effect of Voltage Regulation on Energy Yield for Four Different Scenarios of Loads.

Figure 3.13 confirms the hypothesis that placing a tighter constraint of the operating voltage of the LMPV system has a more pronounced effect when there are fewer loads in the system being managed. For example, when the LMPV system has 40 loads to manage, the energy yield approaches 100% even when the voltage is being regulated to ±3% of the maximum power point voltage, whereas the same degree of voltage regulation results in an energy yield of less than 55% when the system only has 5 loads available to manage. This relationship provides an additional incentive for large-scale implementations of

LMPV systems because as the number of loads increases, the energy yield is improved, and the voltage variations are reduced.

3.3.5 Discussion of Simulation Results

The simulation program developed for the LMPV system provided key insights into the system's performance. Specifically, several parameters were identified as being directly related to the energy yield of the LMPV system. First, the results revealed that the energy yield of the system improves as the number of loads increases. Each combination of loads provides a unique operating point on the I-V curve of the PV array. Therefore, as the number of potential operating points increases, the ability to track the maximum power point throughout the day improves. It was determined that an LMPV system with 8 available loads to manage provided enough possible operating points for the system to reach above a 99% energy yield.

In addition to performing maximum power point tracking, the simulation results supported the claim that the LMPV system can regulate its output voltage without using any power electronic devices. However, the degree to which the voltage can be regulated depends on the number of loads. Similar to the discussion on the LMPV system's MPPT functionality, the more loads the system had to manage provided more operating points for the voltage regulation functionality as well. As the number of loads increases, the LMPV system can regulate its output voltage more precisely, without sacrificing the system's energy yield.

The simulation program also served as a design tool for matching the loads to the PV array and for providing SP values. By simulating an LMPV system ahead of time, the SP values can be determined and programmed into the LMPV controller for actual implementations, facilitating the design process.

While the simulation program provided key insights into the fundamental principles of an LMPV system, there are still many areas in which this program can be improved. For example, the irradiance profile used as the input for generating the I-V curves of the PV array was a simple cosine function with a peak value of 1000 W/m^2. Ideally, the input irradiance profiles would correspond to actual clear-sky irradiance values at various locations that could be converted to the plane-of-array irradiance incident upon the PV array's orientation and actual location. Furthermore, actual irradiance measurements could be used to determine the performance of the LMPV system under more variable conditions. Similarly, the effects of temperature on the performance of the LMPV system could be further explored, being that a constant 25°C was used for these simulations. To accurately analyze the performance of the LMPV system under actual ambient conditions, more realistic temperature profiles could be used.

3.4 Experimental LMPV System

A proof-of-concept prototype of the basic, stand-alone load-managing PV system has been constructed. This system includes a 48-cell silicon module of 140 W_p, a photodetector, an Allen-Bradley Pico 1760-L18BWB-EX programmable logic controller (PLC) with six built-in relays, and six 50 W variable resistors as the loads. The module and photodetector are outdoors on the rooftop, while the rest of the system is indoors, as

pictured in Figure 3.14. The PLC with 6 built-in relays is circled in red, and the 6 variable resistor loads are circled in yellow. Data-logging digital multimeters take measurements of the voltage and total current of the connected loads, i.e., the power delivered to the loads, and the output voltage of the photodetector. Overall, this experimental setup allows for changes in the number of loads, resistance of each load, and switch point for each load.

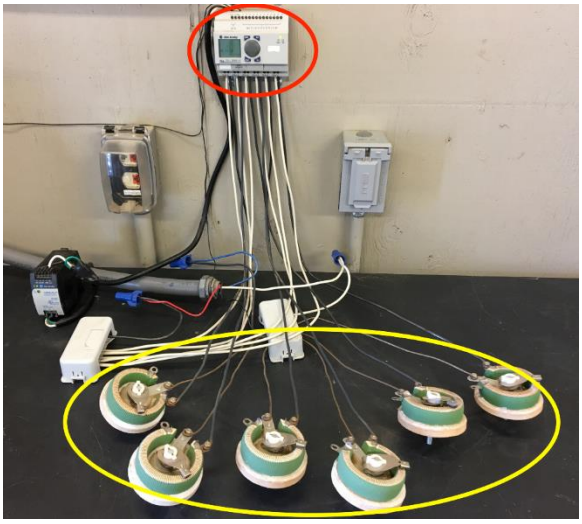

Figure 3.14. Experimental LMPV System, Where PLC with Built-in Relays is Circled in Red and Loads are Circled in Yellow, but the PV Module and Photodetector are not Pictured.

The photodetector is made up of a small silicon solar cell and a trans-impedance amplifier. The choice of a silicon solar cell as the photodetector ensures that the output of the photodetector is similar to the output of the silicon module. The trans-impedance amplifier circuit is shown in Figure 3.15, which measures the short-circuit current of the photodetector and converts it into a voltage signal of 0–10 V for the PLC. The feedback resistor, R_f, is adjusted so the output of the amplifier is 10 V under full irradiance.

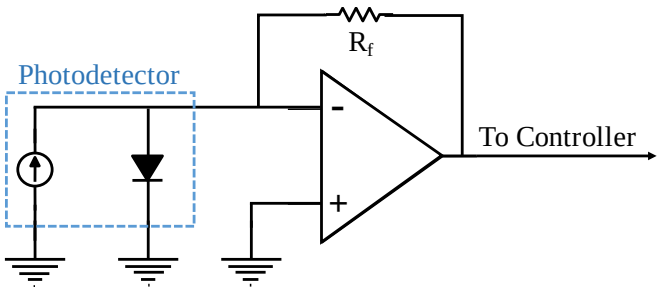

Figure 3.15. Photodetector Trans-impedance Amplifier Circuit.

Since what is measured is the short-circuit current and what is needed is the maximum available PV power, the relationship between short-circuit current and maximum power of the silicon solar cell was measured at different irradiance levels, as shown in Figure 3.16. The relationship is linear, with a Pearson correlation coefficient of 0.9967. Thus, short-circuit current can represent the maximum available PV power.

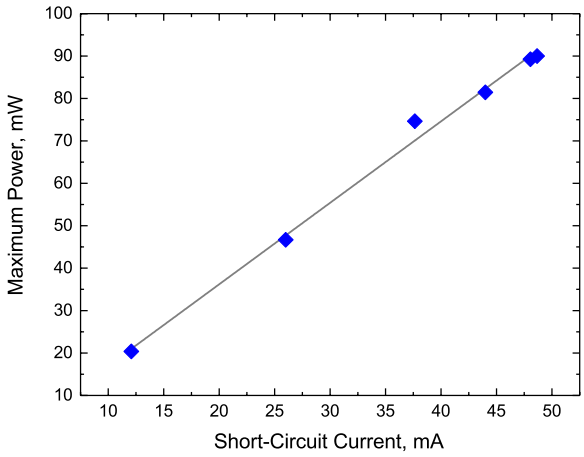

Figure 3.16. Photodetector Maximum Power vs. Short-circuit Current.

The measurements in Figure 3.16 were taken under constant temperature conditions. However, temperature does influence this relationship. In Figure 3.17, the relationship between short-circuit current and maximum power of a commercial 275 W, 60-cell silicon module was simulated for different temperatures. While the relationship was

always linear, the increasing temperatures reduced the power output of the PV module. Ideally, this behavior should be taken into account when designing an LMPV system. However, to simplify the design and analysis of the prototype LMPV system, no temperature correction was included.

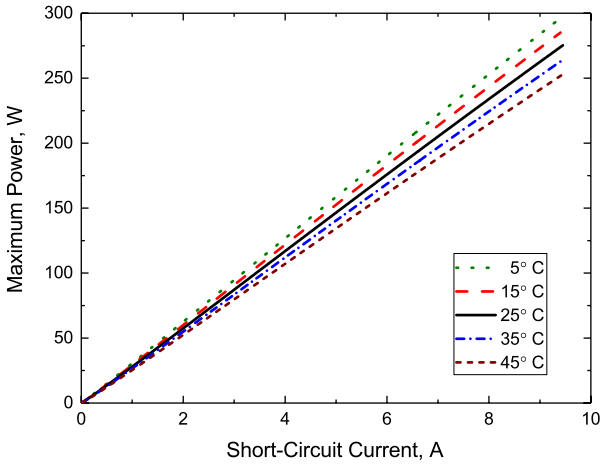

Figure 3.17. Simulated Effect of Temperature on Photodetector Measurements.

3.4.1 Experimental LMPV System with 4 Loads

For the first experiment of the prototype LMPV system, 4 loads were used with each load set to a resistance of 14.5 Ω, such that the combined resistance of the 4 loads in parallel was equal to 3.625 Ω. The SP values for the 4 combinations of loads are presented in Table 3.4. The power delivered to the loads during this experiment is shown in Figure 3.18, where each of the SPs is circled and numbered according to how many loads were connected to the PV array. The results in this figure follow the general shape of the simulated LMPV system with 4 loads of equal resistance from Figure 3.4, as expected.

Table 3.4. V_{SP} Values for Figure 3.18 and Figure 3.21.

	V_{SP} (V)			
	SP1	**SP2**	**SP3**	**SP4**
Figure 3.18	1.25	4.00	6.75	8.20
Figure 3.21	0.00	4.10	6.34	8.16

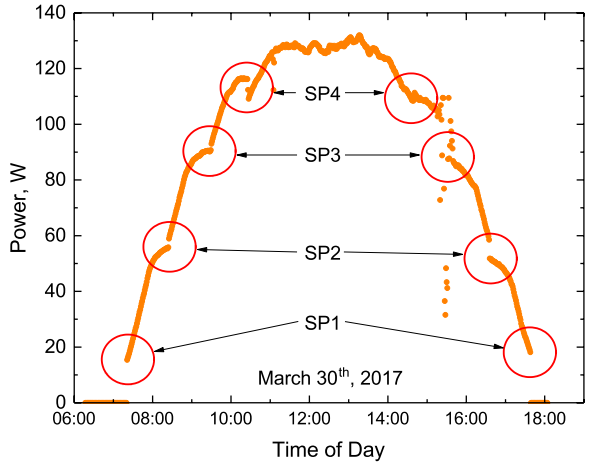

Figure 3.18. Power Delivered by Experimental LMPV System to 4 Loads of Equal Resistance on 3/30/17.

In Figure 3.18, the SP1 value was set to 1.25 V, which explains the jump in power around that switch point, since the photodetector voltage was below that threshold. As the solar irradiance increased in the morning, the PLC subsequently connected loads to the PV module, one by one, based on the voltage signal received from the photodetector, shown in Figure 3.19. A dip in power is observed near the first occurrence of SP4, which is attributed to a sub-optimal switch point setting. The PLC connected the 4th load when dictated to do so by the photodetector, but the drop in power means that it happened too

early. Optimal switch point settings result in a continuous power curve, like at SP2 and SP3. By noon, all four loads were powered by the PV module.

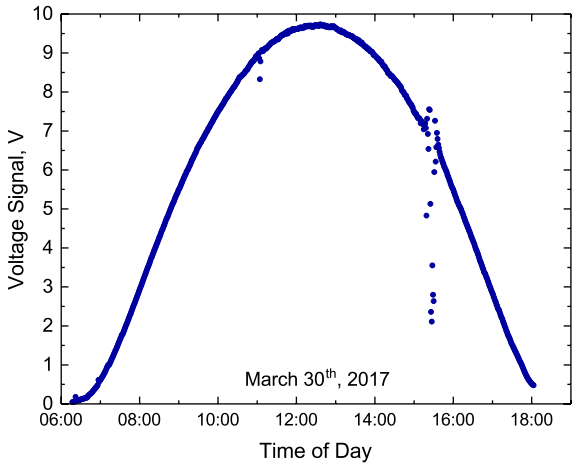

Figure 3.19. Photodetector Output Signal Corresponding to Figure 3.18.

Around midday, the power curve in Figure 3.18 is relatively flat. This behavior indicates there was a mismatch between the combined resistance of the four loads and the characteristic resistance of the PV module at noon. Ideally, the top of the power curve in Figure 3.18 would more closely resemble the shape of the photodetector output signal in Figure 3.19. Therefore, the yet-to-be-optimized system likely did not deliver the maximum available PV power to the loads at noon. As the solar irradiance decreased in the afternoon, the loads were disconnected from the PV module accordingly.

Another key feature of the LMPV system is its ability to rapidly respond to changes in the operating conditions of the PV array, like sudden changes in irradiance due to cloud coverage. This behavior can be seen in Figure 3.18 and Figure 3.19 when around 3:30 p.m. (15:30) there was a brief period with cloud coverage. First, the irradiance, as well as the power, increased slightly due to the effect of irradiance enhancement as the cloud

approached. Then, as the cloud passed over the module, the irradiance and power decreased. In response to this change in operating conditions, the photodetector tracked the change in irradiance, and PLC managed the connections of the loads accordingly.

The voltages that were applied to the loads throughout the day, shown in Figure 3.20, were also in line with expectations, according to the simulation results of the LMPV system with 4 loads of equal resistance in Figure 3.5. Being that the SP for the first load was set to 1.25 V and not 0 V, the voltage plot in Figure 3.20 resembles the simulated LMPV system case that included voltage regulation. The maximum power point voltage around noon was 19.32 V, whereas the lowest and highest voltages applied to the loads were 13.13 V and 24.68 V, respectively. Therefore, the range of voltages applied to the loads varied from -32% to +27% of the maximum power point voltage at noon.

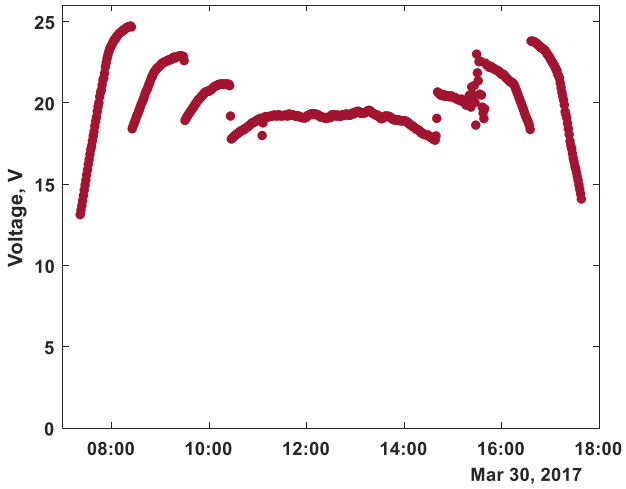

Figure 3.20. LMPV System Voltage Corresponding to Figure 3.18.

Efforts were made to optimize the proof-of-concept system by maximizing its energy yield of the available PV power through adjusting SP settings, number of loads, and

load resistance values. The experiment in Figure 3.18 was repeated in Figure 3.21, but with modified SP settings, shown in Table 3.4.

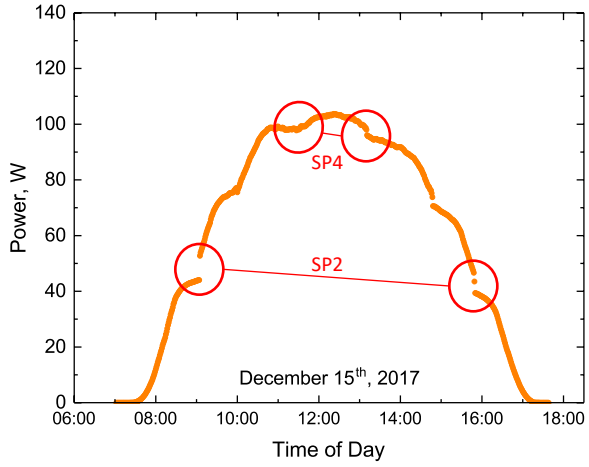

Figure 3.21. Power Delivered by the LMPV System to 4 Loads of Equal Resistance on 12/15/17.

Several important differences can be observed between Figure 3.18 and Figure 3.21. First, the maximum power in Figure 3.21 is much lower than that of Figure 3.18. However, the difference in maximum power was expected. Since the PV module had a fixed tilt angle, the maximum irradiance for the experiment in Figure 3.21 (conducted in December) was much less than the experiment in Figure 3.18 (conducted in March). This conclusion is supported by the photodetector signal measurements; for Figure 3.18, the maximum value of the photodetector signal was 9.73 V, compared to 8.32 V for the experiment in Figure 3.21.

Comparing the two 4-load experiments also revealed the effect of modifying the SP settings. First, setting SP1 to 0 V meant that power was consumed by the first load as soon as the PV module started producing power. Also, the sub-optimal setting for SP4 in

Figure 3.18 was corrected, resulting in a continuous power curve around that switch point. However, the setting for SP2 in Figure 3.21 was now sub-optimal, as there was a significant jump in power when the second load was connected. This behavior indicates that SP2 was too high, meaning the second load was connected too late, which caused the power to jump up.

The effect of temperature on the performance of the experimental LMPV is also much more pronounced in Figure 3.21. When the operating temperature of a PV array is increased, the output current increases slightly, but the output voltage decreases by a greater magnitude, resulting in an overall decrease in power output. This relationship is highlighted by comparing the power at SP2 and SP4 in the morning compared to the afternoon, as shown by the negative slope of the red lines in Figure 3.21 connecting the morning and afternoon occurrences of SP2 and SP4. The phenomenon suggests that improvements can be made to the LMPV control algorithm by including some form of temperature correction.

The voltages that were applied to the loads throughout the day, shown in Figure 3.22, were also in line with expectations. Being that the SP for the first load (SP1) was set to 0 V, the voltage plot in Figure 3.22 resembles the simulated LMPV system with 4 loads of equal resistance case, shown in Figure 3.5, that did not include voltage regulation. For Figure 3.22, the maximum power point voltage around noon was 19.69 V, whereas the lowest and highest voltages applied to the loads were 0 V and 25.63 V, respectively. The range of voltages applied to the loads varied up to +30.2% of the maximum power point voltage at noon.

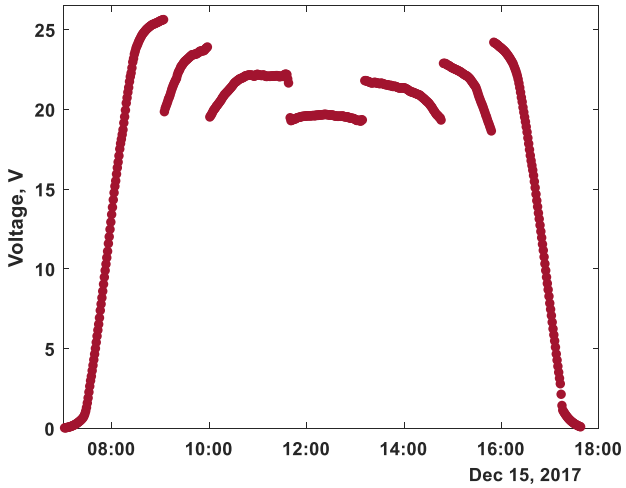

Figure 3.22. LMPV System Voltage Corresponding to Figure 3.21.

3.4.2 Experimental LMPV System with 6 Loads

The experiments from Figure 3.18 and Figure 3.21 were repeated after modifying the number of available loads from 4 to 6 and adjusting the resistance of each load to 21Ω. The power delivered by the LMPV system to the 6 loads is shown in Figure 3.23, which reveals that only SP5 provided an optimal threshold in which the power delivered to the loads appears to be continuous. The results in Figure 3.23 highlight the challenge of appropriately setting each of the SP values, due to the inherent differences between the simulation results and hardware implementation, that does not account for all the variables that affect the performance of the system.

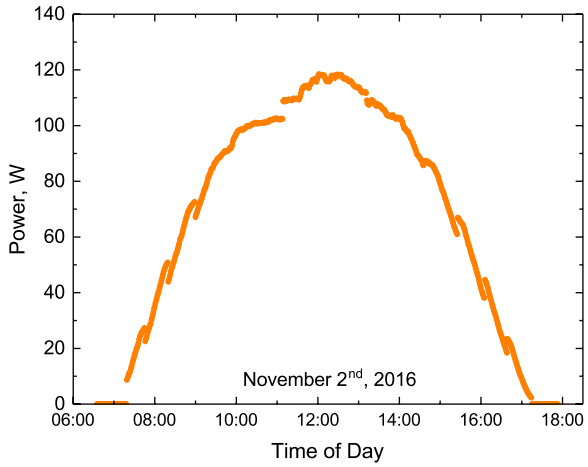

Figure 3.23. Power Delivered by the Experimental LMPV System to 6 Loads of Equal Resistance on 11/2/16.

However, Figure 3.23 also shows that power delivered to the loads around noon more closely resembles the shape of the photodetector signal on that same day (shown in Figure 3.24), which indicates that the combined resistance of the 6 loads more closely matched the characteristic resistance of the PV module at its peak output. One side effect of using the photodetector-based control is that the operating conditions at the photodetector's location are not always the same as the conditions experienced by the PV module. In Figure 3.24, the photodetector experienced some degree of shading, likely caused by a surrounding object, that injected some noise into the signal during the early morning. While this disturbance did not significantly affect the power output of the PV module, the first switch point was slightly delayed, causing the power of the PV module to jump up when the first load was eventually connected. This issue did not occur in the afternoon, as supported by the continuous power curve in the late afternoon in Figure 3.24.

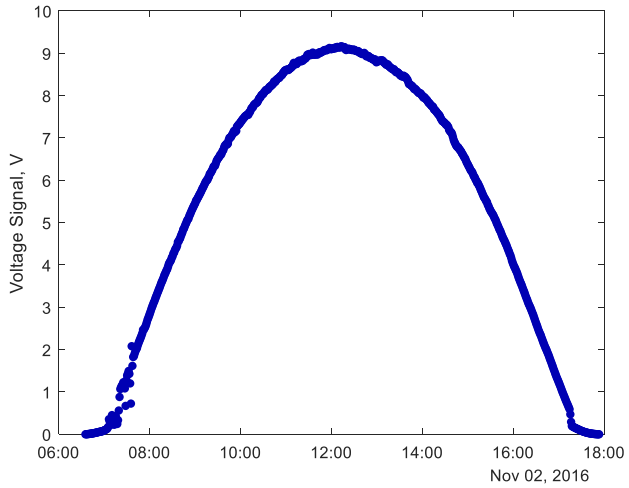

Figure 3.24. Photodetector Output Signal Corresponding to Figure 3.23.

Figure 3.25 shows the voltages applied to the loads by the LMPV system for the 6-load experiment conducted in Figure 3.23. Qualitatively, compared to the voltage plots in Figure 3.20 and Figure 3.22, the voltages in Figure 3.23 were closer to the voltage at noon for a longer period, which supports the conclusions drawn from the simulation results regarding tighter voltage regulations being easier to implement as the number of available loads increases.

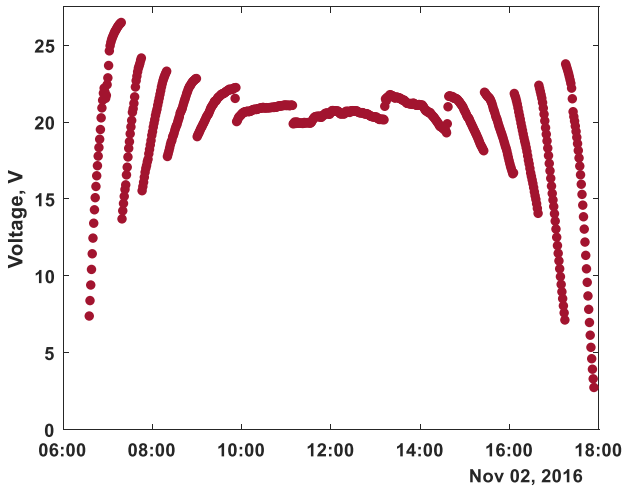

Figure 3.25. LMPV System Voltage Corresponding to Figure 3.23.

3.4.3 Experimental LMPV System with Unequal Resistance

An additional experiment was conducted to validate the simulation results of the LMPV system's performance when managing loads of unequal resistances. In this experiment, the first, second, and fourth loads were set to 17.75 Ω while the third load was set to 8.87 Ω, i.e., the third load takes twice the power as the other three loads under full irradiance. The results of this experiment are presented in Figure 3.26. While several of the switch points used for this experiment were also revealed to be sub-optimal, the overall shape of the power curve matches the simulation results from Figure 3.11, which supports the claim that the LMPV system can handle loads of unequal resistances.

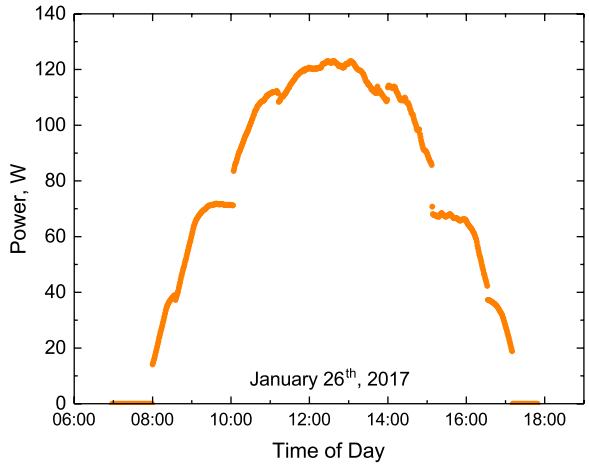

Figure 3.26. Power Delivered by Experimental LMPV System to 4 Loads of Unequal Resistance on 1/26/17.

3.4.4 Discussion of Experimental Results

Overall, the experimental results provided validation to the simulation results in the previous section. First, experiments on the prototype LMPV system were able to be conducted for 1-6 available loads and the resistances of the loads could be modified as

well. The PLC was able to communicate with the photodetector and adjust the number of loads connected to the PV array throughout the day based on the output voltage signal from the photodetector circuit and the programmed V_{SP} threshold values. The experimental results also validated the ability of the LMPV system to accurately respond to rapid changes in irradiance, as revealed by the results presented in Figure 3.18 and Figure 3.19, where the system briefly experience cloud coverage.

Conversely, the experimental results revealed many of the challenges associated with the actual implementation of an LMPV system. One drawback of the experiments conducted on the prototype LMPV system was that there was no way to simultaneously measure the power delivered by the LMPV system as well as the maximum available PV power throughout a day, meaning that the energy yield cannot be experimentally determined. Therefore, experiments were only performed on the prototype system during sunny days so that output power curves could be easily compared to the simulation results, such that conclusions can be drawn. While the results do indicate that the prototype system can respond to rapid changes in irradiance, it would be difficult to draw those same conclusions from an overcast day with highly variable PV output power.

The experimental results also highlighted the effects of temperature on the performance of the LMPV system. Differences in operating conditions between photodetector and PV array, like operating temperature or soiling, can reduce the accuracy in estimating the available PV power. Since the prototype system did not include any temperature correction, some of the switch points that produced optimal power curves in the morning did not do so in the afternoon because as the ambient temperature increased,

the switch points were not modified to track that change. This phenomenon suggests that some form of temperature correction could improve the performance and energy yield of the LMPV system. Small variations in location and orientation of the photodetector can also affect the accuracy of the switch points. One potential improvement would be to add a mechanical support structure to the PV array to which the photodetector could be attached to reduce the discrepancies between their operating conditions. Moreover, multiple photodetectors could be implemented to improve the estimation of available power, especially for larger PV arrays with larger physical footprints.

Lastly, the experimental results revealed the challenge of matching the combined resistance of the loads to the characteristic resistance of the PV array. Typically, the characteristic resistance of the PV array calculated by using the values from their specification sheets would not exactly match the characteristic resistance of the installed PV array. Even if that value was known, it is subject to change over time as the daily maximum irradiance changes with the season, as the temperature changes, and as the modules degrade over time. Each of these variables presents a challenge for implementations of the LMPV system with a photodetector-based control because as the quality of the power matching decreases, so does the energy yield.

4 LMPV SYSTEM WITH FEEDBACK-BASED CONTROL

In (Azzolini & Tao, 2018), the benefits of implementing an LMPV system were explored and supported by both simulation and hardware results. However, several challenges were discovered through the analysis of the hardware results. Being that the maximum power point tracking algorithm within the LMPV system relied on an estimation of available power from the PV array (Azzolini & Tao, 2018), differences in operating conditions between the photodetector and the actual PV array made it challenging to accurately estimate the maximum available power. Moreover, the lack of temperature compensation further complicated the estimation of available power and the control did not contain any type of feedback to correct for errors. This chapter introduces an alternative control methodology to address these challenges and others discussed in Chapter 3.4.4.

Instead of using a photodetector to estimate the maximum available power from the PV array, the feedback-based LMPV controller continuously measures the power output of the PV array. Therefore, when a load is connected or disconnected from the PV array, the change in power is monitored to ensure that change increased output power, i.e., to track the maximum power. The feedback-based LMPV controller has two inputs to measure the output voltage and current of the PV array and the output of the controller sets the state of each relay, as shown in Figure 4.1. Overall, the system in Figure 4.1 still contains the same fundamental components of the LMPV system, introduced in Figure 3.2, and still performs the MPPT functionality through load-matching, as detailed in Figure 3.1, but the way in which the system controls the loads has been modified. By directly measuring the output power of the PV array, there is no need to estimate the available

power, and any erroneous switching can be identified and corrected for through a feedback loop.

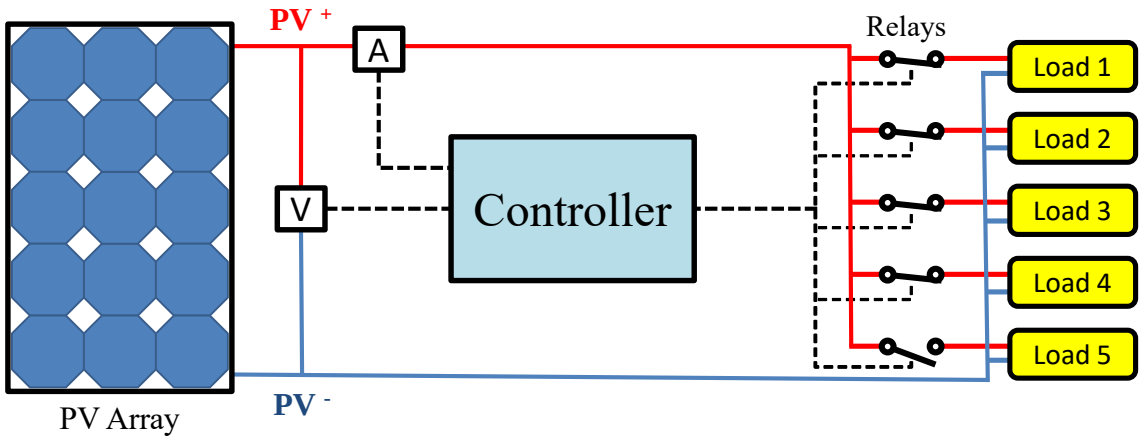

Figure 4.1. LMPV System with Feedback-based Control

4.1 Feedback-Based Load-Matching MPPT Algorithm

Being that the feedback-based LMPV system continuously monitors the output power of the PV array, the controller can determine if the power increased or decreased when the load was changed. Since the objective of the controller is to perform maximum power point tracking, when the power increases in response to a load being added or removed, the control action is considered successful and the power at that SP is recorded and stored. In this implementation of the LMPV system, the SP values represent values of power (in Watts), also referred to as P_{SP} values, as opposed to the V_{SP} values in Chapter 3. If the power decreases in response to a load being added or removed, the control action is considered to be unsuccessful and the controller reverts to its previous state. When an unsuccessful control action occurs, the threshold at which the system will try to add/remove that load again is updated based on the magnitude of the measured PV output power before

and after the control action occurred. A simplified overview of this load-matching MPPT algorithm is shown in Figure 4.2, which shows how the P_{SP} values are updated and stored each time a successful control action occurs. It is through this updating process that the system can handle changes in operating conditions over time, including the effects of temperature, soiling, degradations, etc.

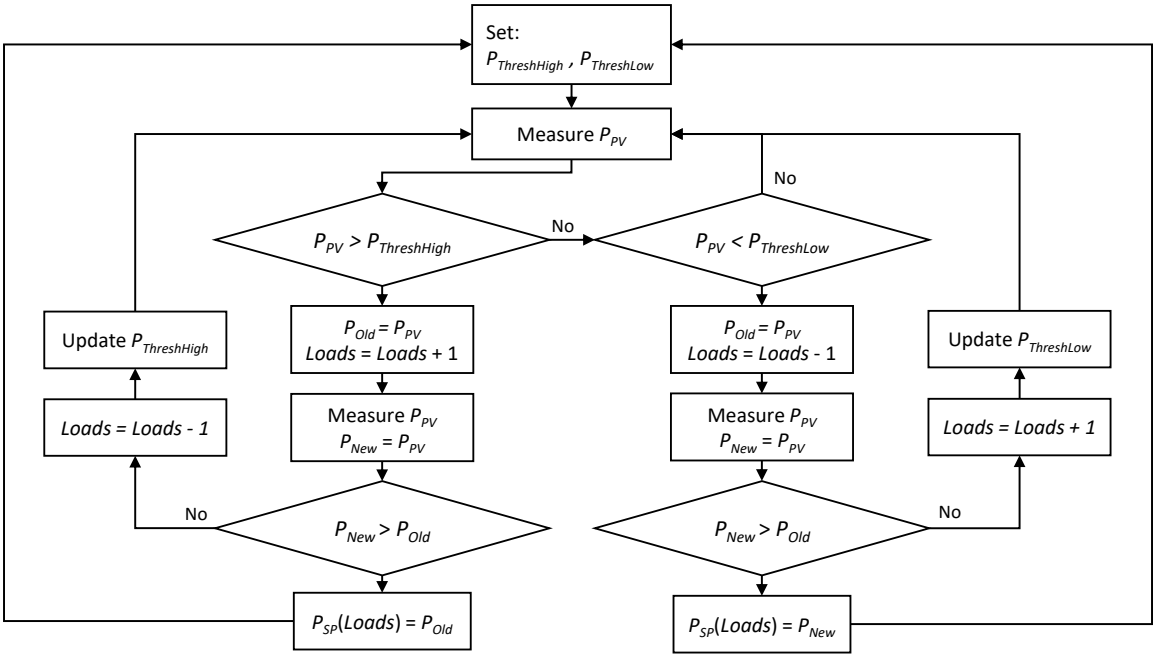

Figure 4.2. Simplified Block Diagram of the Feedback-based, Load-matching MPPT.

The feedback-based control algorithm for maximum power point tracking was developed in Simulink and implemented as a state machine using the Stateflow toolbox. The Simulink environment was selected for the development of the load-matching MPPT algorithm for its capability as a stand-alone simulation environment and for its ability to interact with data acquisition (DAQ) devices in real-time. In other words, once the algorithm was developed, it could be tested directly in Simulink using time-series models of PV systems and then deployed in hardware without having to translate code into another

language. For the hardware implementation, the desktop computer running the Simulink program acts as the processor and handles all the computation required by the control algorithm.

The Stateflow diagram for the MPPT algorithm of the feedback-based LMPV controlled is presented in Figure 4.3, which shows a more detailed depiction of the control algorithm from Figure 4.2. There are three main sections of the MPPT algorithm, outlined in Figure 4.3: 1.) monitoring power, 2.) adding a load, and 3.) removing a load.

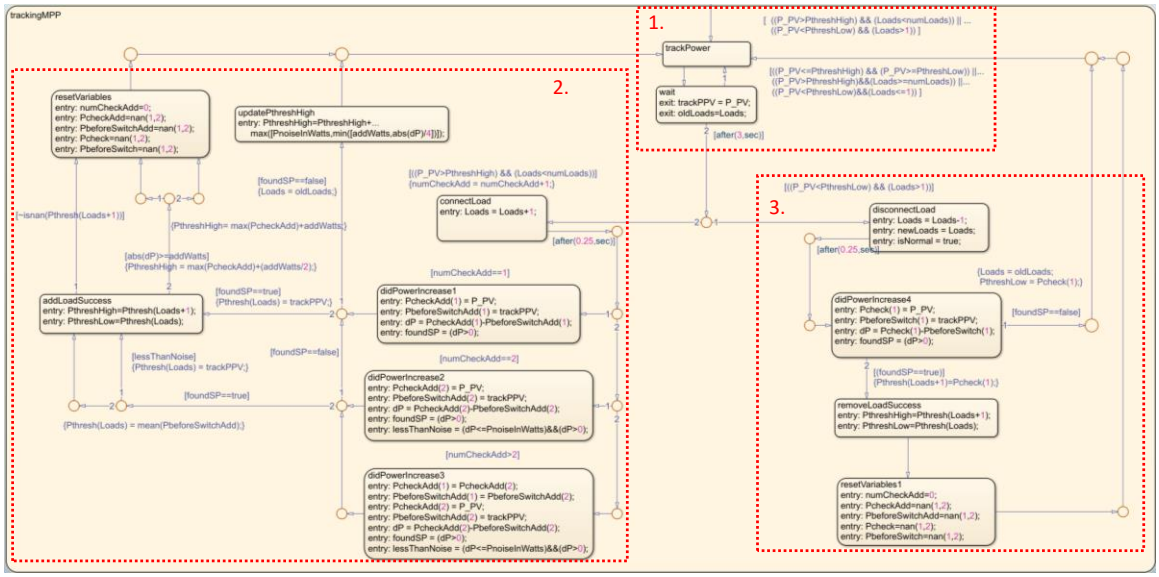

Figure 4.3. MPPT Algorithm for the Feedback-based LMPV Controller in Stateflow.

The *Pthresh* variable in Figure 4.3 is a critical component of the load-matching MPPT algorithm. This variable is an array that contains the P_{SP} values for each load, i.e., that values of PV output power (*P_PV*) above which each load should be connected to the PV array to perform maximum power point tracking. The *Pthresh* array is one-dimensional with a length equal to the number of loads available to the LMPV system. For example, the value of *Pthresh(2)* represents the P_{SP} value of the second load (in Watts), i.e., the

power threshold at which the second load is connected to the PV array in parallel to the first load. Likewise, *Pthresh(3)* represents the power threshold at which the third load is connected in parallel to the first two loads, and so on. The load-matching MPPT algorithm is implemented such that the P_{SP} values stored in the *Pthresh* array will update over time as the operating conditions of the PV array change over time. Theoretically, when all other variables are held constant, the P_{SP} values for each load in the system are not sensitive to changes in irradiance. However, the P_{SP} values are sensitive to changes in the operating temperature of the PV array and are potentially sensitive to degradation if the underlying characteristics of the PV modules are affected. The effects of soiling can also affect the P_{SP} values over time if different sections of the PV array (or different sections of a single module) experience different levels of soiling than the rest. Yet, regardless of the underlying cause for the changes in P_{SP} values, the controller can track the changes over time.

In section 1 of Figure 4.3, *P_PV* is measured at every time step (details regarding signal conditioning will be covered in a later chapter). When *P_PV* is either greater than the value of *PthreshHigh* or less than the value of *PthreshLow* (threshold values in Watts), the algorithm moves into the *Wait* block. The *Wait* block implements a time delay (equal to 3 seconds in Figure 4.3) to protect against any transients. If the value of *P_PV* moves back within the threshold values at any point during the time delay, the algorithm goes back to the *trackPower* block and the time delay is reset. Once *P_PV* maintains a value outside of the threshold values for the full 3 seconds, the algorithm moves to section 2 (assuming that *P_PV* > *PthreshHigh* and that there is another load available to be

connected to the PV array) or to section 3 (if *P_PV* < *PthreshLow* and there is a load available to be disconnected).

In section 2, the controller connects another load to the PV array, in parallel with any other connected loads, and then checks to see if the power increased or decreased. If the power decreased, the load is disconnected, the value of *PthreshHigh* is modified, and the algorithm returns to the *trackPower* block. The number of times the algorithm tries to connect a load is tracked by the *numCheckAdd* variable. The algorithm stores the two most recent values of *P_PV* before and after an additional load was connected and uses that information to update the *PthreshHigh* variable. If the power increased after the load was connected, then:

- The binary variable of *foundSP* is set to *true.*
- The value of *P_PV* before the switch took place is stored in the *Pthresh* array.
- New values are selected for *PthreshHigh* and *PthreshLow* based on the stored values in the *Pthresh* array.
    - If the value of *PthreshHigh* is set to *NaN*, an estimate of *PthreshHigh* is determined (simply by adding a predefined number of watts to the current value of *P_PV* using the *addWatts* variable). This situation only takes place while the algorithm is operating in Mode 1, i.e., when the algorithm is learning the *Pthresh* values on the first day the system is implemented. Once all the *Pthresh* values have been learned, the *addWatts* variable is no longer needed and the algorithm operates in Mode 2.

- The algorithm returns to the *trackPower* block.

The algorithm moves to section 3 after the value of *P_PV* is less than *PthreshLow* for the entire duration of the time delay, assuming there is a load available to be disconnected. Similar to section 2, the controller disconnects a load from the PV array and checks to see if the power increased or decreased. If the power decreased, the controller re-connects that load, updates the value of *PthreshLow* to the value of *P_PV* after the load was disconnected, and returns to the *trackPower* block. If the power increased after the load was disconnected, then:

- The value of *foundSP* is set to true.
- The value of *P_PV* after the load was disconnected is stored in the *Pthresh* array.
- The algorithm returns to the *trackPower* block.

To further elaborate on the novel load-matching MPPT algorithm, let us consider an example in which the controller is monitoring a PV array consisting of a single PV module and the system has 6 ohmic loads of equal resistance to manage. In this example, we will assume the first load has already been connected to the PV array and the algorithm is trying to determine when the second load can be connected in parallel to the first load. To simplify the behavior of the PV module, we will assume a constant temperature of 25° C and a clear-sky irradiance profile. In Figure 4.4, the top plot shows the output power of the PV module (*P_PV*) versus time and the bottom plot shows the number of loads connected to the PV module versus time.

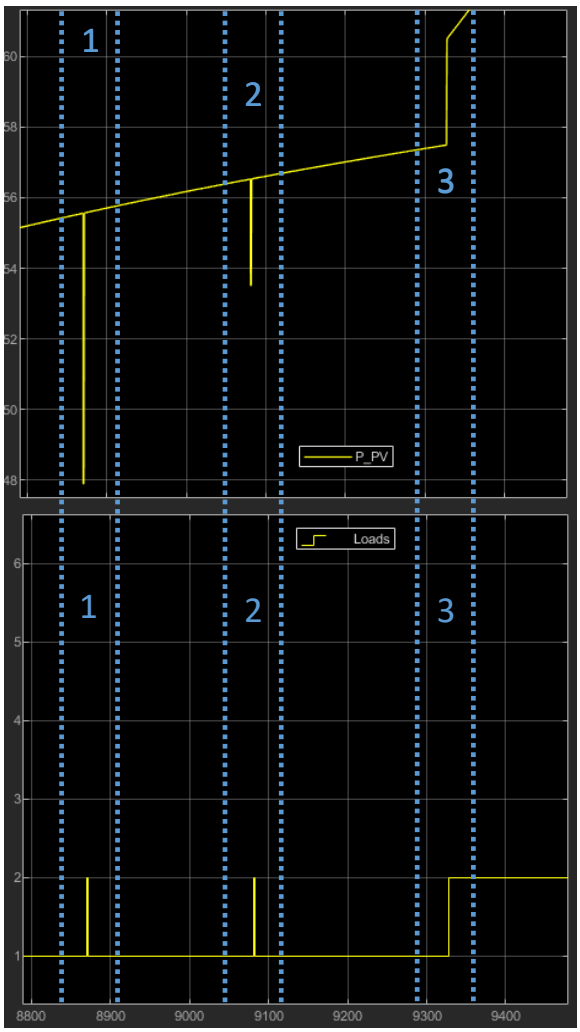

Figure 4.4. Example of MPPT Operation for Feedback-based Control.

Figure 4.4 is broken down into three parts (numbered 1 through 3) to help explain the operation of the MPPT algorithm. In part 1, the value of *PthreshHigh* was equal to 55.5 W. After *P_PV* remained above *PthreshHigh* for 3 seconds, Load 2 was connected in parallel to Load 1, as observed in the bottom plot of Figure 4.4. However, the value of *P_PV* dropped to under 48 W, so Load 2 was disconnected promptly and *P_PV* returned to its value just before the switch occurred. The value of *PthreshHigh* was then modified to about 56.5 W, based on (5):

$$PthreshHigh = PthreshHigh + \min\left(\left[addWatts, \left(\frac{abs(dP)}{4}\right)\right]\right); \quad (5)$$

where *dP* represents the difference between *P_PV* before and after Load 2 was connected. This equation, which is used in the algorithm when *foundSP=false*, shows that the maximum value that *PthreshHigh* can be increased by is determined by the value of the *addWatts* variable. As the value of *dP* decreases, it is used to modify the value of *PthreshHigh* instead of *addWatts*. From (Azzolini & Tao, 2018) it is known that optimal P_{SP} values result in a continuous power curve. Therefore, this equation helps the controller to check more frequently as the optimal P_{SP} value is approached. In this example, *addWatts* was equal to 4, so *PthreshHigh* was modified from 55.5 W to 56.5 W based on the value of *dP*.

In part 2, the process of connecting the second load was repeated. Again, the value of *P_PV* decreased when Load 2 was connected. So, Load 2 was then disconnected and *PthreshHigh* was once again modified by (5) from 56.5 W to 57.5 W. Then, in section 3, Load 2 was once again connected in parallel to Load 1. At this point, the value of *P_PV* increased, indicating a successful control action. The value of *P_PV* that resulted in the successful control action would then be stored in *Pthresh(2)*, the value of *PthreshLow* would be set to *Pthresh(2)*, and the value of *PthreshHigh* would be set to *Pthresh(3)* (if it were operating in Mode 2) or *Pthresh(2)* + *addWatts* (if it had been operating in Mode 1). Then, the controller would return to the *trackPower* block in Figure 4.3. This process would then be repeated as *P_PV* increases with the increase in irradiance throughout the morning and the maximum power point of the PV array would be tracked by connecting more loads.

Overall, this example highlights the two different modes of operations of the load-matching MPPT algorithm. When the P_{SP} value for a load is unknown, the algorithm operates in Mode 1, where it first estimates the P_{SP} value, then updates its estimate after each unsuccessful control action, using (5). Once all the P_{SP} values have been determined and stored in the *Pthresh* array, the values of *PthreshHigh* and *PthreshLow* are set based on the corresponding values of each load in the *Pthresh* array, i.e., Mode 2. It is expected that the controller will only operate in Mode 1 on the first day that the controller is implemented. As the P_{SP} values change over time, Mode 2 will track those changes and update the new P_{SP} values in the *Pthresh* array. Therefore, Mode 2 is expected to encounter fewer unsuccessful control actions than Mode 1.

4.2 Simulation of the Feedback-Based LMPV System

To properly design and test the novel load-matching MPPT algorithm, a model of the system and controller was developed in Simulink. The Simulink software environment contains many tools for modeling and simulating renewable energy systems, including detailed PV system models based on the NREL SAM database (Blair, DiOrio *et al.*, 2018). A model of the feedback-based LMPV system based on the diagram provided in Figure 4.1 was developed in Simulink and is presented in Figure 4.5. The Simulink model contains a PV array block, one current sensor, one voltage sensor, 6 ohmic loads of equal resistance, and a *Stateflow* block that contains the load-matching MPPT algorithm.

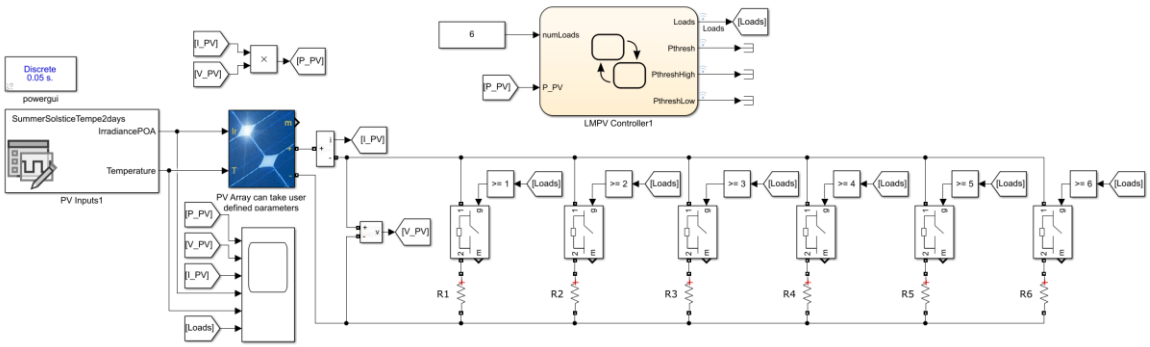

Figure 4.5. Simulink Model of the Feedback-based LMPV System with 6 Resistive Loads.

The PV array block in Figure 4.5 accepts user-defined PV array specifications, as was used for the simulations in this section. The PV array consisted of just a single PV module, modeled after a 290 W, 60-cell Yingli Solar module with: a V_{OC} of 38.99 V, a V_{MP} of 31.74 V, an I_{SC} of 9.69 A, and an I_{MP} of 9.13 A. The PV array block has two inputs: one for irradiance and one for temperature. Unless otherwise stated, the temperature was assumed to be a constant 25°C. Several irradiance profiles were generated using the PV_LIB toolbox developed by Sandia National Laboratories (Stein, 2012). In Figure 4.5, the PV_LIB toolbox was used to generate clear-sky irradiance profiles for Tempe, AZ for two consecutive days starting on the summer solstice. The decision to simulate two consecutive days was made to demonstrate the behavior of the feedback-based MPPT algorithm; the first day shows the behavior of the algorithm as it learns the P_{SP} values for each load, i.e., Mode 1, and the second day shows the behavior of the algorithm when the P_{SP} values have already been learned, i.e., Mode 2. The PV array block is linked to the NREL SAM database (Blair, DiOrio *et al.*, 2018) which loads in the PV module characteristics and sets the number of series-connected modules and number of parallel-

connected strings of modules that make up the full PV array. To simplify the behavior of the system, the PV array consists of just a single PV module.

Resistive loads are used in the Simulink model of the feedback-based LMPV system to simplify the behavior of the MPPT algorithm, but the system can handle other types of DC loads as well. The resistance of each load was set based on (2), such that the combined resistance of all 6 loads is equal to the characteristic resistance of the PV array at STC. Each load has its own relay that connects it to the PV array based on the output of the load-matching MPPT controller. The algorithm for the MPPT controller was designed and implemented using the Stateflow toolbox in Simulink, which contains the same code that was introduced in Figure 4.3. The load-matching MPPT controller only requires two inputs: the number of loads available to be managed and the output power of the PV array (the product of the current and voltage sensors).

4.2.1 Constant Temperature Results

The Simulink model of the feedback-based LMPV system with 6 loads of equal resistance was simulated for two consecutive days. The clear-sky irradiance profiles input to the PV array block were generated for Tempe, AZ starting on the summer solstice (06/21/2018), and a constant temperature of 25°C was used for the two-day simulation, as shown in Figure 4.6. The irradiance profile in Figure 4.6 represents the plane-of-array (POA) irradiance incident upon the tilted surface of the PV array. The tilt angle of the PV array was set equal to the latitude angle of the installation site (33°). The simulation was conducted as a discrete time-series using a time-step of 0.05 seconds.

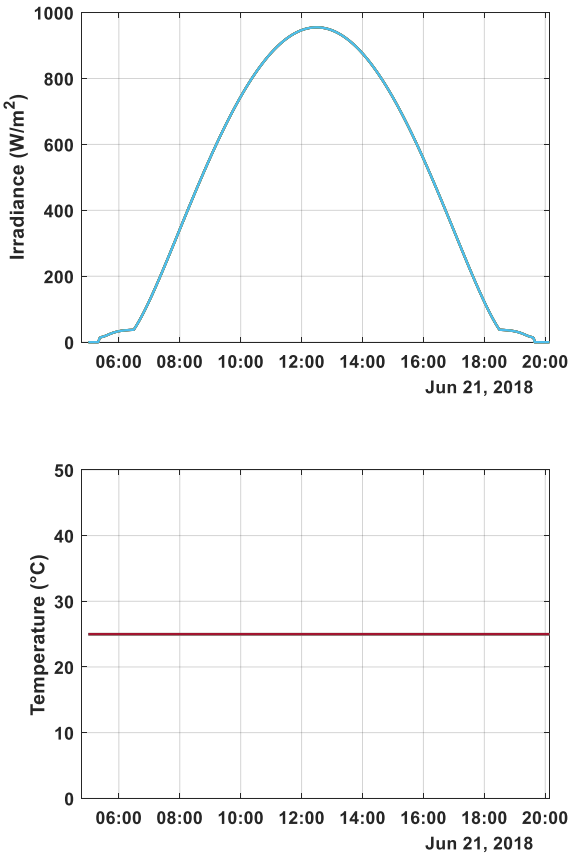

Figure 4.6. Irradiance and Temperature Profiles for Simulation of 06/21/18.

The results from the first day of the simulation (06/21/18) are presented in Figure 4.7, which shows the power, voltage, and current outputs of the simulated PV array, as well as the number of loads connected to the PV array. In Figure 4.7, the two different operating modes of the feedback-based controller are demonstrated. Throughout the morning, the controller was learning the optimal P_{SP} values for each of the loads, i.e., Mode 1. Since the optimal P_{SP} values were unknown at the beginning of the simulation, the system experienced a number of unsuccessful control actions for each of the loads, as observed in the bottom left subplot of Figure 4.7. In that subplot, the number of loads connected to the PV array oscillated between *n* and *n+1* loads as the controller tried to learn the optimal P_{SP} values for each load. After each of these unsuccessful control actions, the value of

PthreshHigh was increased, based on (5). Once a control action was successful, i.e., connecting an additional load to the PV array increased *P_PV*, the value for that P_{SP} was stored accordingly in the *Pthresh* array. By noon, all the P_{SP} values had been identified and stored in the *Pthresh* array.

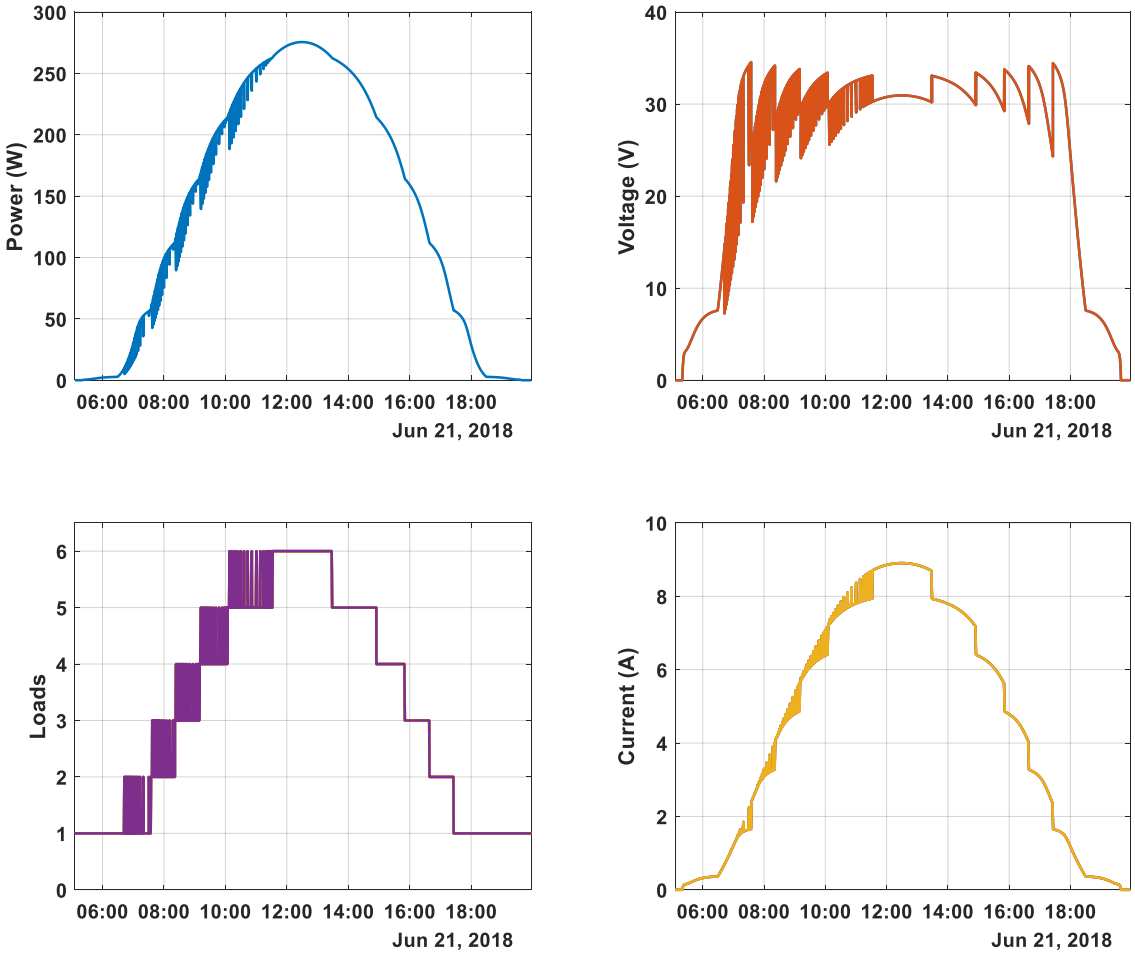

Figure 4.7. Simulation Results for Feedback-based LMPV System with Constant Temperature (06/21/18).

In the afternoon of 06/21/2018, the controller disconnected the loads (one load at a time) as the output power from the PV array decreased with the decreasing irradiance. At this point, the load-matching MPPT algorithm was operating in Mode 2. Since valid P_{SP}

values for each load had been successfully learned throughout the morning, the number of unsuccessful control actions were significantly reduced from tens of unsuccessful control actions per load in the morning to ≤ 2 per load in the afternoon. The controller then remained in Mode 2 until the end of the simulation after the two consecutive days had been simulated. The reason that the number of unsuccessful control actions for each load was still greater than 0 in the afternoon is that the P_{SP} values stored in the *Pthresh* array were not exactly the optimal values. So, each time those P_{SP} values are encountered, the controller still attempts to improve them. This function of the load-matching MPPT algorithm is highlighted in Figure 4.8, where the value of P_{SP} for Load 6 learned in the morning is compared to its afternoon value.

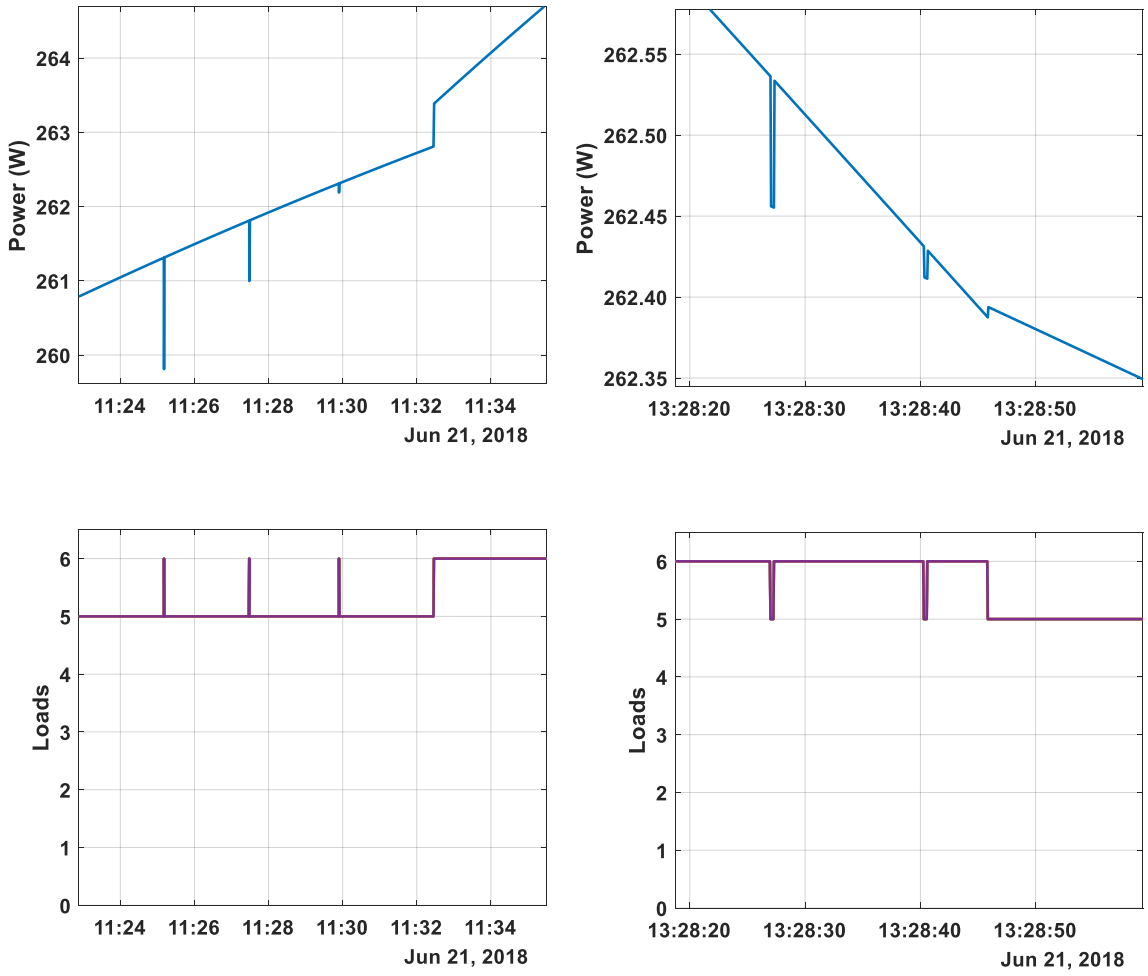

Figure 4.8. Results of P_{SP} for Load 6 in the Morning Compared to the Afternoon.

The top left subplot of Figure 4.8 shows the output power of the PV array as the controller experienced three unsuccessful control actions, followed by a successful control action. After the successful control action that connected Load 6 to the PV array, the output PV power increased from 262.8 W to 263.4 W. While the increase in PV power represented a successful control action, the jump in power indicated a suboptimal P_{SP} value; the optimal value would be less than 262.8 W and greater than the previous unsuccessful P_{SP} value of 262.3 W. Therefore, the average of those two values (262.55 W) was stored as an estimate of the optimal P_{SP} value for Load 6, i.e., *Pthresh(6)* was set to 262.55 W.

However, when this P_{SP} value was encountered again in the afternoon, the estimated optimal P_{SP} value was still not the exact optimal value, as observed in the two unsuccessful control actions in the top right subplot of Figure 4.8 (note that the first unsuccessful control action occurred just under 262.55 W due to the 3-second time delay). After each of these unsuccessful control actions, the value of *PthreshLow* was set equal to the PV output power at the time at which Load 6 was disconnected as an updated estimate of the optimal P_{SP} value; the value of PV output power while Load 6 was disconnected during the unsuccessful control action represented the upper bound of the optimal P_{SP} value. After the third control action was successful, the value of P_{SP} was set to 262.39 W and replaced the previous value of *Pthresh(6)*. While the change in the value of *Pthresh(6)* from the morning to the afternoon was relatively small due to the idealized assumptions of constant temperature, this process for updating the P_{SP} values stored in the *Pthresh* array is expected to play an important role in actual implementations of the feedback-based LMPV system where the operating conditions of the PV array are continuously changing.

Since two consecutive days were modeled for the simulation, the operating conditions of the PV array during the second day of the simulation were very similar to the first day, as shown in Figure 4.9. The POA irradiance reached the same peak of 955.2 W/m^2 and the temperature was held constant at 25°C.

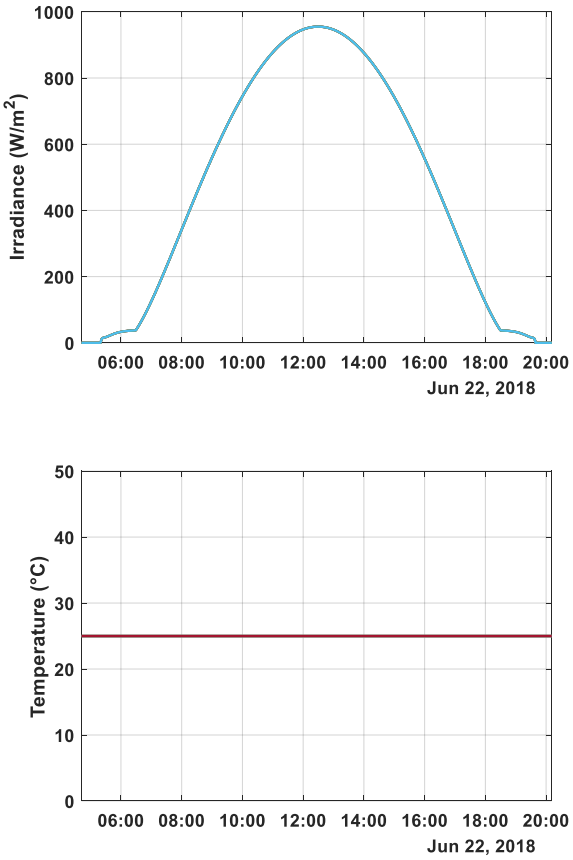

Figure 4.9. Irradiance and Temperature Profiles for Simulation of 06/22/18.

The results from the second day of the simulation (06/22/18) are presented in Figure 4.10, which shows the power, voltage, and current outputs of the simulated PV array, as well as the number of loads connected to the PV array. Unlike in Figure 4.7, the controller had already stored the P_{SP} values for each of the loads from the previous day in the *Pthresh* array and began the day operating in Mode 2. Throughout the morning, the controller connected loads to the PV array as the output power from the PV array increased with the POA irradiance and updated its estimates of the optimal P_{SP} values for each load as necessary. There were only two unsuccessful control actions during the simulation of the second day, as the P_{SP} value for Load 2 was updated just once in the morning and once in the afternoon—representing a significant improvement in unsuccessful control actions

from the first day. Overall, the results presented in this section indicate that the load-matching MPPT algorithm worked as expected under constant temperature conditions.

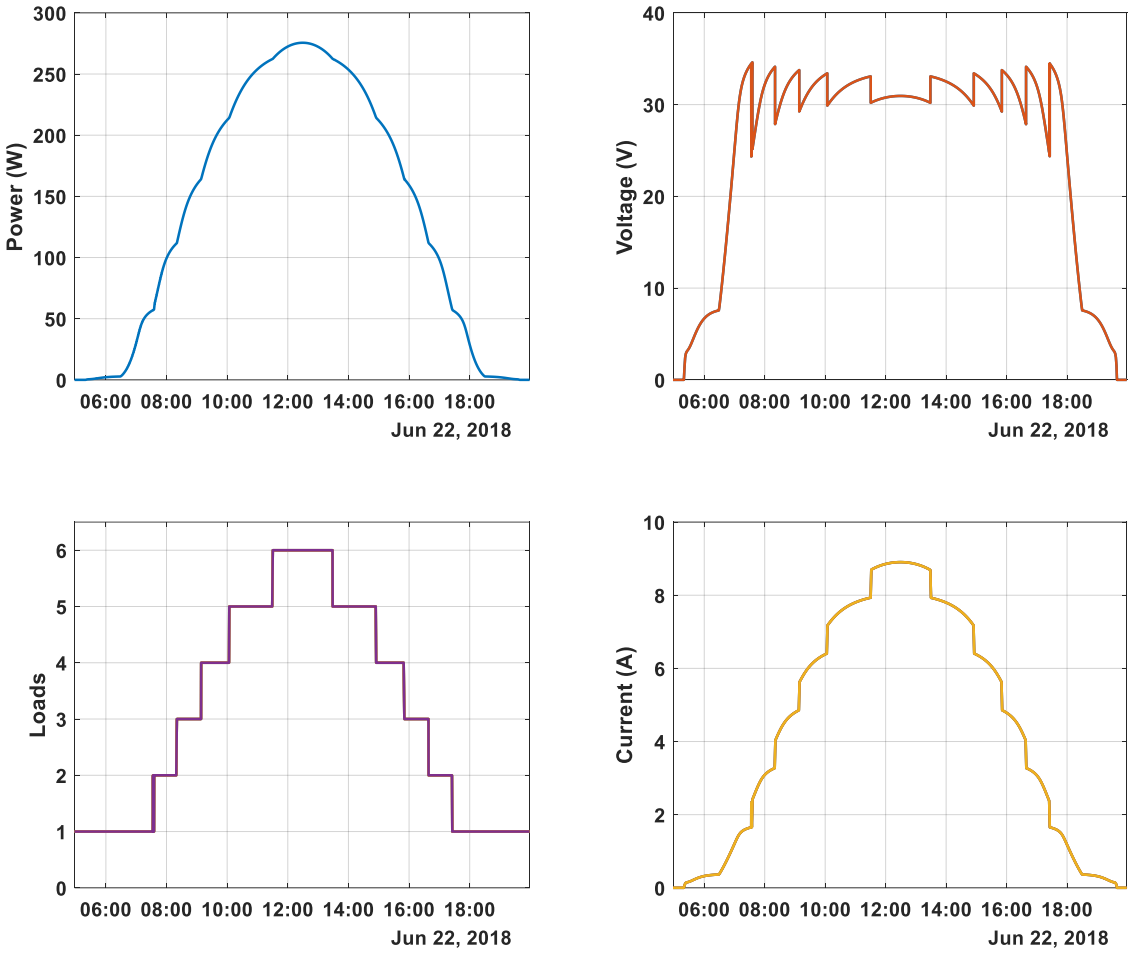

Figure 4.10. Simulation Results for Feedback-based LMPV System with Constant Temperature (06/22/18).

Table 4.1 compares the performance of the feedback-based LMPV system over the two simulated days. By comparing the midday P_{SP} values from 6/21 to the final P_{SP} values on 6/22, it can be observed that the initial values learned during the Mode 1 operation were relatively accurate. The P_{SP} value of 0 for Load 1 indicates that this load was always connected to the PV array. Since all the loads are purely resistive, the only requirement is

that they are sized accordingly to avoid exceeding any thermal limits. Assuming each resistor has a high enough thermal rating, they can consume power as soon as it is produced by the PV array.

Table 4.1. Comparison of Feedback-based LMPV System Performance over Two Days with Constant Temperature.

	06/21/2018 (Tempe, AZ)				06/22/2018 (Tempe, AZ)			
Loads	**Initial P_{SP} (W)**	**Midday P_{SP} (W)**	**Final P_{SP} (W)**	**Total Relay Actions**	**Initial P_{SP} (W)**	**Midday P_{SP} (W)**	**Final P_{SP} (W)**	**Total Relay Actions**
1	00.00	00.00	00.00	0	00.00	00.00	00.00	0
2	NaN	56.84	57.00	36	57.00	57.26	57.03	6
3	NaN	111.90	111.77	32	111.77	111.79	111.77	2
4	NaN	164.30	164.06	34	164.06	164.09	164.06	2
5	NaN	214.29	214.20	34	214.20	214.22	214.20	2
6	NaN	262.56	262.39	40	262.39	262.40	262.39	2
	PV Energy Extracted (Wh)				**PV Energy Extracted (Wh)**			
	2046.83				2046.94			

Table 4.1 shows the total number of relay actions that occurred for each of the loads, which represents both the successful and unsuccessful control actions. For example, an unsuccessful control action for connecting Load 3 results in the relay changing from its *off* state to its *on* state and then back to its off state, so 2 relay actions. The total number of relay actions from 6/22 was greatly reduced from that of 6/21 since the P_{SP} values had already been learned from the simulation of the first day. As noted in the discussion of Figure 4.10, only Load 2 resulted in unsuccessful control actions on the second day, whereas the relays associated with the rest of the loads only acted twice, i.e., turning from *off* to *on* once in the morning then turning from *on* to *off* once in the afternoon. It can also be observed that while these loads did not experience any unsuccessful control actions, their P_{SP} values were slightly modified throughout the day. So, even when a successful control action occurs, the algorithm still uses the updated measurements to improve its estimation of the optimal P_{SP} values for each load.

Lastly, Table 4.1 presents the total amount of energy extracted from the PV array for each day of the simulation. As expected, the energy extracted from the PV array during the first day of the simulation was slightly lower than that of the second day, which can be attributed to the reduction in power during each unsuccessful control action. While the duration of each unsuccessful control action only lasted for 0.25 seconds, it was long enough to cause a noticeable change in PV energy over the day. However, the amount of energy extracted from the PV array on the second day was only 0.0052% greater than on the first day; thus, the energy lost due to unsuccessful control actions can be considered negligible.

4.2.2 Varying Temperature Results

The simulation conducted in Chapter 4.2.1 was repeated after modifying the temperature profile of the simulated PV array to incorporate several step-changes. Since afternoon temperatures are typically higher than morning temperatures, the modified temperature profile included a 25% increase (from 25°C to 31.25°C) after the irradiance peaked around noon on each of the two consecutive days being simulated. The decision to model the varying temperature as a step-change, as opposed to a continuous change, was based on previous knowledge of the effects of temperature on the performance of the LMPV system as detailed in the discussion of Figure 3.21. Also, the use of a step-change in temperature simplifies the analysis of the temperature impact. At the end of the first day, the temperature was reset to 25°C. The irradiance and temperature profiles for the first day of the simulation are shown in Figure 4.11.

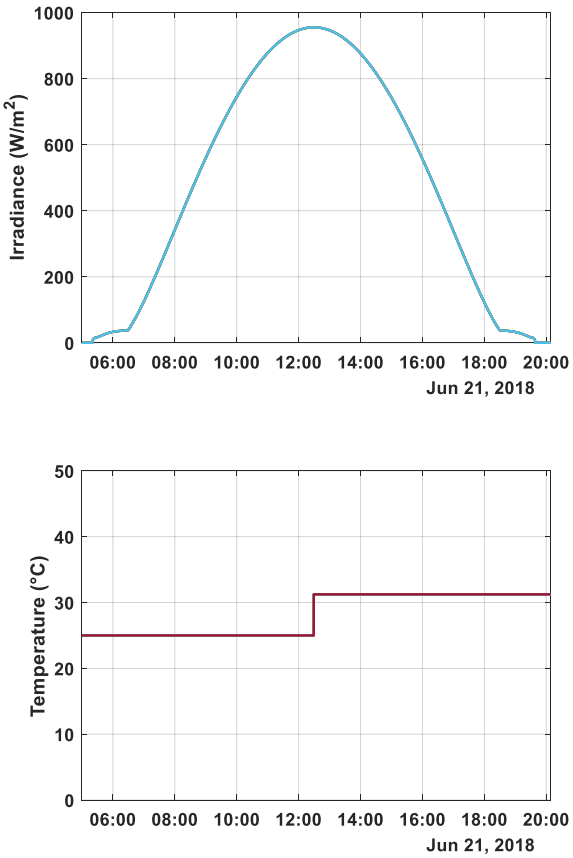

Figure 4.11. Irradiance and Temperature Profiles for Simulation of 06/21/18 with a Step-change in Temperature.

The results from the first day of the simulation (06/21/18) are presented in Figure 4.12, which shows the power, voltage, and current outputs of the simulated PV array, as well as the number of loads connected to the PV array. The effect of the step-change in temperature is observed in the PV array output power, voltage, and current subplots of Figure 4.12 around midday. The 25% increase in temperature also affected the optimal P_{SP} values as well; in the afternoon of the first day, there were more unsuccessful control actions taken compared to the results in Figure 4.7 where the temperature was constant throughout the entire day.

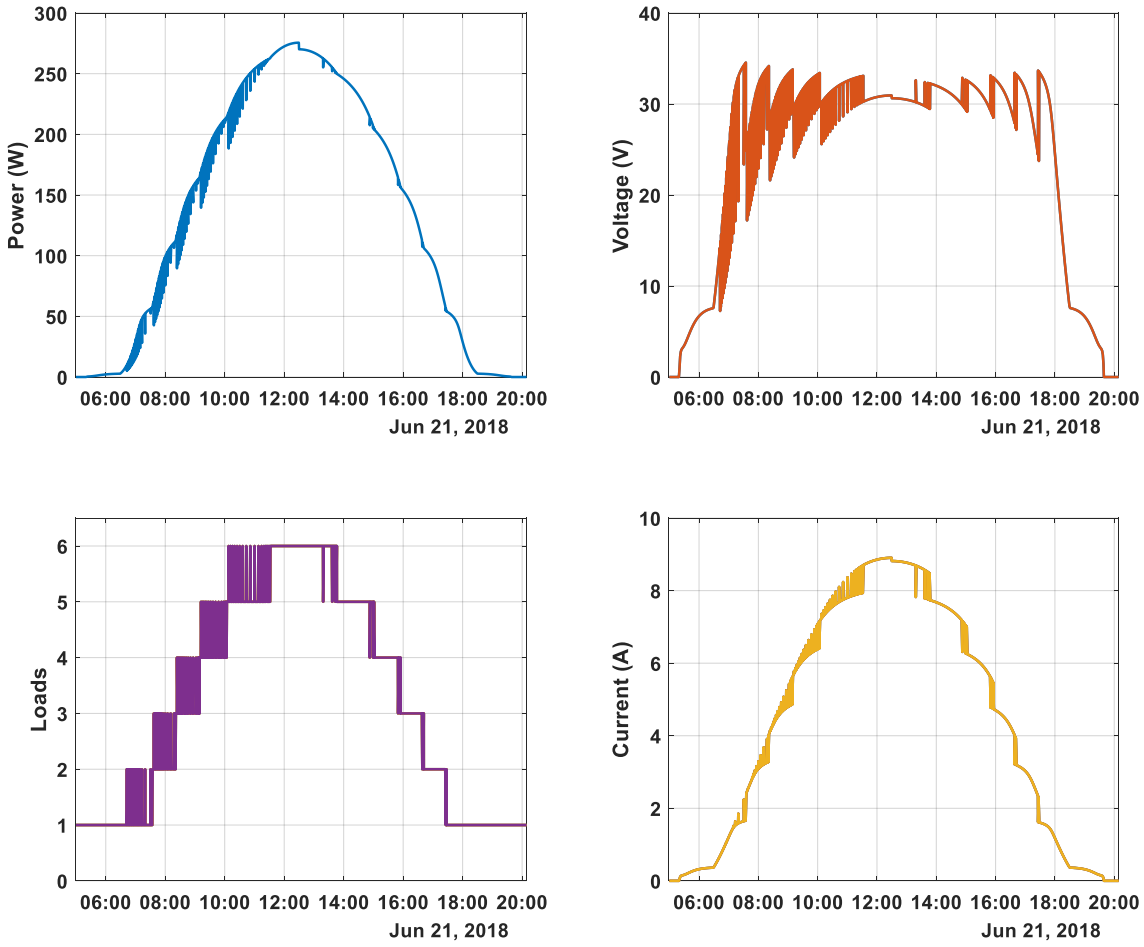

Figure 4.12. Simulation Results for Feedback-based LMPV System with a Step-change in Temperature (06/21/18).

For the second day of the simulation (06/22/2018), the temperature was reset back to 25°C for the morning and the step-change was once again applied after the POA irradiance peaked around midday, as shown in Figure 4.13.

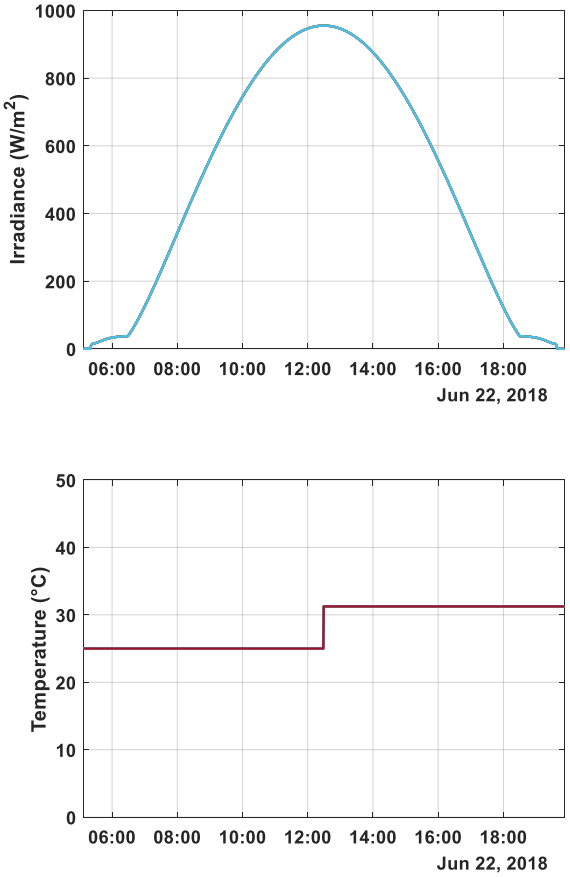

Figure 4.13. Irradiance and Temperature Profiles for Simulation of 06/22/18 with a Step-change in Temperature.

The results from the second day of the simulation (06/22/18) are presented in Figure 4.14, which shows the power, voltage, and current outputs of the simulated PV array, as well as the number of loads connected to the PV array. Being that the P_{SP} values for each of the loads had already been learned from the first day of the simulation and stored in the *Pthresh* array, the load-matching MPPT algorithm started the day operating in Mode 2. However, since the higher afternoon temperatures from the day before caused the optimal P_{SP} values for each load to be reduced, there were more unsuccessful control actions taken in the morning of the second day of the simulation (06/22/2018) compared to Figure 4.10 for which the temperature was held constant throughout the two-day simulation.

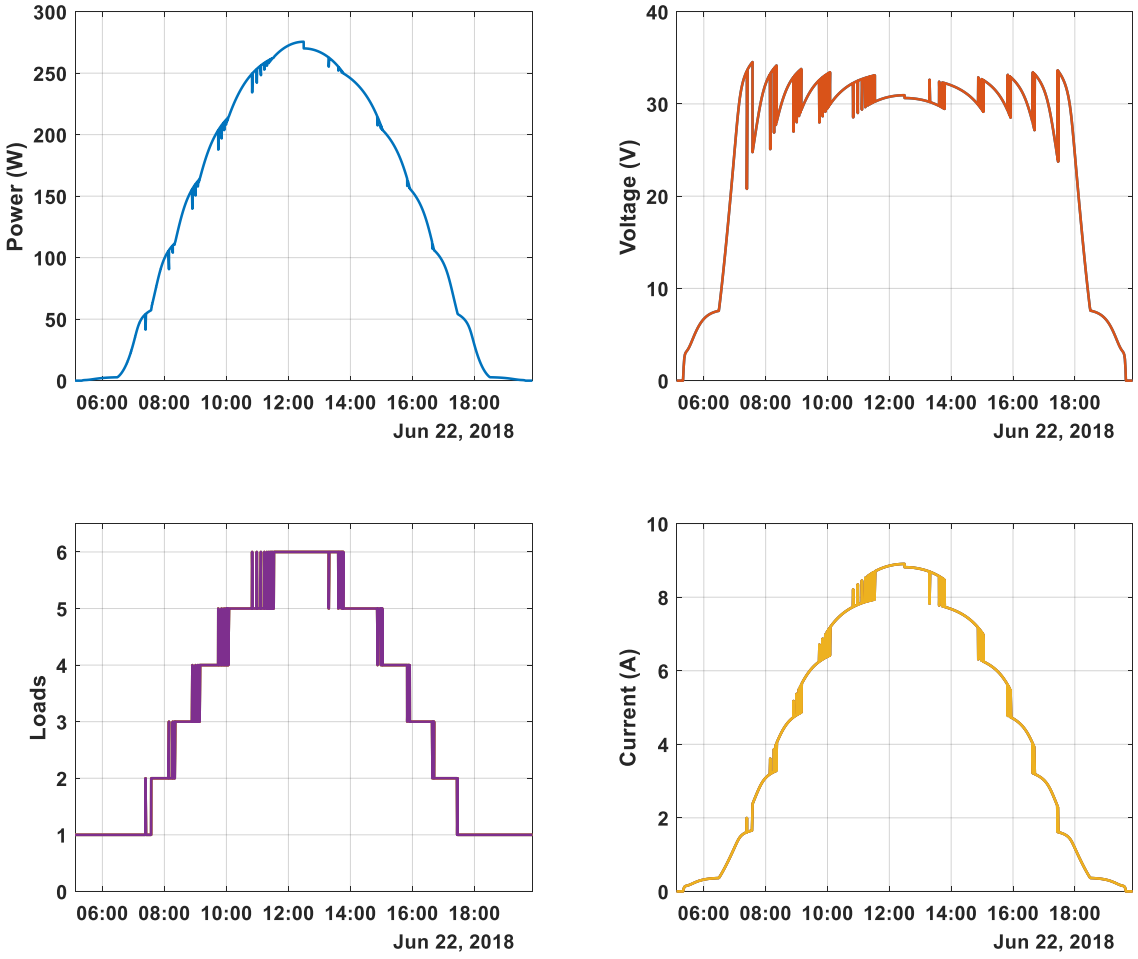

Figure 4.14. Simulation Results for Feedback-based LMPV System with a Step-change in Temperature (06/21/18).

The results from each day of the two-day simulation of the feedback-based LMPV system with several step-changes in operating temperatures are presented in Table 4.2. The effect of operating temperature on the performance of the feedback-based LMPV system was observed in several ways. First, the final P_{SP} values for 6/21 were noticeably lower than the midday P_{SP} values. This result indicates that the optimal P_{SP} values are correlated with changes in temperature, but not irradiance; these same two columns of data in Table 4.1 showed that the P_{SP} values were only slightly modified from their midday values to their final values.

Table 4.2. Comparison of Feedback-based LMPV System Performance over Two Days with Varying Temperatures.

	06/21/2018 (Tempe, AZ)				06/22/2018 (Tempe, AZ)			
Loads	**Initial P_{SP} (W)**	**Midday P_{SP} (W)**	**Final P_{SP} (W)**	**Total Relay Actions**	**Initial P_{SP} (W)**	**Midday P_{SP} (W)**	**Final P_{SP} (W)**	**Total Relay Actions**
1	00.00	00.00	00.00	0	00.00	00.00	00.00	0
2	NaN	56.84	54.11	40	54.11	55.71	54.11	8
3	NaN	111.90	106.12	36	106.12	111.78	106.12	14
4	NaN	164.30	155.87	40	155.87	164.09	155.87	20
5	NaN	214.29	203.66	42	203.66	214.28	203.66	26
6	NaN	262.56	249.63	50	249.63	262.72	249.63	34
	PV Energy Extracted (Wh)				**PV Energy Extracted (Wh)**			
	2024.19				2024.30			

The step-change in operating temperature also affected the total relay actions for each day of the simulation. Similar to the case in which temperature was held constant over the two-day simulation, the relays for each of the loads experienced a greater number of actions on the first day compared to the second. However, on both days, the total number of relay actions for each load was increased compared to the case with a constant temperature profile. Since the changes in temperature caused the optimal P_{SP} values for each load to move around, there were more unsuccessful control actions on each day, resulting in an overall increase in total relay actions. In general, the increase in relay actions should still be tolerable but is dependent upon the type of relay used. Mechanical relays can degrade over time and even fail to operate properly after a certain number of operations. In contrast, solid-state relays—like the ones used in power electronics—are designed to operate thousands of times per second. Therefore, solid-state relays would ideally be used for hardware implementations of an LMPV system, as they are more robust.

While the increase in operating temperature of the PV array did not have much of an effect from the first day of the simulation to the second (an absolute change of 0.11

Wh), the PV energy, in this case, was noticeably reduced from the case with a constant temperature profile. The PV energy extracted on the second day of the simulation with varying temperature was 1.12% less than the case with a constant temperature profile. However, this reduction in power is attributed to the effects of increasing temperatures on the output of the PV array, rather than the load-matching MPPT algorithm, as shown in Figure 4.15.

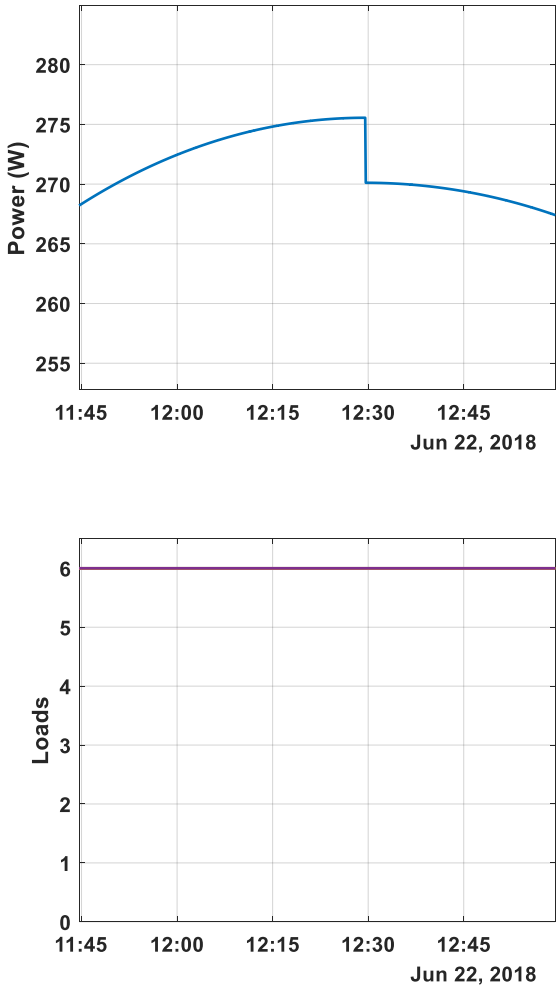

Figure 4.15. Effect of Increasing Temperature on PV Output Power.

When the step-change in temperature occurred, the number of loads connected to the PV array remained constant at 6, but the PV output power dropped from 275.6 W to 270.1 W (-2%), indicating that the reduction in power can be attributed to the PV array characteristics. This result was expected, as PV modules typically have a negative temperature coefficient associated with their output power.

4.2.3 Variable Irradiance Results

The simulation conducted in Chapter 4.2.1 was repeated after modifying the irradiance profile of the simulated PV array to incorporate actual irradiance measurements. The raw ground horizontal irradiance (GHI) dataset for Albuquerque, NM was downloaded from the PV Performance Modeling Collaborative of Sandia National Laboratories (Stein, 2012). Two consecutive days of measured GHI data were selected (06/23/2018-06/24/2018) based on their proximity to the dates used for the simulation in Chapter 4.2.1 and Chapter 4.2.2. The first day of GHI data (06/23/2018) represents a clear day, while the second day represents a partially cloudy day with relatively high variability; the selection of a clear-sky day and a partially cloudy day was made to showcase the performance of the feedback-based LMPV controller for days with low and high irradiance variability.

The GHI data was then converted to POA irradiance, assuming a PV array tilt angle of 35° (equal to the latitude angle of Albuquerque, NM) and an azimuth angle of 180°. To highlight the effects of using measured irradiance data on the performance of the feedback-based LMPV system, the operating temperature of the PV array was held constant at 25°C. The irradiance and temperature profiles for the first day of the simulation are shown in

Figure 4.16; the irradiance profile from Figure 4.6 is included as well to highlight the differences between the measured irradiance profile and the calculated clear-sky irradiance profile (Figure 4.6).

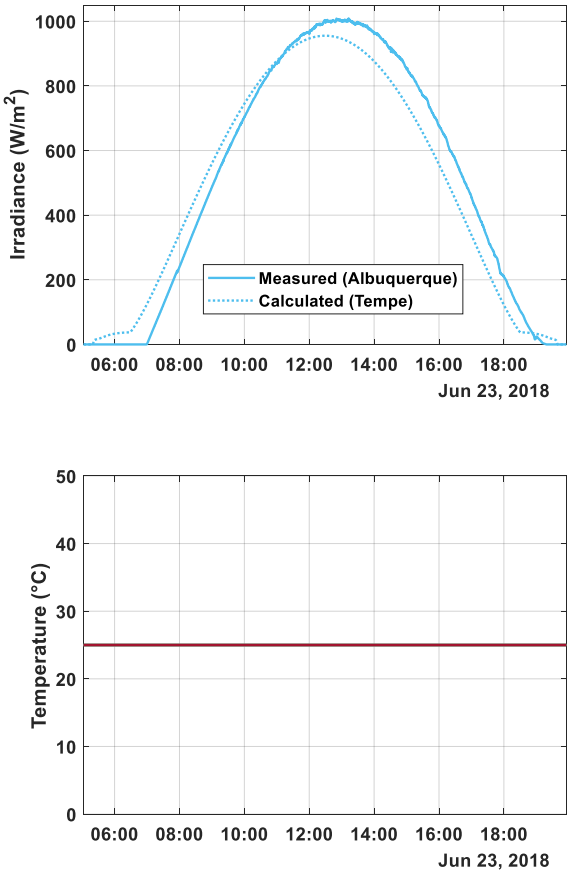

Figure 4.16. Irradiance and Temperature Profiles for Simulation of 06/23/18 with Measured Irradiance Data and Constant Temperature.

Figure 4.6 shows that the maximum POA irradiance of 1008.80 W/m^2 was slightly greater than the maximum POA irradiance of the simulations in Chapter 4.2.1 and Chapter 4.2.2 (955.2 W/m^2); the differences in the time and magnitude of the peak values of the two irradiance profiles are attributed to the differences between the PV locations, tilt

angles, and modeling assumptions. However, the overall shape of the two irradiance profiles was very similar.

The results from the first day of the simulation (06/21/18) are presented in Figure 4.17, which shows the power, voltage, and current outputs of the simulated PV array, as well as the number of loads connected to the PV array. The main difference between the results in Figure 4.17 and Figure 4.7 is that the maximum power experienced using the measured irradiance profile (292.12 W) was greater than that of (275.55 W), due to the increased maximum value of POA irradiance.

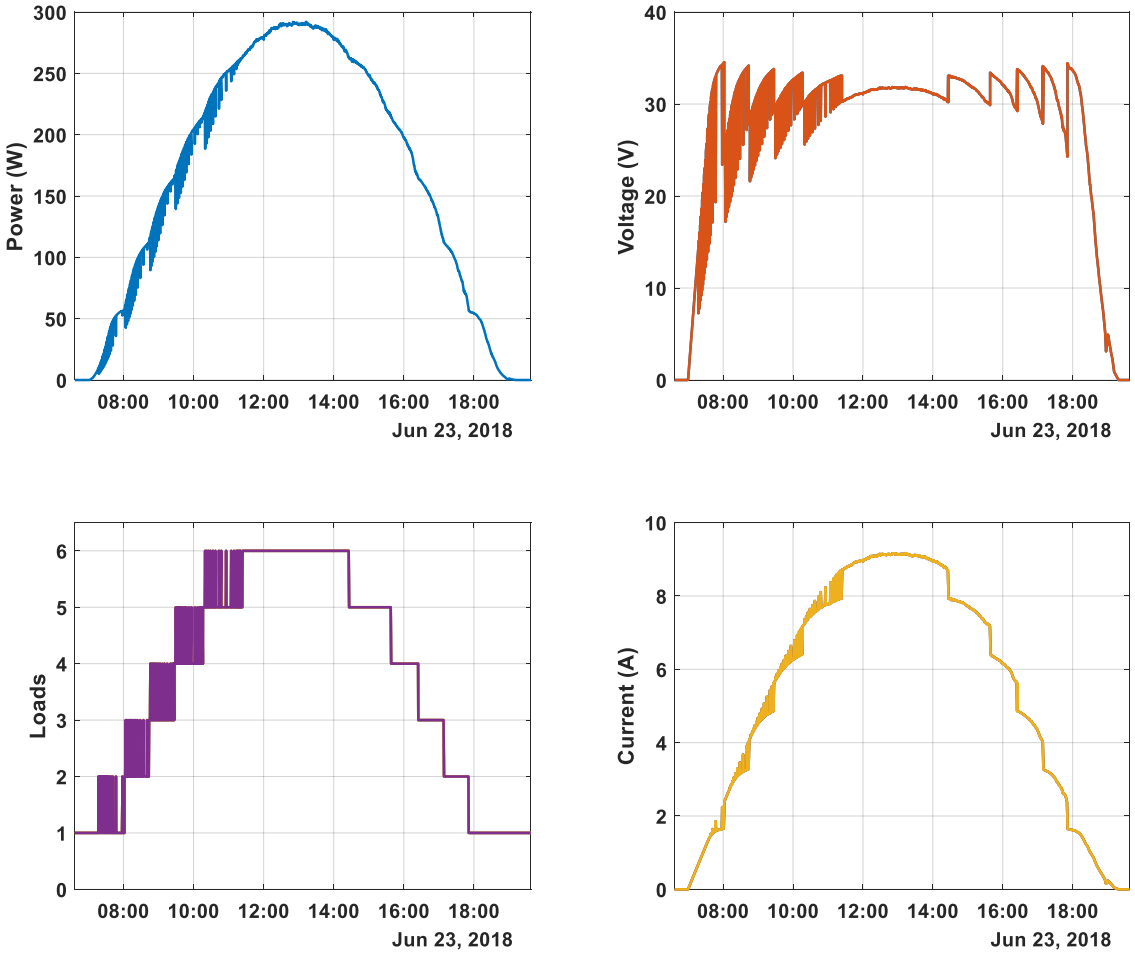

Figure 4.17. Simulation Results for Feedback-based LMPV System with a Measured Irradiance Profile and Constant Temperature (06/23/18).

Even though the measured irradiance profile contained a greater maximum value, the P_{SP} values for each of the loads were nearly identical, as shown in Table 4.3. This result further supports the claim that the optimal P_{SP} values are not affected by changes in irradiance.

Table 4.3. Comparison of Midday P_{SP} Values When Using Measured Irradiance Data.

	Clear-Sky Irradiance Model 06/21/2018 (Tempe, AZ)	**Measured Irradiance** 06/23/2018 (Albuquerque, NM)
Loads	**Midday P_{SP} (W)**	**Midday P_{SP} (W)**
1	00.00	00.00
2	56.84	56.85
3	111.90	111.90
4	164.30	164.31
5	214.29	214.29
6	262.56	262.54

For the second day of the simulation (06/23/2018), the temperature remained constant at 25°C, but the irradiance profile represented a partially cloudy day with relatively high variability, as shown in Figure 4.18. While most of the day was cloudy, the middle of the day was relatively clear, as the POA irradiance around noon reached a maximum value of 1001.66 W/m^2 (compared to 1008.80 W/m^2 from the previous day).

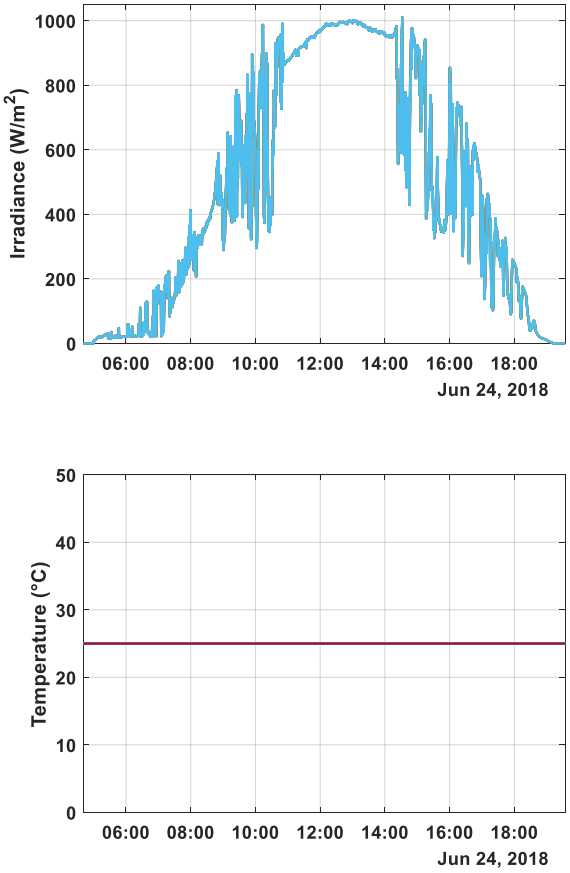

Figure 4.18. Irradiance and Temperature Profiles for Simulation of 06/24/18 with Measured Irradiance Data and Constant Temperature.

The results from the second day of the simulation (06/24/18) are presented in Figure 4.19, which shows the power, voltage, and current outputs of the simulated PV array, as well as the number of loads connected to the PV array. Due to the high variability of the POA irradiance, the PV output power was also highly variable. However, the load-matching MPPT algorithm was still able to perform successfully as it connected and disconnected the loads in response to the rapid changes in PV output power. Another indication that the algorithm worked as expected is that the maximum number of loads were connected around midday when the sky conditions were clear and then removed all but the first load by the end of the day.

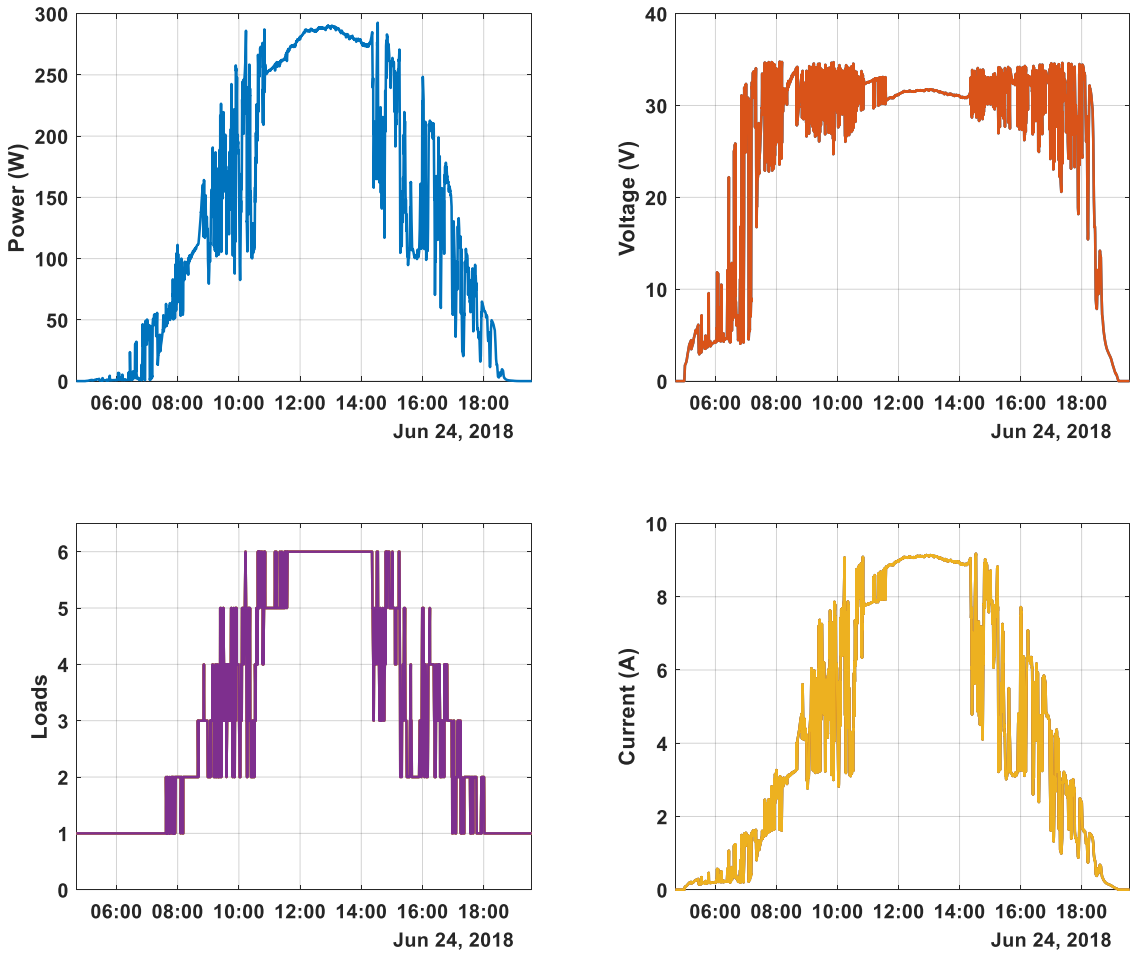

Figure 4.19. Simulation Results for Feedback-based LMPV System with a Measured Irradiance Profile and Constant Temperature (06/24/18).

Table 4.4 compares the performance of the feedback-based LMPV system for each day of the two-day simulation with the measured irradiance profiles. While the P_{SP} values were relatively stable on the first day of the simulation, they moved around a bit on the second day. Since it was previously shown that the optimal P_{SP} values do not change with changes in irradiance, the fact that the P_{SP} values varied on the second day indicates that the algorithm performs slightly better with lower irradiance variability. However, the P_{SP} values for each of the loads were still within a few watts from their values on the previous day, suggesting that the performance on the second day was still acceptable.

Table 4.4. Comparison of Feedback-based LMPV System Performance Over Two Days with a Measured Irradiance Profile and Constant Temperature.

	06/23/2018 (Albuquerque, NM)				06/24/2018 (Albuquerque, NM)			
Loads	**Initial P_{SP} (W)**	**Midday P_{SP} (W)**	**Final P_{SP} (W)**	**Total Relay Actions**	**Initial P_{SP} (W)**	**Midday P_{SP} (W)**	**Final P_{SP} (W)**	**Total Relay Actions**
1	00.00	00.00	00.00	0	00.00	00.00	00.00	0
2	NaN	56.85	56.97	36	56.97	57.96	57.00	72
3	NaN	111.90	111.78	32	111.78	113.19	109.30	142
4	NaN	164.31	164.07	36	164.07	164.23	163.98	194
5	NaN	214.29	214.16	32	214.16	214.03	211.95	174
6	NaN	262.54	262.39	38	262.39	262.59	259.88	90
	PV Energy Extracted (Wh)				**PV Energy Extracted (Wh)**			
	2140.52				2004.60			

Based on the results in Table 4.4, the highly variable irradiance profile used on the second day of the simulation (06/24/2018) had a greater effect on the total relays actions than it did on the P_{SP} values. The relays for each of the loads experienced a sharp increase in operations on the second day of the simulation, except for the relay associated with the first load which was always in the *on* position. As the output power from the PV array changed rapidly with the measured irradiance profile, the load-matching MPPT controller had to act more frequently to track the power changes, as expected. Overall, the increase in total relay actions is only a concern if mechanical relays are used, as their performance is likely to degrade more rapidly than solid-state relays.

The last major difference between the two-day simulation with measured irradiance profiles is the effect on the magnitude of energy extracted from the PV array. The energy extracted from the PV array on the second day was 6.35% less than that of the first day. Since it was previously shown that the decrease in power associated with unsuccessful control actions was negligible, the difference in PV energy from the first day to the second can be attributed to the reduction in POA irradiance on the second day.

4.2.4 Discussion of Simulation Results

Several key conclusions can be drawn from the simulation results of the feedback-based LMPV system. In all the experiments, the load-matching MPPT algorithm was able to successfully identify the P_{SP} values for each of the loads, indicating that the algorithm is fairly robust in its response to varying PV array operating conditions. By comparing the results from Table 4.1 and Table 4.4, it was determined that changes in POA irradiance do not affect the optimal P_{SP} values, but the load-matching MPPT algorithm can be affected by the rapidly changing PV output power associated with highly variable irradiance profiles. However, the algorithm was still able to determine P_{SP} values for each of the loads within a few watts of the optimal values.

It should be noted that the performance of the feedback-based LMPV system under highly variable irradiance conditions (Figure 4.19) represents a worst-case scenario. The PV array used in that simulation consisted of just a single PV module, whereas practical applications of the feedback-based LMPV system would contain several parallel-connected strings of PV modules, each of which containing several series-connected PV modules. It has been shown in the literature that larger PV systems with larger geographic footprints experience less variability in their output power than smaller PV systems (Lave & Kleissl, 2013). Therefore, it is expected that the ability of the algorithm to track the maximum power point of a PV array would improve as the size of the PV array is increased.

In Chapter 4.2.2, it was determined that the optimal P_{SP} values are inversely related to the operating temperature of the PV array. By inducing a step-change in the PV array operating temperature, both the output power and optimal P_{SP} values for each of the loads

were reduced, but the load-matching MPPT algorithm was still able to track the changes in P_{SP} values over time.

4.3 Hardware Implementation of an LMPV System with Feedback-Based Control

The feedback-based LMPV system described in Chapter 4.2 was constructed in hardware to validate the simulation results. The system contains each of the components shown in Figure 4.1, including one 48-cell silicon PV module, one voltage sensor, one current sensor, and six electromechanical relays (built into a PLC). The voltage and current sensors are connected to the analog inputs of a National Instruments USB-6001 DAQ, which communicates via USB with the desktop computer that runs the control algorithm in Simulink. This experimental setup is shown in Figure 4.20 (PV module is installed on the roof and is not pictured).

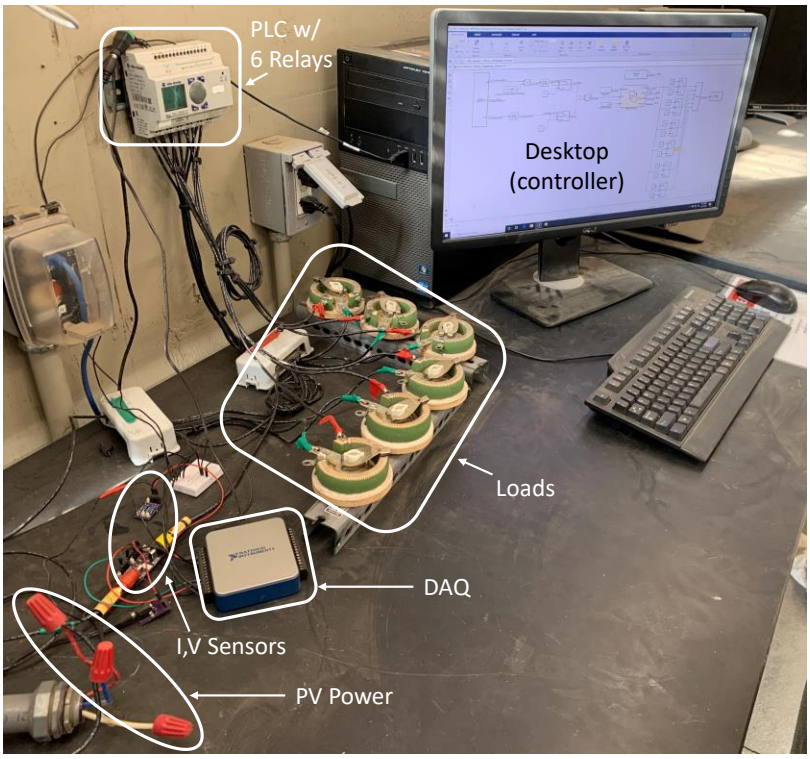

Figure 4.20. Hardware Implementation of Feedback-based LMPV System.

The following sections outline the design constraints and considerations for each of the components used in the hardware implementation of the feedback-based LMPV system. Being that the hardware implementation was intended to be used in a research setting, the individual components of the system were selected and designed with a certain degree of flexibility in mind. For example, the current and voltage sensors were designed to be compatible with higher power modern PV modules, rather than being optimized for use with the existing PV module installed on the roof. It is also important to consider that, since the system will be used in a research environment, the components selected for the hardware implementation described in this chapter may differ from those that would be used in a full-scale implementation of the feedback-based LMPV system. For example, this implementation of the system utilizes an off-the-shelf DAQ and desktop environment

to handle the signal processing and provide the computational power needed by the control algorithm; a full-scale implementation may utilize a microcontroller with onboard signal processing to provide a more compact solution. Other considerations will also be covered in the following subsections.

4.3.1 PV Array

The PV array used in the hardware implementation of the feedback-based LMPV system consisted of just a single Canadian Solar CS6A-170P PV module. The current-voltage and power-voltage characteristics of the PV module were measured *in situ* with a Seaward PV210 tester and the results are shown in Figure 4.21. The measurements were taken at the terminals of the installed PV module on April 9th, 2020 around solar noon. The PV210 reported an average POA irradiance of 1027 W/m^2 throughout the measurements, which is close to the 1000 W/m^2 STC irradiance value. The maximum power point of the module was determined to be 132.4 W with a maximum power point voltage of 17.4 V and a maximum power point current of 7.61 A. It should be noted that this module had been installed on the roof for several years before this measurement was taken, which explains the relatively poor characteristics; newer modules typically have more than double the output power capacity of this module. However, the load-matching MPPT algorithm does not require any knowledge about the PV array characteristics and is expected to operate successfully regardless of the PV array it is connected to.

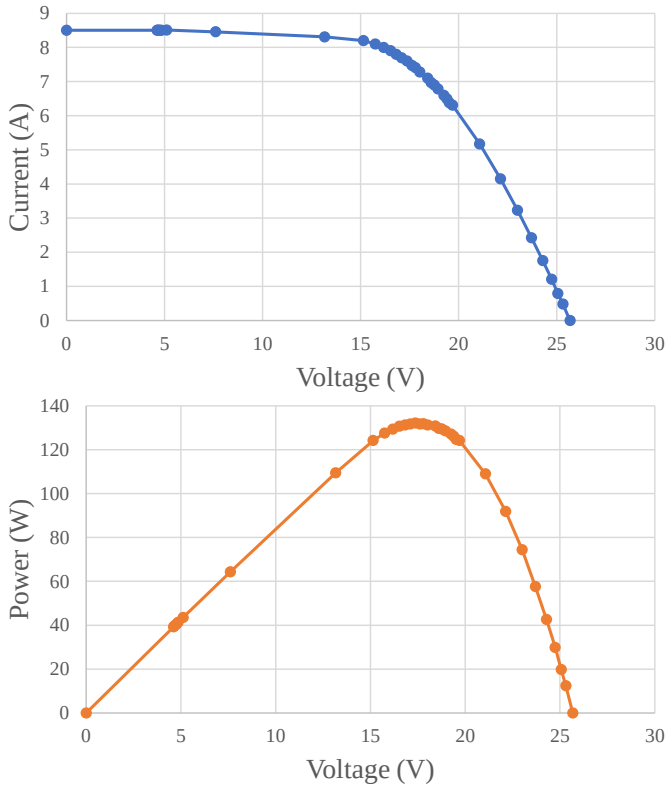

Figure 4.21. Current-voltage (Top) and Power-voltage (Bottom) Curves of the CS6A-170P PV Module.

4.3.2 Data Acquisition

A data acquisition device (National Instruments USB-6001) was selected to handle the analog measurements of the voltage and current sensors. The USB-6001 is capable of handling up to 4 differential analog inputs or up to 8 single-ended analog inputs with a maximum sample rate of 20 kS/second and has a built-in 14-bit analog-to-digital converter (ADC) resolution. The USB-6001 DAQ also has two analog output ports and many general-purpose digital input/output ports, providing a great deal of flexibility to accommodate future upgrades. Also, the USB-6001 is supported by MATLAB and

Simulink, allowing for the measurements to be triggered and synchronized to a real-time clock by the desktop computer.

The analog inputs ports of the USB-6001 have a range of +/-10 V. To minimize the quantization error of the built-in ADCs, each of the sensors was designed such that their output signals were in the range of 0-10 V. Since the negative input voltage range of the ADCs was not utilized, the ADC resolution was effectively reduced to 13-bits. However, this resolution still provides an acceptable level of accuracy for each of the measurements, as will be discussed later.

The analog output functionality of the USB-6001 DAQ was utilized to control the relays for each of the loads. Since the relays were built into the PLC, only one analog output port was needed. As the analog output voltage of the DAQ device increased, more loads were connected to the PV module through their corresponding relays. For example, an analog output voltage of 2 V would cause the PLC to activate the first two relays, a voltage of 3 V would activate the first three relays, and so on. With this configuration, the order in which the loads were connected throughout the day could not be modified while the controller was running. Future work could incorporate stand-alone relays to be directly controlled by the digital outputs of the DAQ to investigate more sophisticated algorithm features, such as load cycling to ensure all loads are powered equally throughout the day.

4.3.3 Current Sensor Design

One of the simplest and most reliable ways to measure current is by placing a precision resistor, or shunt resistor, in the current path and measuring the voltage drop

across it. Once the voltage and resistance values are known, the current can be calculated using Ohm's law. However, there is a trade-off to consider when selecting a shunt resistor. As resistance increases, the voltage drop across it increases as well, making it easier to accurately measure, but the power dissipated across the resistor is also increased. To minimize power losses, resistance values on the order of milli-ohms are typically selected, requiring additional components to amplify the voltage drop before it is measured, e.g., current-sense amplifiers. The analog output voltage of the amplifier is connected to the input of the ADC to digitize the measurement so that the controller can properly interpret it. The signal chain for a typical shunt current sensor is depicted in Figure 4.22.

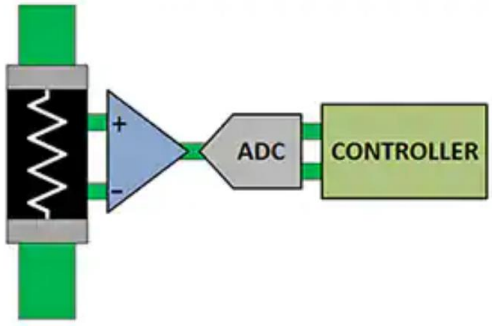

Figure 4.22. Signal Chain of a Typical Shunt Current Sensor (Leibson, 2018).

Instead of designing the current sensor based on the characteristics of the PV module in Chapter 4.3.1, which had a maximum power point current of less than 8 A, the sensor was designed to handle DC currents up to 10 A to accommodate the higher currents associated with newer PV modules. Being that the sensor was being placed upstream of the loads, the common-mode voltage range of the sensor needed to be able to handle the highest voltages expected from the PV module that occur near open-circuit conditions. Once again, to accommodate newer PV modules, a value of 40 V was selected.

To minimize power dissipation, a shunt resistor with a resistance of 20 mΩ and a current sense amplifier (LMP8640) with a gain of 50 V/V were selected that would produce an output voltage of 0-10 V (equal to the input range of the DAQ) over the expected current range of 0-10 A. The expected performance of the current sensor design is shown in Figure 4.23, where the output voltage scales linearly with changes in current.

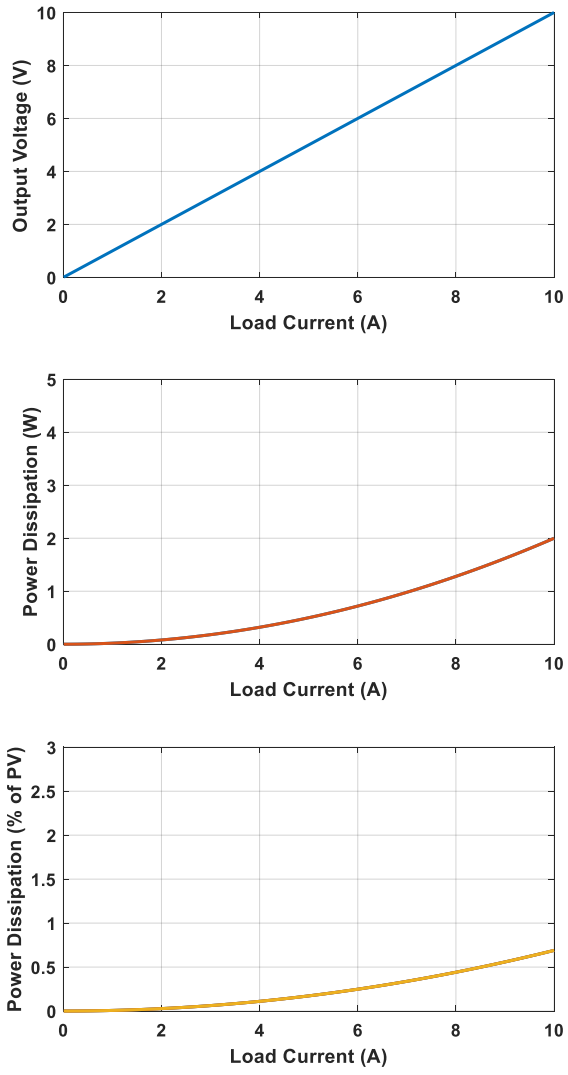

Figure 4.23. Analysis of Current Sensor Design.

Using a value of 20 mΩ resulted in a maximum power loss of just 2 W, which is less than 1% of the output power of a typical 300 W PV module. The output current is calculated by converting the output voltage of the current sense amplifier by using (6).

$$I_{PV} = \frac{V_{Out}}{Gain \times R_{Shunt}} \tag{6}$$

Since the value of the gain is a constant 50 V/V for the LMP8640 amplifier and the value of R_{Shunt} is also considered to be constant at 20 mΩ, the product of those two values will always equal 1. So, in this case, the magnitude of the analog output voltage of the current sense amplifier is equal to the magnitude of the current passing through the shunt resistor. This relationship is also depicted in the top subplot of Figure 4.23.

The analog output of the current sensor was connected to the analog input USB-6001 DAQ; the analog input port was configured for a differential measurement since the current sensor output did not share a common ground with the PV system. The positive range of the DAQ provides 13-bits of resolution, resulting in a maximum quantization error of roughly 0.6 mA, which introduced a nearly negligible amount of error into the signal chain.

Once the current sensor components were selected, a printed circuit board (PCB) was designed and fabricated. Overall, the PCB was designed to minimize any potential noise in the signal chain; the PCB was designed for differential measurement (to reject any ground noise) by adding two resistors to limit biasing currents, capacitors were added to stabilize the power supply voltage, and short leads were used to connect the voltage signal across the shunt resistor to the inputs of the current sense amplifier. To handle the full range

of output current from the PV module, the PCB was fabricated with 2oz copper traces, as opposed to the standard 1 oz copper traces used for many prototype PCBs. The electrical schematic and PCB layout of the current sensor are shown in Figure 4.24. A 3-D rendering of the current sensor PCB is shown in Figure 4.25.

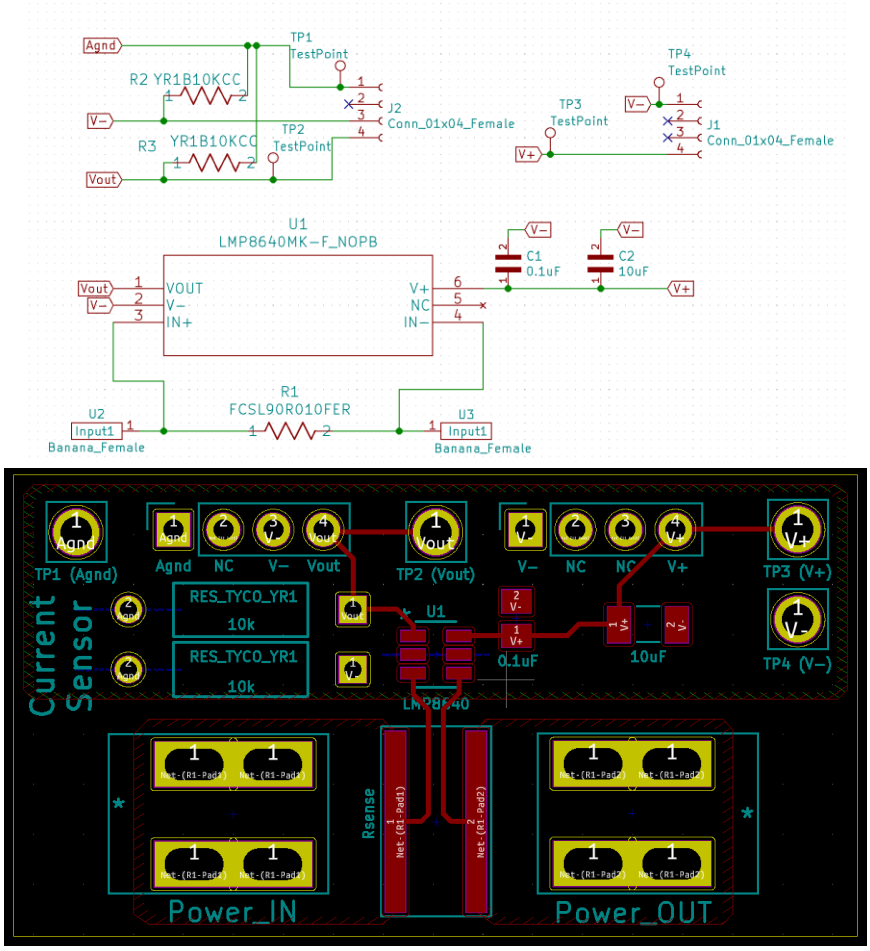

Figure 4.24. Current Sensor Electrical Schematic (Top) and PCB Layout (Bottom).

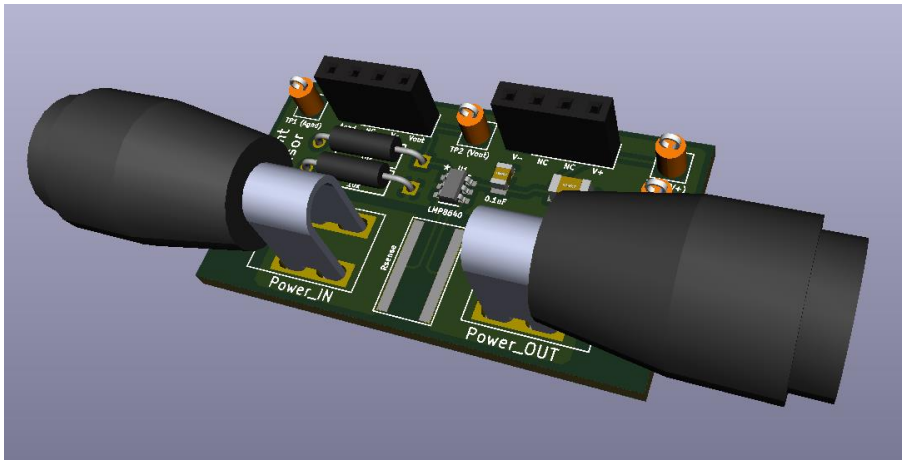

Figure 4.25. 3-D Rendering of Current Sensor PCB.

4.3.4 Voltage Sensor Design

To measure the output voltage of the PV module, a simple voltage divider was implemented. The resistance values of the voltage divider were selected based on a maximum output voltage of 40 V (the same value used for the voltage rating of the current sense amplifier) and the ratio between the two resistances provided an output voltage of 10 V (the maximum voltage that can be measured by the DAQ). The exact values of the two resistors were slightly modified to align with their commercial availability. The resulting resistance values selected were 47 kΩ and 15kΩ.

The expected performance of the voltage divider is shown in Figure 4.26, where the output voltage of the sensor scales linearly with the PV output voltage, reaching the 10 V maximum for PV voltages just over 40 V. Given the relatively large resistance values selected, the maximum power dissipated by the voltage divider was less than 0.03 W.

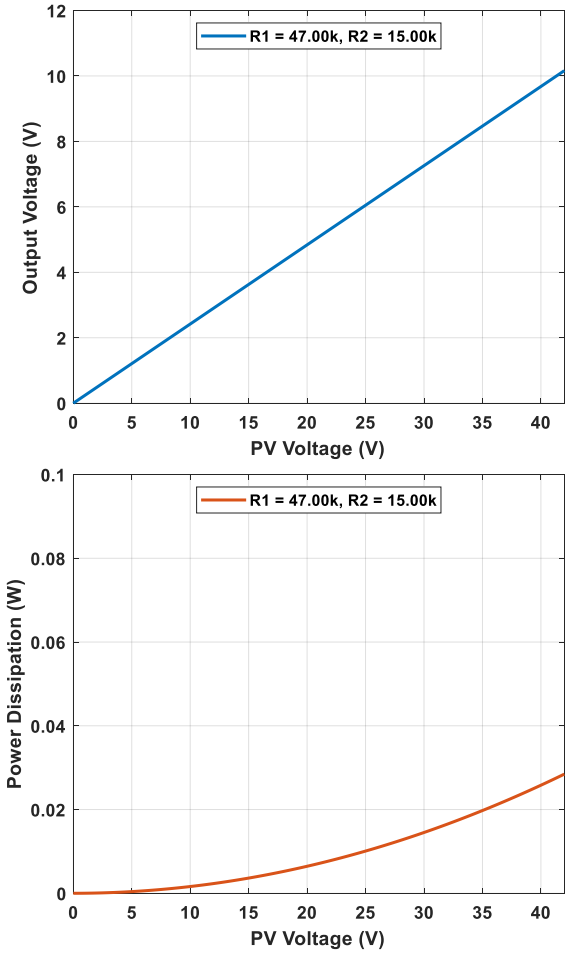

Figure 4.26. Expected Voltage Divider Performance.

The analog output of the voltage sensor was connected to the analog input USB-6001 DAQ; the analog input port was configured for a single-ended measurement since the voltage divider shares a common ground with the PV system. The positive range of the DAQ provides 13-bits of resolution, resulting in a maximum quantization error of roughly 2.5 mV, which introduced a nearly negligible amount of error into the signal chain. The analog measurements were multiplied by the voltage divider transfer function to convert the measurements back to their full-scale voltage values.

Once the voltage sensor components were selected, a printed circuit board (PCB) was designed and fabricated. Unlike the current sensor, the voltage sensor signal could not be configured as a differential measurement because it shared a ground with the PV module. However, the DAQ has several internal features to reduce noise as much as possible. The electrical schematic and PCB layout of the voltage sensor are shown in Figure 4.27. Given the relatively small footprint of the voltage sensor board, modifications were added to support the addition of biasing-resistors in case future designs support the use of differential measurements through an isolated ground. A 3-D rendering of the current sensor PCB is shown in Figure 4.28. This PCB was fabricated the PCB was fabricated with the standard 1 oz copper traces.

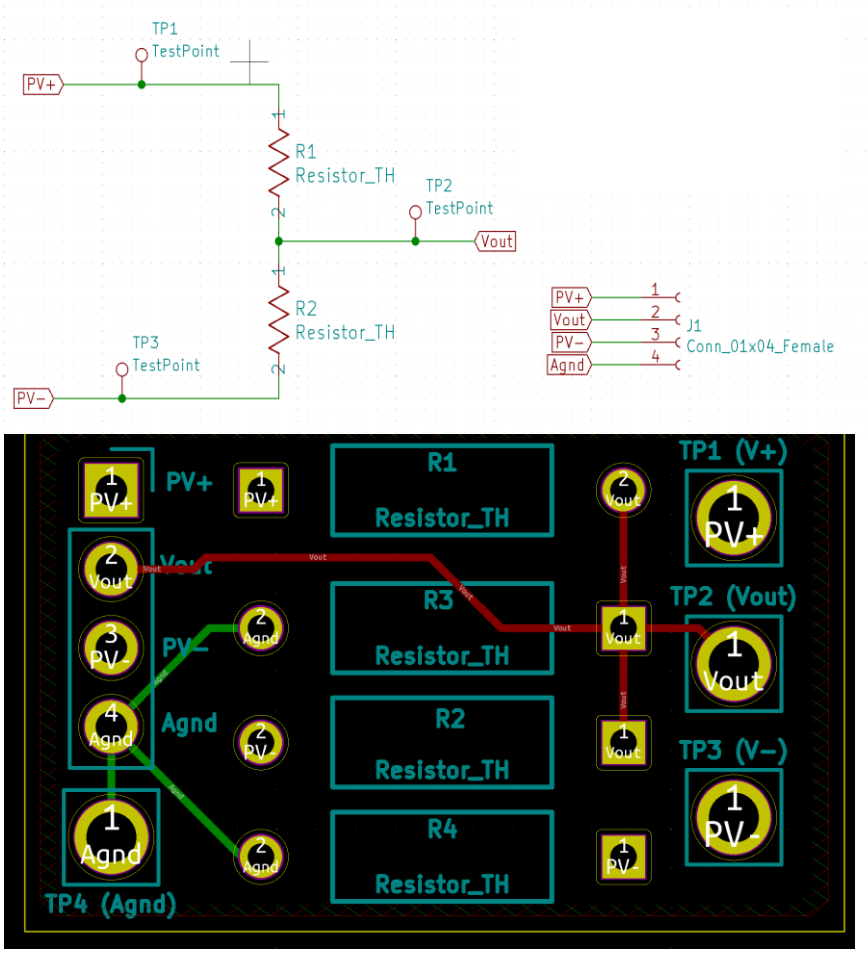

Figure 4.27. Voltage Sensor Electrical Schematic (Top) and PCB Layout (Bottom).

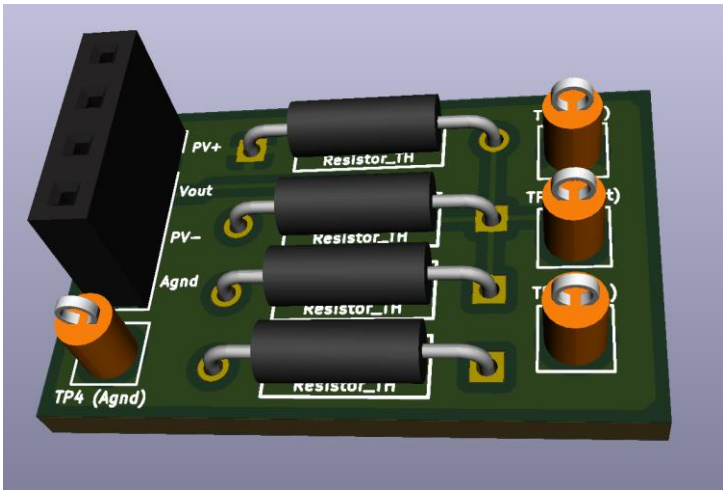

Figure 4.28. 3-D Rendering of Voltage Sensor PCB.

4.4 Hardware Validation Results

After the individual components of the system were procured, fabricated, and tested, the feedback-based LMPV system was installed on the roof of the Engineering Research Center building at Arizona State University. The load-matching MPPT algorithm from Chapter 4.1 was implemented in Simulink, where the PV array model and virtual sensors were removed and replaced by an analog input block that communicated with the USB-6001 DAQ. The Simulink model was synchronized with the real-time clock of the desktop computer and the model was set to query the DAQ device every 0.05 seconds. A moving average with a window length of 5 was used to smooth out the variations between the samples. The feedback-based LMPV system had 6 equal-resistance loads available to track the maximum power point of the PV array throughout the day. These settings were held constant for each of the results presented in the following subsections.

To highlight the various modes in which the load-matching MPPT algorithm operates, the hardware experiments were conducted over two consecutive days. On the first day, the algorithm attempts to learn the optimal P_{SP} values for each of the six loads. After each of the P_{SP} values are determined, the algorithm updates them over time as the operating conditions of the PV change. The algorithm can successfully learn the P_{SP} values of each of the loads regardless of when the experiment begins; experiments were initiated in both the morning and afternoon to demonstrate the performance of the load-matching MPPT algorithm in each case. While the performance of the load-matching MPPT algorithm is simpler to analyze during sunny days, experiments were also conducted on

days with cloudy weather to validate the performance of the system under highly-variable irradiance conditions. Each of these experiments is discussed in the following subsections.

4.4.1 Morning-Initiated Experiment

Similar to the simulation results presented in Chapter 4.2, an experiment was initiated on the hardware implementation of the feedback-based LMPV system on the morning of 05/01/2020 and was carried out until the evening of the following day. The results from the first day of the experiment are shown in Figure 4.29.

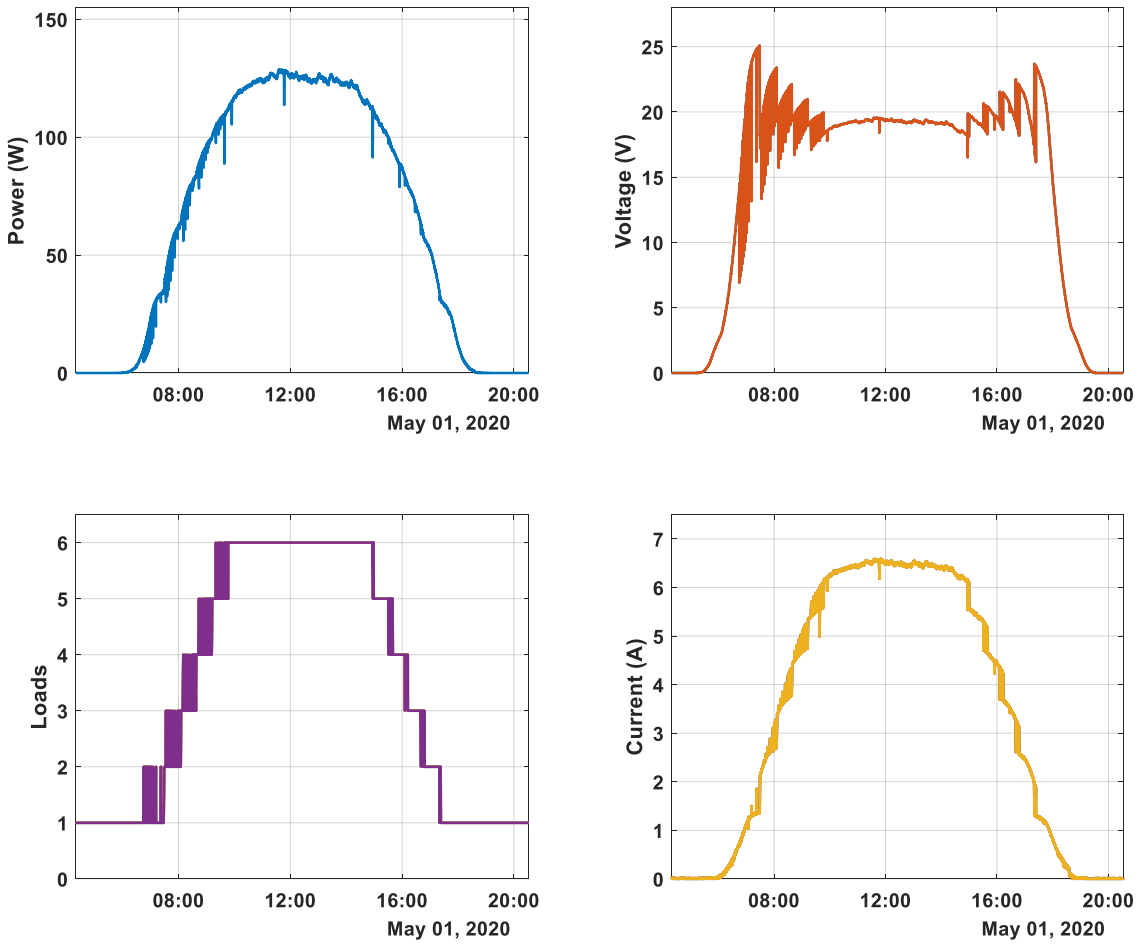

Figure 4.29. Hardware Results for the First Day of the Morning-initiated Experiment (05/01/20).

As observed in Figure 4.29, the hardware results closely resemble the simulation results from Chapter 4.2. Throughout the morning, the load-matching MPPT algorithm was operating in Mode 1, where it was attempting to learn the P_{SP} values for each of the loads. At the beginning of the experiment, the P_{SP} values were unknown, which resulted in a number of unsuccessful control actions throughout the morning. By zooming in on the first switch point from Figure 4.29 (where Load 2 was successfully connected), the performance of the algorithm can be validated, as shown in Figure 4.30.

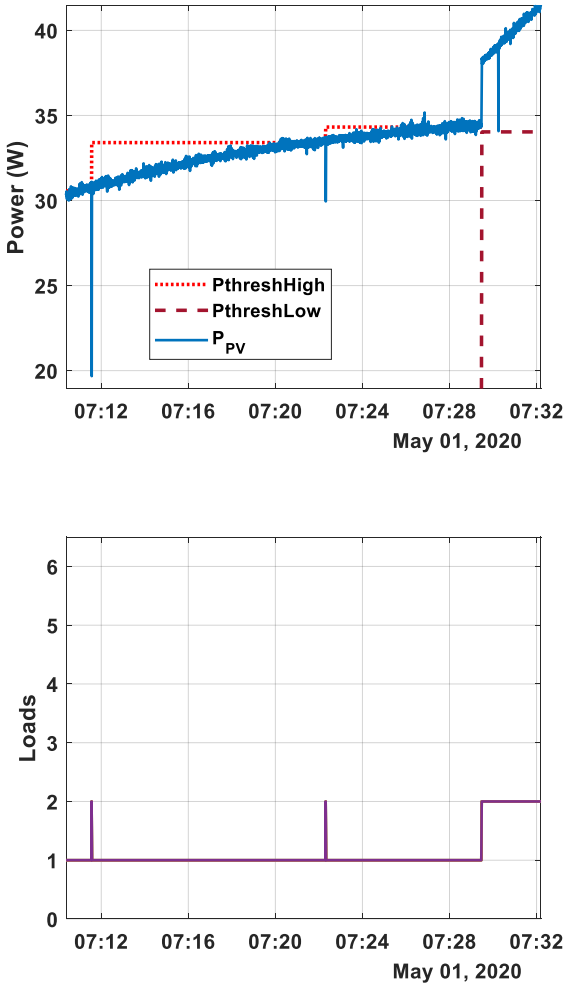

Figure 4.30. Algorithm Validation around the Successful Connection of Load 2.

Figure 4.30 shows the final two unsuccessful control actions for Load 2; after each of these actions, the PV power dropped, so the value of *PthreshHigh* was adjusted using (5), depicted by the red dotted line. After the third control action, the PV power remained above *PthreshHigh* for 3 seconds, so the controller maintained the connection of Load 2 to the PV array in parallel with Load 1. Upon the successful control action, the PV power experienced a considerable increase, indicating that the optimal P_{SP} value was actually a bit lower; optimal P_{SP} values result in a more continuous power curve, as discussed in Chapter 3.4.1. Therefore, when the algorithm updated the values of *PthreshHigh* and

PthreshLow, it stored a slightly lower value for the P_{SP} of Load 2 to try to correct for the sub-optimal switch point. This corrected value of P_{SP} was determined by taking the average value of PV power between the last two control actions. If the power increased by less than 0.5 W, i.e., less than the magnitude of the noise, no corrective action would have been taken.

Figure 4.30 also validates the sensor performance and the decision to include a time delay. While the PV power signal does contain roughly 0.5 W of noise, the controller was still able to operate successfully, as the change in power due to both successful and unsuccessful control actions was clear. Since the power signal is the product of both the voltage signal and the current signal, the amount of noise in each of those signals is compounded. For this experiment, a moving average filter was used to reduce some of the noise, but the window length was only set to 5 samples. Using a larger averaging window would likely reduce the noise in the signal even further. However, by including a time delay, the impact of the noise is reduced because the PV power signal had to remain above *PthreshHigh* for 3 seconds. The benefit of this time delay is also shown just after Load 2 was successfully connected, where another dip in power was observed in the signal. If the algorithm did not include a time delay, this momentary dip in power may have caused an unnecessary control action to be taken.

By noon, the P_{SP} values for each of the loads had been determined. Throughout the afternoon, the loads were disconnected from the PV array as the irradiance decreased and the algorithm adjusted the P_{SP} values for each of the loads in a response to the changes in temperature. Figure 4.31 shows the validation of the algorithm around the successful

disconnection of Load 2, which highlights the final two unsuccessful control actions prior to Load 2 remaining disconnected. After each unsuccessful control action that attempted to remove Load 2, the value of *PthreshLow* was adjusted to the value of power at the time when that load was unsuccessfully disconnected, as depicted by the red dashed line in Figure 4.31. After the third control action, the PV power remained above *PthreshLow* for 3 seconds and Load 2 remained disconnected. Compared to Figure 4.30, the switch point shown in Figure 4.31 resulted in a more continuous power curve, indicating that a more optimal value had been found. Therefore, no modifications were made to the value of P_{SP} stored for Load 2, as had been done the first time that value had been stored in Figure 4.30.

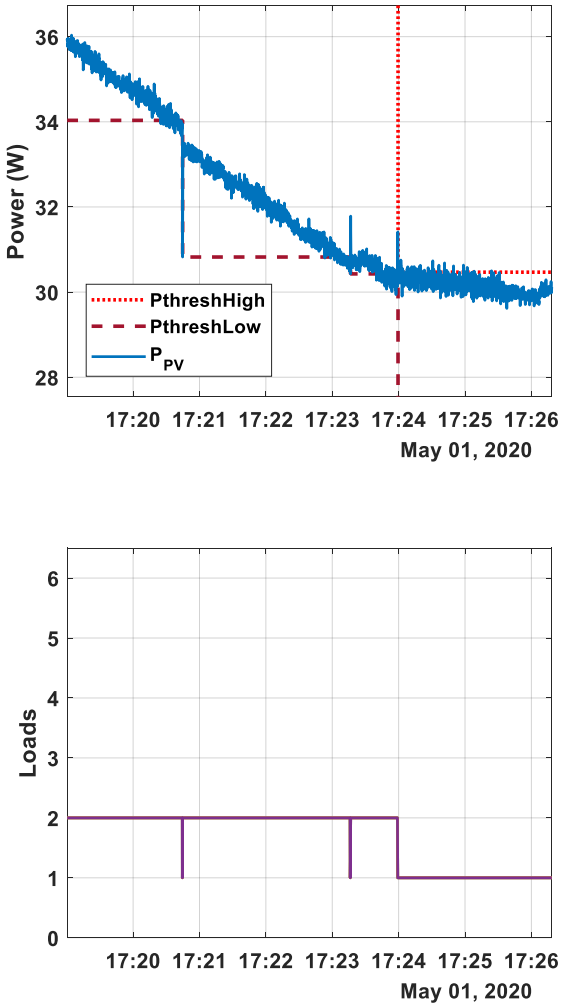

Figure 4.31. Algorithm Validation around the Successful Disconnection of Load 2.

A summary of the feedback-based LMPV system performance on the first day of the morning-initiated experiment is presented in Table 4.5. The effect of temperature on the performance of the feedback-based LMPV system can be observed by comparing the midday P_{SP} values with the final P_{SP} values for this day. Other than the first load, which was always connected to the PV array, the P_{SP} values for each of the loads during the middle of the day were greater than their final value for that day. The decrease in P_{SP} values was likely due to the temperatures in the afternoon being greater than the temperatures in the

morning. This result agrees with the simulation results in Figure 4.12 that revealed the optimal P_{SP} values are negatively correlated with temperature. In fact, after comparing the difference between the midday and final P_{SP} values, it can be observed that the difference in P_{SP} values for Load 3 (-6.47 W) was greater in magnitude than that of Load 6 (-1.80 W). This result indicates that there was a greater difference in temperature between when Load 3 was successfully connected (around 8:00) then disconnected (around 16:00) from the PV array compared to the temperature difference between when Load 6 was successfully connected (around 9:45) then disconnected (around 15:00) from the PV array. When the effect of temperature was explored in simulation, only a single step change in temperature was utilized, so each of the P_{SP} values were affected equally. However, if a more realistic temperature profile was used, the change in P_{SP} values would have likely resembled the data in Table 4.5.

Table 4.5. Summary of Results From the First Day of the Morning-initiated Experiment on 05/01/2020.

	05/01/2020 (Tempe, AZ)			
Loads	**Initial P_{SP} (W)**	**Midday P_{SP} (W)**	**Final P_{SP} (W)**	**Total Relay Actions**
1	00.00	00.00	00.00	0
2	NaN	34.03	30.47	28
3	NaN	63.29	56.82	26
4	NaN	83.63	79.31	24
5	NaN	99.63	94.56	26
6	NaN	112.02	110.22	26
	PV Energy Extracted (Wh)			
	1052.66			

The results from the second day of the morning-initiated experiment are shown in Figure 4.32. Since the P_{SP} values for each of the loads had already been determined from the previous day, the algorithm started the day operating in Mode 2. Similar to the

simulation results in Figure 4.12, the algorithm adjusted the P_{SP} values from the previous day because the morning temperatures were now less than the afternoon temperatures from the previous day. By adjusting the P_{SP} values throughout the morning, some unsuccessful control actions had to be taken, but not as many as were needed compared to the first day when the algorithm was operating in Mode 1 and P_{SP} values were completely unknown.

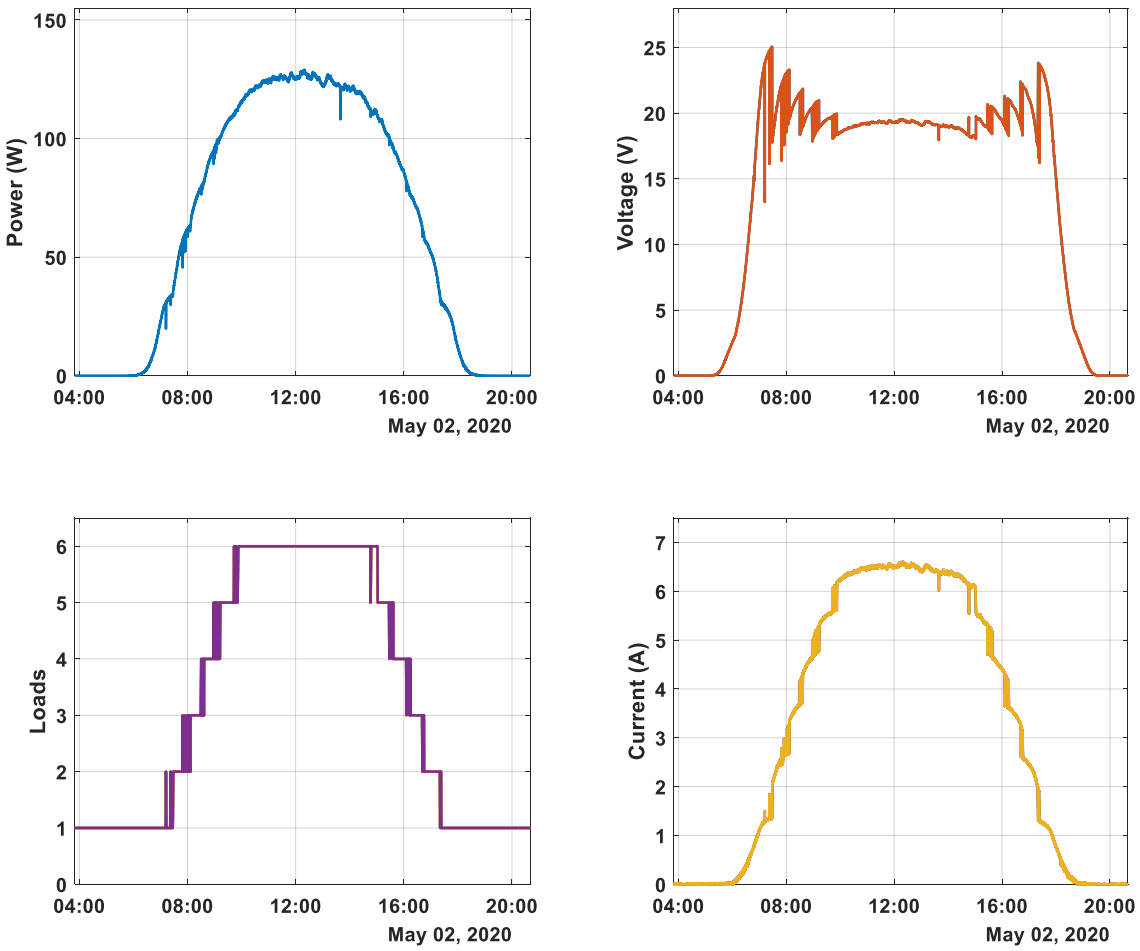

Figure 4.32. Hardware Results for the Second day of the Morning-initiated Experiment (05/02/20).

A comparison of the feedback-based LMPV system performance over the two days of the morning-initiated experiment is presented in Table 4.6. As expected, there was a

reduction in the total relay actions per load on the second day compared to the first day, as the controller already had fairly accurate estimates of the optimal P_{SP} values at the start of the second day. While the changes in temperature did cause the P_{SP} values to change throughout the two-day experiment, the load-matching MPPT controller was able to accurately track those changes.

Table 4.6. Comparison of Performance Over the Two Days of the Morning-initiated Experiment.

	05/01/2020 (Tempe, AZ)				05/02/2020 (Tempe, AZ)			
Loads	**Initial P_{SP} (W)**	**Midday P_{SP} (W)**	**Final P_{SP} (W)**	**Total Relay Actions**	**Initial P_{SP} (W)**	**Midday P_{SP} (W)**	**Final P_{SP} (W)**	**Total Relay Actions**
1	00.00	00.00	00.00	0	00.00	00.00	00.00	0
2	NaN	34.03	30.47	28	30.47	33.74	30.31	14
3	NaN	63.29	56.82	26	56.82	62.80	57.48	14
4	NaN	83.63	79.31	24	79.31	81.92	76.10	16
5	NaN	99.63	94.56	26	94.56	100.34	95.39	22
6	NaN	112.02	110.22	26	110.22	112.16	109.78	12
	PV Energy Extracted (Wh)				**PV Energy Extracted (Wh)**			
	1052.66				1046.29			

Although the P_{SP} values varied significantly over the two-day experiment, the midday P_{SP} values from each day were fairly similar for each of the loads, and the same holds for the final P_{SP} values from each day. This result supports the claim that the algorithm was performing as expected but also suggests room for improvement in the tracking algorithm to further reduce the number of unsuccessful control actions. For example, if the temperature was also being measured and stored alongside the P_{SP} values, the algorithm could learn the correlation between the P_{SP} values and temperature to continuously modify the P_{SP} values as the temperature changed throughout the day, likely leading to a reduction in unsuccessful control actions and thus a reduction in total relay actions per load.

In the simulation results, it was shown that the total PV energy extracted from the module was only marginally reduced in the presence of the increased relay actions experienced during the Mode 1 operation of the algorithm. In Table 4.6, PV energy extracted was greater on the first day, even though the total relay actions were greater. This result indicates that the PV energy was likely reduced on the second day due to the ambient conditions at the PV array, rather than by the algorithm. Thus, it is difficult to draw any significant conclusions from the PV energy metric in the hardware experiments because the ambient conditions are not being controlled as they were in the simulation results.

4.4.2 Afternoon-initiated Experiment

The experiment in Chapter 4.4.1 was initiated in the morning, but the algorithm is able to learn the P_{SP} values regardless of when the experiment was initiated. To demonstrate this capability, a similar experiment was conducted after initiating the load-matching MPPT controller in the afternoon of 04/24/2020. The experiment was then continued until the end of the following day.

Instead of learning the P_{SP} values as the PV power increased throughout the morning, the P_{SP} values were learned as the power decreased in the afternoon. Since there was PV power available from the moment the experiment had started, the algorithm first tested each combination of loads to determine its starting point, as shown in Figure 4.33. The initialization routine started by connected all 6 loads to the PV array in parallel and temporarily stored the PV power as the P_{SP} value for Load 6. Then, the loads were disconnected from the PV array, one by one, and the P_{SP} values were temporarily stored

accordingly. Since the PV power was greatest at 6 loads, the algorithm reconnected all 6 loads back to the PV array after the initialization routine had finished and set the value of *PthreshLow* equal to the value of P_{SP} of Load 5.

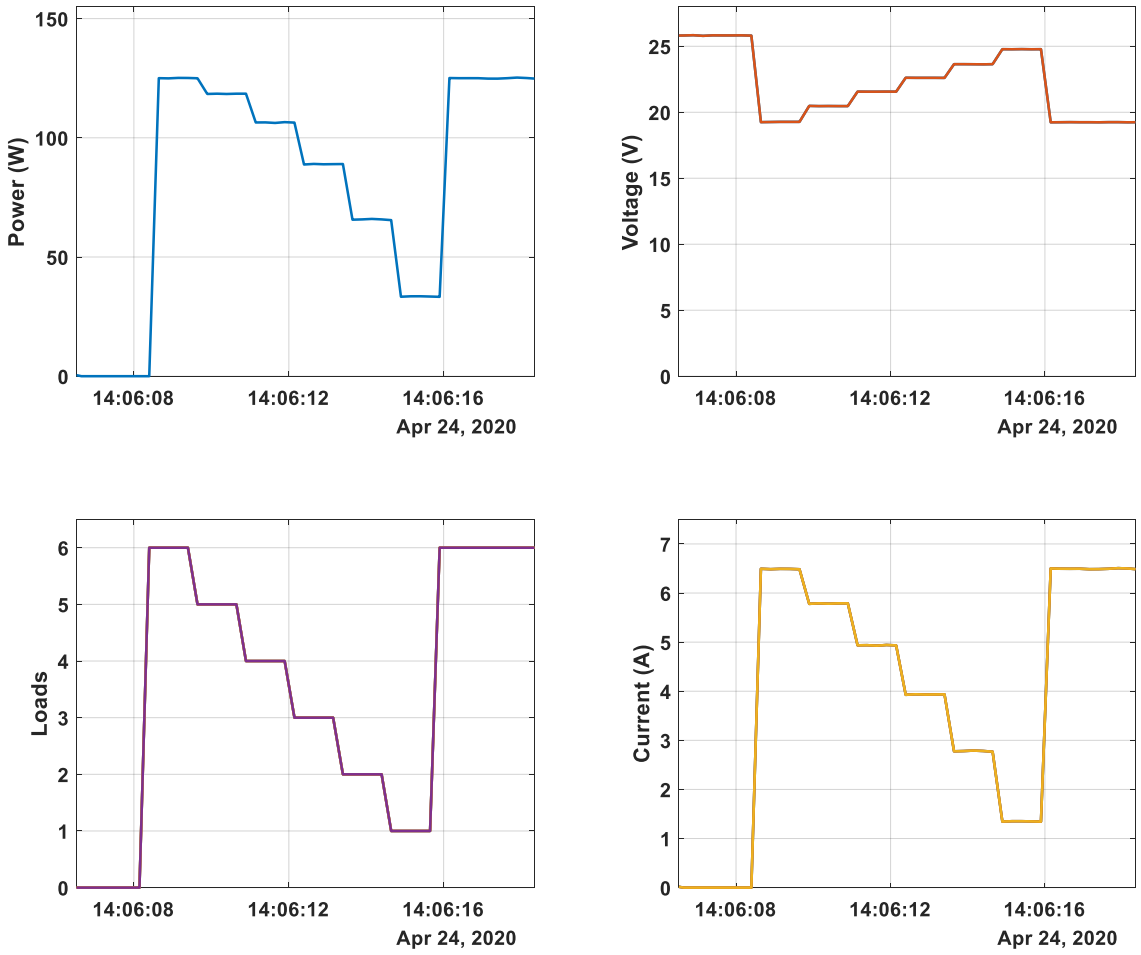

Figure 4.33. Initialization Routine Executed when PV Power is Available at the Start of the Experiment.

After the initialization routine ended, the algorithm returned to its normal operating mode for the remainder of the day. Being that estimates of the P_{SP} values for each of the loads had been determined during the initialization routine, the algorithm was able to operate in Mode 2. The results from the first day of the afternoon-initiated experiment are

presented in Figure 4.34. After each unsuccessful control action, the value of *PthreshLow* was adjusted, as explained in the discussion of Figure 4.31, until a successful control action occurred. By the end of the day, the algorithm had successfully updated the P_{SP} values for each of the loads.

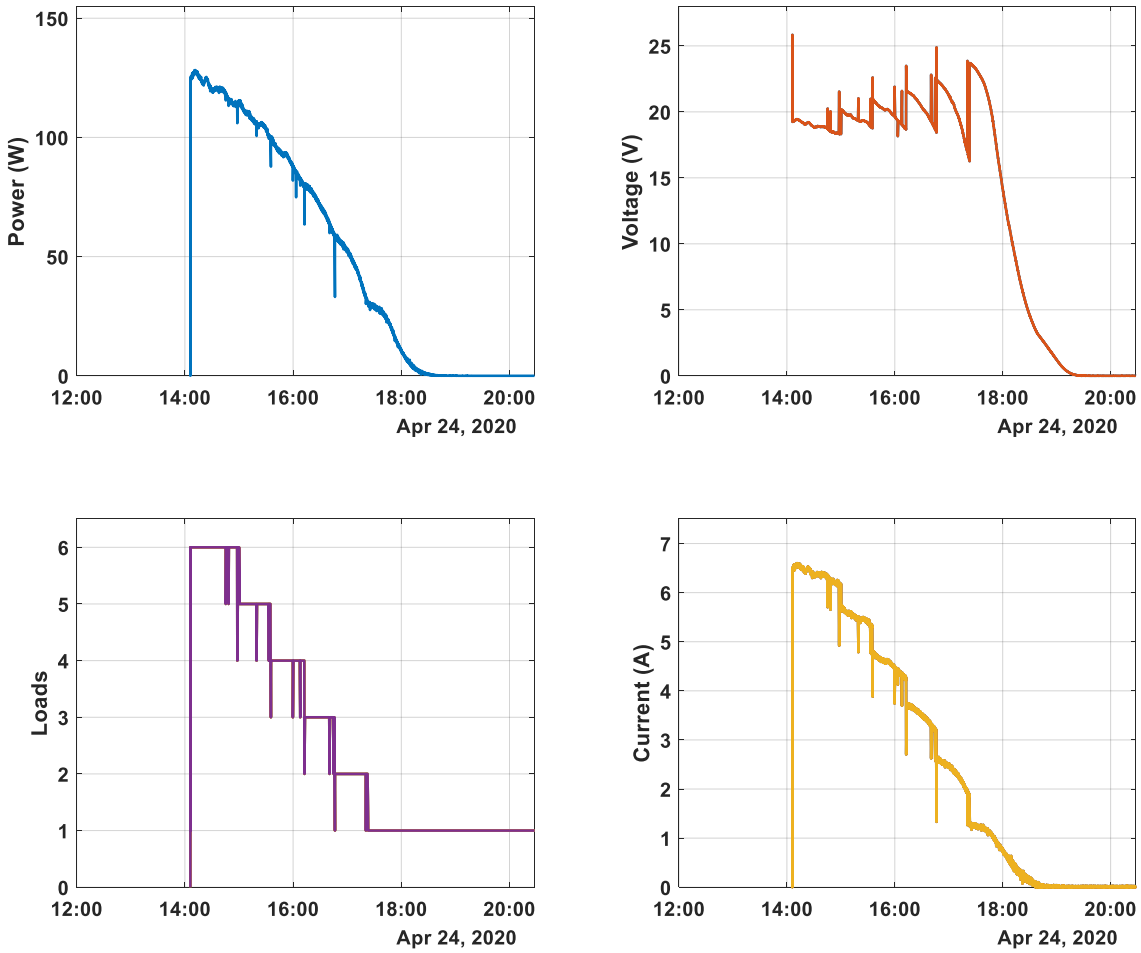

Figure 4.34. Hardware Results for the First Day of the Afternoon-initiated Experiment (04/24/20).

The performance of the feedback-based LMPV system on the first day of the afternoon-initiated experiment is summarized in Table 4.7. The midday P_{SP} values were considerably higher during the afternoon-initiated experiment compared to the morning-

initiated experimental results in Table 4.5. This result is in line with expectations because the P_{SP} values were determined through the initialization routine that was initiated in the early afternoon around 14:00. For example, during the morning-initiated experiment, the P_{SP} value for Load 2 was determined around 7:30 when the irradiance was significantly less than at 14:00. However, despite the discrepancy of the midday P_{SP} values, the final P_{SP} values for the afternoon-initiated experiment were close to those of the morning-initiated experiment, indicating that the algorithm was able to successfully adjust the P_{SP} values for each of the loads by the end of the day.

Table 4.7. Summary of Results from the First Day of the Afternoon-initiated Experiment on 04/24/2020.

	04/24/2020 (Tempe, AZ)			
Loads	**Initial P_{SP} (W)**	**Midday P_{SP} (W)**	**Final P_{SP} (W)**	**Total Relay Actions**
1	00.00	00.00	00.00	0
2	NaN	65.78	30.43	8
3	NaN	88.95	58.68	12
4	NaN	106.57	79.75	10
5	NaN	118.51	99.95	12
6	NaN	125.10	113.81	16
	PV Energy Extracted (Wh)			
	312.67			

The results in Table 4.7 also reveal that the total relay actions per load were significantly reduced compared to the morning-initiated experimental results. Part of the reduction in relay actions can be attributed to the fact that the experiment was conducted for less than half of a full day. However, most of the loads experienced less than half of the relay actions compared to the morning-initiated experiment, which suggests that the algorithm was able to learn the P_{SP} values more efficiently as the power was decreasing throughout the afternoon as opposed to when the power was increasing in the morning.

These subtle differences were expected since the functions for updating the *PthreshHigh* and *PthreshLow* values are slightly different for when the power is increasing versus when power is decreasing.

The results from the second day of the morning-initiated experiment are shown in Figure 4.35. Since the P_{SP} values for each of the loads had already been determined from the previous day, the algorithm started the day operating in Mode 2. The algorithm once again adjusted the P_{SP} values from the previous day in response to the temperature differences. Figure 4.35 also shows that the algorithm responded to a dip in power around 14:00 and again around 16:20 (likely due to partial cloud coverage), but both instances resulted in unsuccessful control actions, indicating that the duration and/or magnitude of the cloud coverage was not very significant.

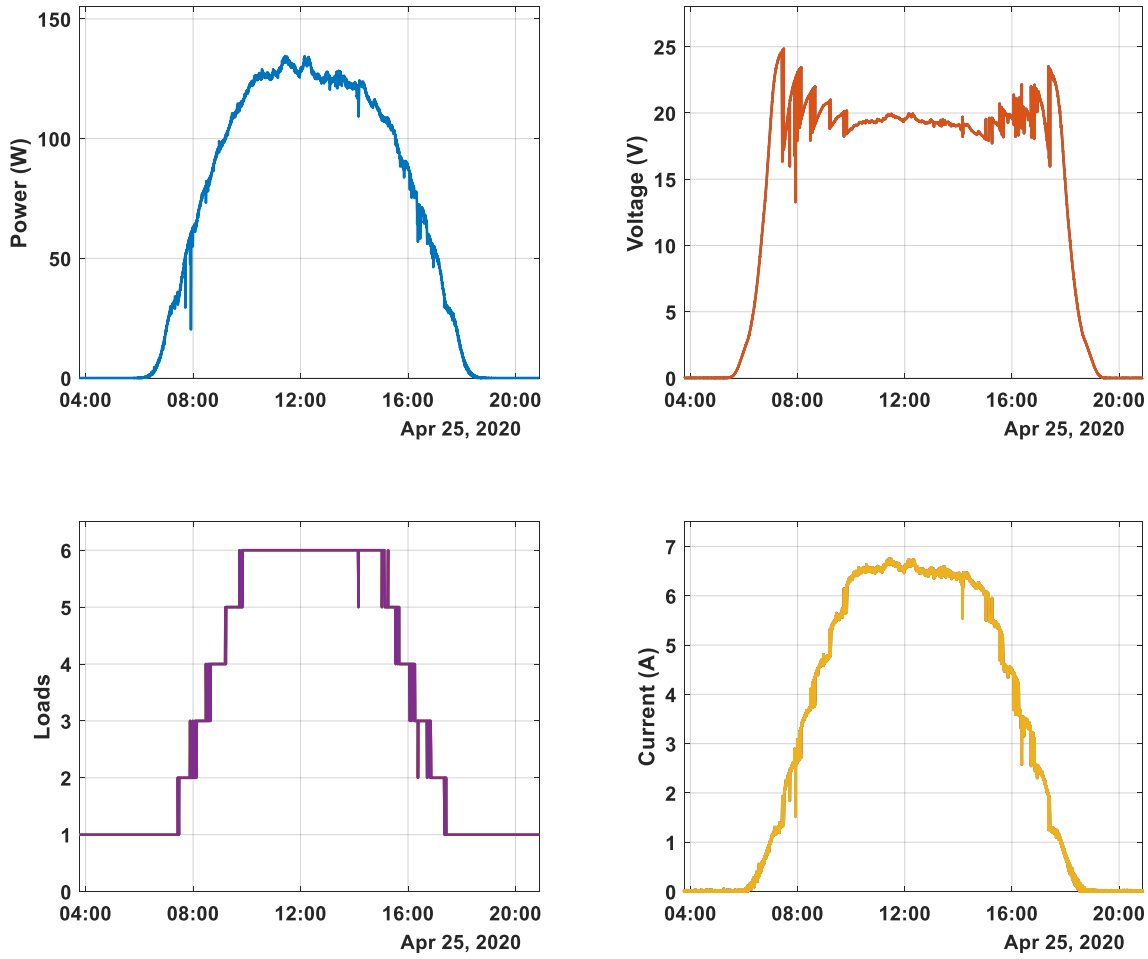

Figure 4.35. Hardware Results for the Second Day of the Afternoon-initiated Experiment (04/25/20).

A comparison of the feedback-based LMPV system performance over the two days of the afternoon-initiated experiment is presented in Table 4.8. Unlike the morning-initiated experiment, there was an increase in the total relay actions per load on the second day compared to the first day because the experiment on the first day started more than halfway through the day. While the changes in temperature did cause the P_{SP} values to change throughout the two-day experiment, the load-matching MPPT controller was able to accurately track those changes.

Table 4.8. Comparison of Performance Over the Two Days of the Afternoon-initiated Experiment.

	04/24/2020 (Tempe, AZ)				04/25/2020 (Tempe, AZ)			
Loads	**Initial P_{SP} (W)**	**Midday P_{SP} (W)**	**Final P_{SP} (W)**	**Total Relay Actions**	**Initial P_{SP} (W)**	**Midday P_{SP} (W)**	**Final P_{SP} (W)**	**Total Relay Actions**
1	00.00	00.00	00.00	0	00.00	00.00	00.00	0
2	NaN	65.78	30.43	8	30.43	33.94	29.47	20
3	NaN	88.95	58.68	12	58.68	64.44	56.57	16
4	NaN	106.57	79.75	10	79.75	83.90	76.82	22
5	NaN	118.51	99.95	12	99.95	100.67	92.76	12
6	NaN	125.10	113.81	16	113.81	114.93	108.01	12
	PV Energy Extracted (Wh)				**PV Energy Extracted (Wh)**			
	312.67				1058.54			

The energy extracted from the PV array during the second day of the afternoon-initiated experiment was greater than that for the second day of the morning-initiated experiment. Again, this difference is likely due to the daily temperature differences throughout the days, as the afternoon-initiated experiment was conducted about a week before the morning-initiated experiment.

4.4.3 Days with Variable Irradiance

Once the hardware implementation of the feedback-based LMPV controller had been validated, the experiments were repeated several times to ensure the system continued to operate properly and to collect additional data. The experiments conducted in Chapter 4.4.1 and Chapter 4.4.2 took place during nearly completely sunny days, which facilitated the analyses and explanations of the system's performance. However, the feedback-based LMPV system also operated successfully on cloudy and partially cloudy days.

Figure 4.36 presents the results for an experiment conducted on 05/06/2020, in which the P_{SP} values had already been learned from the previous day. The load-matching

MPPT controller adjusted the P_{SP} values from the previous day throughout the morning and successfully connected Load 6 by the late morning. Just after midday, the PV array began to experience cloud coverage, which decreased the power output of the array. In response to the rapid drop in PV power, the load-matching MPPT controller began to disconnect loads—in some cases dropping the number of connected loads down to 4 and even testing the disconnection of the 4th load. It can also be observed that the daily peak in PV power of 127.9 W occurred at 13:05, i.e., after solar noon, due to the effects of cloud enhancement.

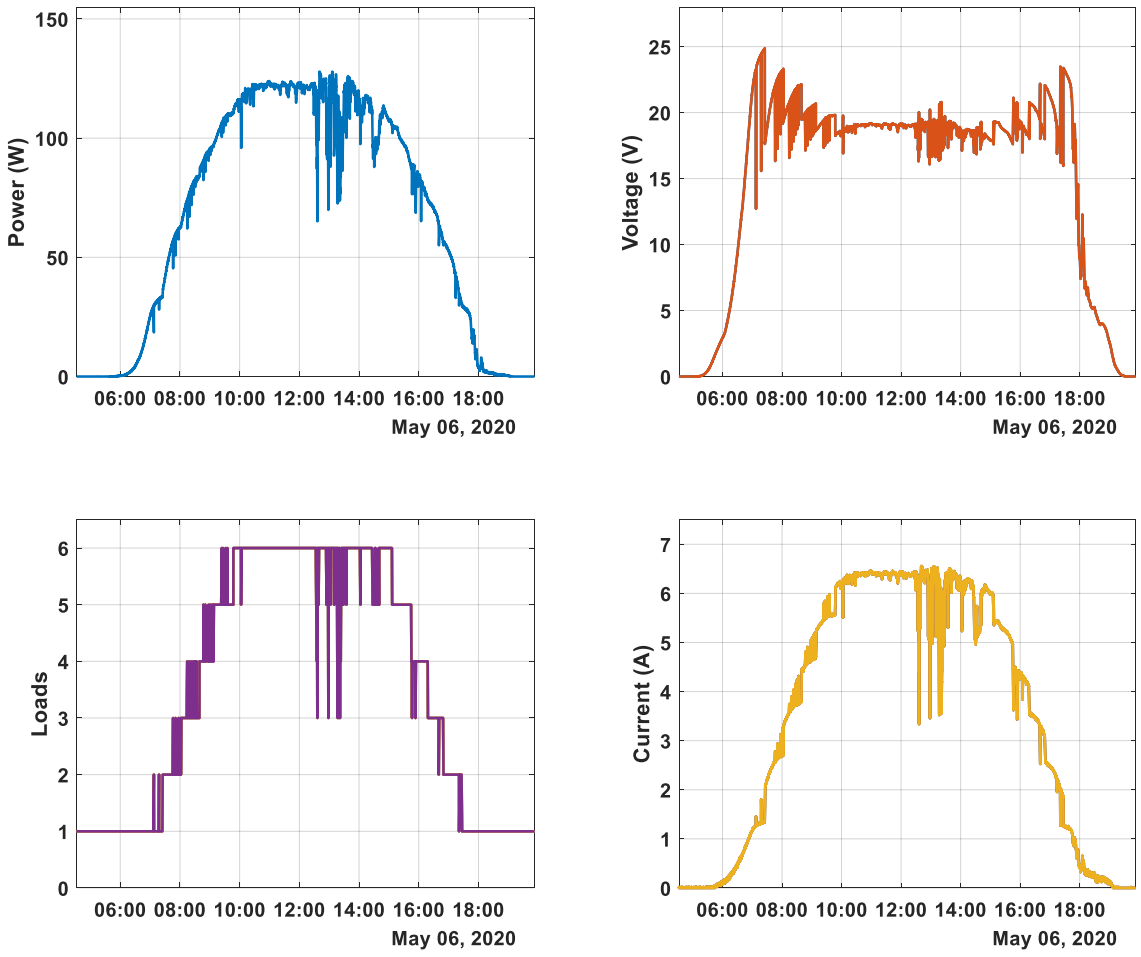

Figure 4.36. Hardware results for the Experiment Conducted on 05/06/2020.

By zooming in on one of the drops in power, the performance of the load-matching MPPT algorithm under varying irradiance conditions can be verified, as shown in Figure 4.37. As the power began to drop, a successful control action was taken to remove Load 6. Then, as the power dropped further, the system experienced an unsuccessful control action when it attempted to remove Load 5, which manifested as a negative spike in the power subplot of Figure 4.37. After a couple of oscillations between 5 and 6 connected loads, Load 5 was successfully disconnected at 12:36. From there, the controller attempted to remove Load 4 two times, but both were unsuccessful and resulted in negative spikes in the power subplot. Eventually, the cloud coverage dispersed, and all 6 loads were able to be reconnected. Overall, the controller continued to operate as expected, even amid rapidly varying irradiance conditions.

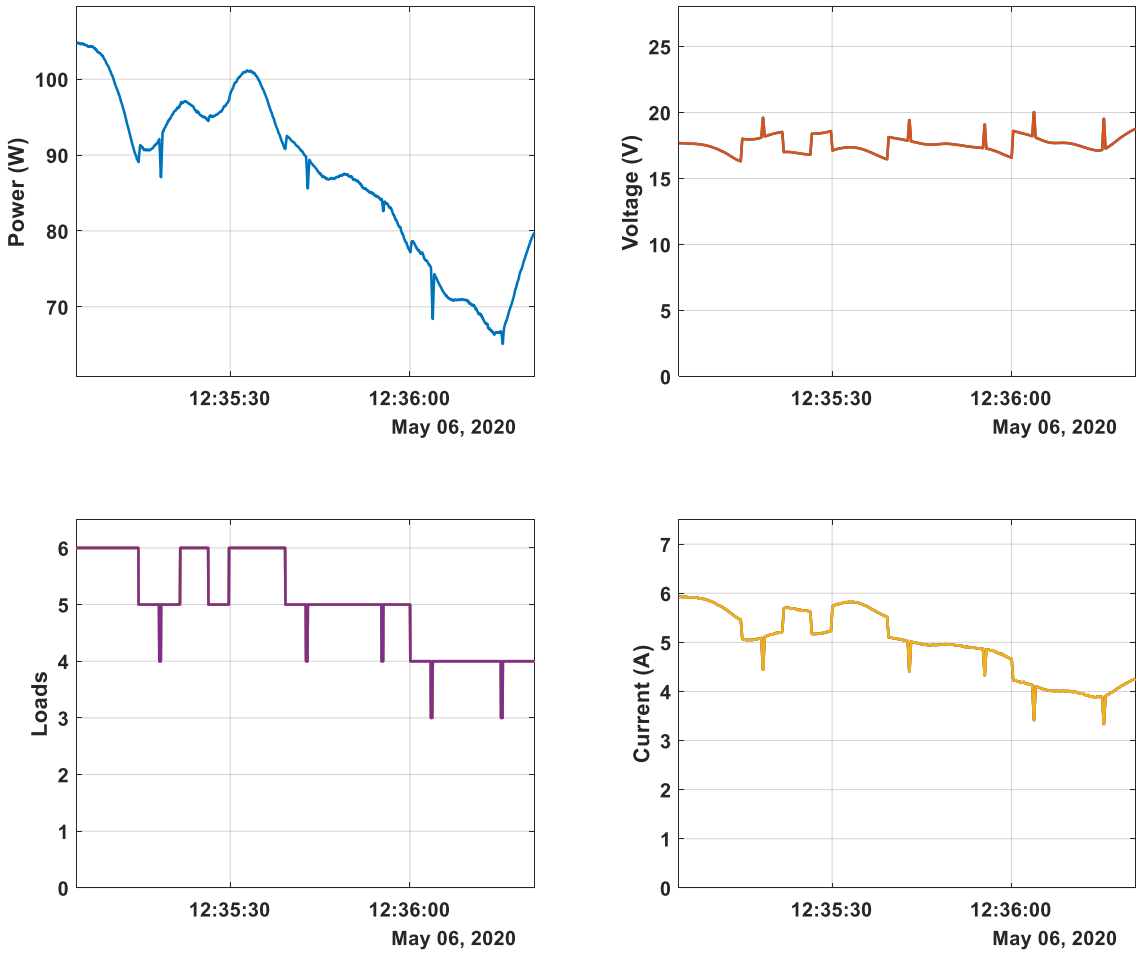

Figure 4.37. Validation of Load-matching MPPT Algorithm Performance under Varying Irradiance.

The performance of the feedback-based LMPV system on 05/06/2020 is summarized in Table 4.9. As expected, the total number of relay actions taken per load was significantly increased, especially for Loads 4, 5, and 6. Being that the majority of the cloud coverage occurred in the early afternoon when the available PV power is near its maximum, the variability in irradiance during this time caused the greatest increase in relay actions for Load 6, whereas the relay actions for Load 2 were not affected. The cloud coverage also reduced the amount of PV energy extracted throughout the day compared to the results of the second day of the experiments in Table 4.6 and Table 4.8.

Table 4.9. Summary of Results from the Experiment Conducted on 05/06/2020.

	05/06/2020 (Tempe, AZ)			
Loads	**Initial P_{SP} (W)**	**Midday P_{SP} (W)**	**Final P_{SP} (W)**	**Total Relay Actions**
1	00.00	00.00	00.00	0
2	29.46	32.99	29.64	8
3	56.65	63.03	56.52	16
4	73.89	83.96	73.64	34
5	90.51	96.81	88.89	44
6	106.00	109.96	104.59	142
	PV Energy Extracted (Wh)			
	1016.73			

The experiment conducted on 05/06/2020 revealed that the feedback-based LMPV system was able to operate properly in the presence of rapidly changing irradiance. In that experiment, the P_{SP} values had already been stored from the operation of the system on a previous day. Another experiment was conducted on a very cloudy day (04/30/2020), in which the P_{SP} values were unknown at the beginning of the experiment. The results of this experiment are presented in Figure 4.38.

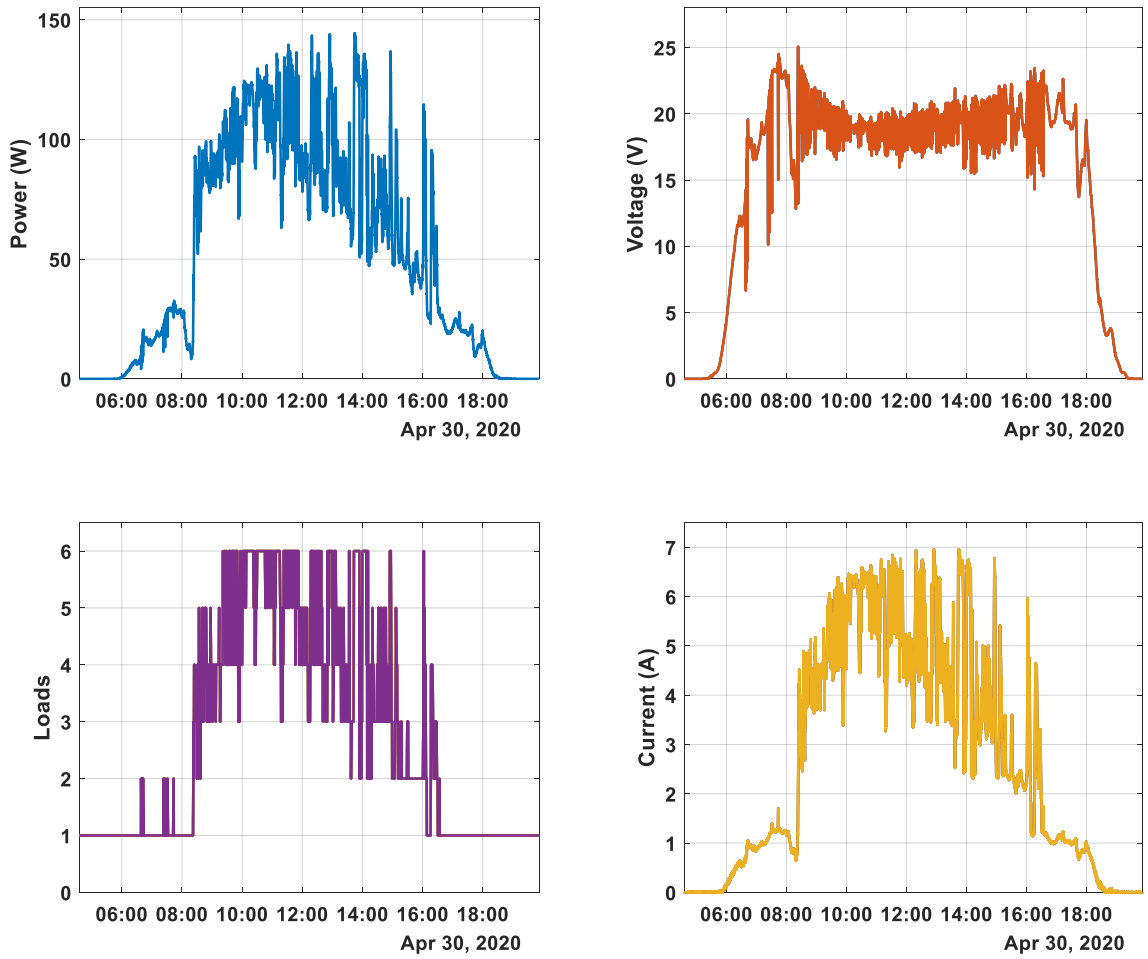

Figure 4.38. Hardware Results for the Experiment Conducted on 04/30/2020.

For the experiment in Figure 4.38, the load-matching MPPT controller had the added challenge of learning the P_{SP} values for each of the loads under highly-variable irradiance conditions due to the cloudy weather. While the variability made it more difficult to validate the performance of the load-matching MPPT controller, several key observations indicated the algorithm had worked properly. First, the Loads subplot in Figure 4.38 shows that the controller had just one load connected at the beginning of the day, then all 6 loads were connected by around 10:00 (similar to the results from the clear-

sky experiments) and ultimately returned to having just one load connected by the end of the day.

Another indication that the algorithm performed properly can be observed in the voltage subplot of Figure 4.38. Although the voltage appeared noisy due to the varying irradiance, the voltage remained around the maximum power point voltage throughout the entire middle portion of the day (i.e., roughly 19 V as seen in the results from the clear-sky experiments). If at any point the controller removed too many loads, positive spikes in the voltage would have been observed as the operating point of the PV array would have shifted closer to its open-circuit voltage; the opposite would also have been true if the controller had connected too many loads.

Other results from the experiment conducted on 04/30/2020, summarized in Table 4.10, also indicate the algorithm worked properly. Even in the presence of highly variable irradiance, the load-matching MPPT controller was able to determine the P_{SP} values for each of the loads, which were very similar in magnitude to the experimental results from the clear-sky experiments for both the midday and final values. As expected, the most significant change in performance is observed in the effect on total relay actions for each of the loads. Other than Loads 1 and 2, all the loads experienced a significant increase in relay actions, with Load 5 experiencing 448 relay actions. While the magnitude of total relay actions was greatly increased, the cumulative effect on the output PV energy was likely still negligible compared to the effect of the cloud coverage. Also, if solid-state relays are used, the increased number of relay actions due to the highly variable irradiance is negligible, as those relays are designed to change states thousands of times per second.

Table 4.10. Summary of Results from the Experiment Conducted on 04/30/2020.

	04/30/2020 (Tempe, AZ)			
Loads	**Initial P_{SP} (W)**	**Midday P_{SP} (W)**	**Final P_{SP} (W)**	**Total Relay Actions**
1	00.00	00.00	00.00	0
2	NaN	34.18	28.79	38
3	NaN	63.00	54.58	132
4	NaN	73.22	80.45	296
5	NaN	92.84	101.82	448
6	NaN	107.91	111.42	446
	PV Energy Extracted (Wh)			
	787.01			

Figure 4.38 also highlights the effect of cloud enhancement on the output power of the PV array. The daily peak output power of the PV array reached a magnitude of 144.4 W—significantly greater than the daily peak values of the clear-sky experiments. The daily peak also occurred at 13:44, which is considerably after solar noon for that day. One specific instance of the cloud enhancement that occurred towards the end of the daylight hours (just after 16:00) caused the system to operate with 5 loads connected for a few minutes and even check the connection of Load 6, which was typically remained disconnected after 15:00.

4.4.4 Discussion of Hardware Results

The design and implementation of the feedback-based LMPV system in hardware were successfully validated through multiple day-long experiments under both clear-sky and cloudy conditions. Regardless of the time of day in which it was initiated, each experiment resulted in the load-matching MPPT controller successfully identifying the P_{SP} values for each of the loads. As expected, changes in the ambient temperatures around the

PV array caused the optimal P_{SP} values to change, but the controller was able to track those changes and update the P_{SP} values accordingly over time. The sensors provided accurate and consistent measurements of the PV array output power, with an acceptable signal to noise ratio, that allowed the controller to determine if a control action resulted in an increase or decrease in PV power. Overall, the results of the hardware experiments closely matched the results and behaviors observed in the simulated experiments and provided sufficient evidence to support the viability of a load-matching MPPT controller.

While the feedback-based LMPV system was successfully implemented and validated in hardware, there are several aspects of the system that could be improved in future iterations of the system. First, the level of noise in the voltage and current measurements could be addressed, either through digital signal processing techniques or through hardware improvements. For the improvement of the signal processing, increasing the sampling rate and/or increasing the averaging window would likely result in a reduction in noise. Due to limitations in the software support of the USB-6001 DAQ in Simulink, the sampling rate had to be equal to the time step of the simulation. Therefore, while utilizing a DAQ to acquire the signals from the voltage and current sensors provided a flexible solution, a more sophisticated solution would be to have a dedicated ADC for each sensor that was optimized for the range of expected values; the USB-6001 had a standard ±10 V input range, which is quite large compared to other commercially available ADCs. Digitizing the measurements earlier in the signal chain would also result in fewer opportunities for noise to enter the signal. By reducing signal noise, there would also be less of a need for the time delays in the control algorithm, potentially improving the accuracy in determining and updating the P_{SP} values over time.

Aside from the signal chain improvements, the load-matching MPPT algorithm also has room for improvement. The simulation and hardware results both revealed that temperature had a significant effect on the optimal P_{SP} values for each of the loads, where higher temperatures caused a reduction in the P_{SP} values. It was observed that the P_{SP} values varied significantly from their midday values to their final values for the same day but did not vary much from one day to the next. The effect of temperature on the P_{SP} values can be addressed either directly, by including temperature measurement, or indirectly, by storing the time values for each P_{SP} value. If a temperature sensor was utilized, the P_{SP} values could be continuously modified as temperature changes, after the precise relationship to temperature had been learned (perhaps through the implementation of a simple regression). Without a temperature sensor, a similar correction could be implemented based on the time at which each P_{SP} value was determined. However, the utilization of direct compensation through the use of a temperature sensor would likely provide a more robust solution as variable irradiance conditions may pose an additional challenge for the indirect method.

The load-matching MPPT algorithm used in the hardware implementation of the feedback-based LMPV system was similar to the P&O algorithm discussed in Chapter 2.1. However, being that measurements of the PV array current, voltage, and power are available to the controller, it would be possible to implement a modified version of some of the more sophisticated MPPT algorithms, like the IncCond algorithm. These advanced algorithms could also provide reductions in the unsuccessful control actions taken by the load-matching MPPT algorithm.

Another useful feature that can be incorporated into the feedback-based LMPV system is voltage regulation. For each of the experiments on the hardware implementation of the feedback-based LMPV system, there were no restrictions placed on the operating voltage of the output power from the PV array, and as a result, there was a wide range of voltages applied to the loads throughout each experiment—especially during the early mornings and late afternoons. Depending on the application, the voltage applied to the loads may have to be limited to a certain range. As discussed in Chapter 3.3.4, the LMPV system can incorporate voltage regulation by modifying the switch points of the loads, but as the requirements on operating voltage become stricter, the energy yield of the system may be sacrificed. However, it was previously shown that as more loads are made available to the system to manage, voltage regulation has less of an effect on the energy yield of the system.

Being that the output voltage of the PV array is already being measured, voltage regulation can be incorporated into the load-matching MPPT control algorithm; when the algorithm checks whether or not a control action was successful, it can also check to make sure the voltage is within the allowable range. If so, the control action would be considered successful, and if not, the control action would be unsuccessful. Therefore, in theory, only the control algorithm would have to be modified to incorporate voltage regulation, rather than having to modify any hardware components.

5 APPLICATIONS

The differences between the LMPV system and conventional PV systems can lead to significant cost savings in utilizing PV electricity for several practical applications. Furthermore, due to the limited availability of grid-forming inverters and DC-DC converters with MPPT functionality, the LMPV system also simplifies the use of PV electricity in remote and/or high-power DC applications. While nearly all new PV installations in the US and other developed countries are grid-connected systems, there is substantial demand for off-grid PV systems in developing countries to power applications like water pumps and refrigeration systems. According to the World Bank, the off-grid solar sector has expanded into a $1.75 billion annual market, but an estimated $6.6 - $11 billion is required to achieve universal electricity access (World-Bank, 2020).

LMPV systems can be implemented to address the rising demand for off-grid solar installations. Typically, off-grid PV systems require additional balance-of-systems components like batteries and power conditioners. However, by implementing an LMPV system, the need for additional balance-of-systems components is reduced because the LMPV system can perform the MPPT functionality and voltage regulation. Thus, LMPV systems can be designed for irrigation and refrigeration applications at a reduced cost compared to conventional PV systems. For these applications, each pump or refrigeration unit would be managed by the PV system such that the objective of the application is satisfied by multiple smaller pumps/refrigeration units as opposed to using one large centralized unit.

While the analyses of the LMPV system in Chapter 3 and Chapter 4 focused on stand-alone implementations, the LMPV system can also be backed by a secondary power such, e.g., the electric grid, to eliminate the intermittency in the power available from the PV array.

An example of a grid-backed LMPV system for DC applications is presented in Figure 5.1. In this example, the stand-alone LMPV system is modified by including an additional relay per load and a centralized AC/DC rectifier circuit. Depending on the number of loads and the power rating of the rectifier circuit, the system could also be designed with each load having a dedicated rectifier circuit. Typically, the cost of any electrical component increases with its power and thermal rating, so having individual rectifiers for each load would likely become economical at a certain point as the number of loads, and thus the total power rating, increases.

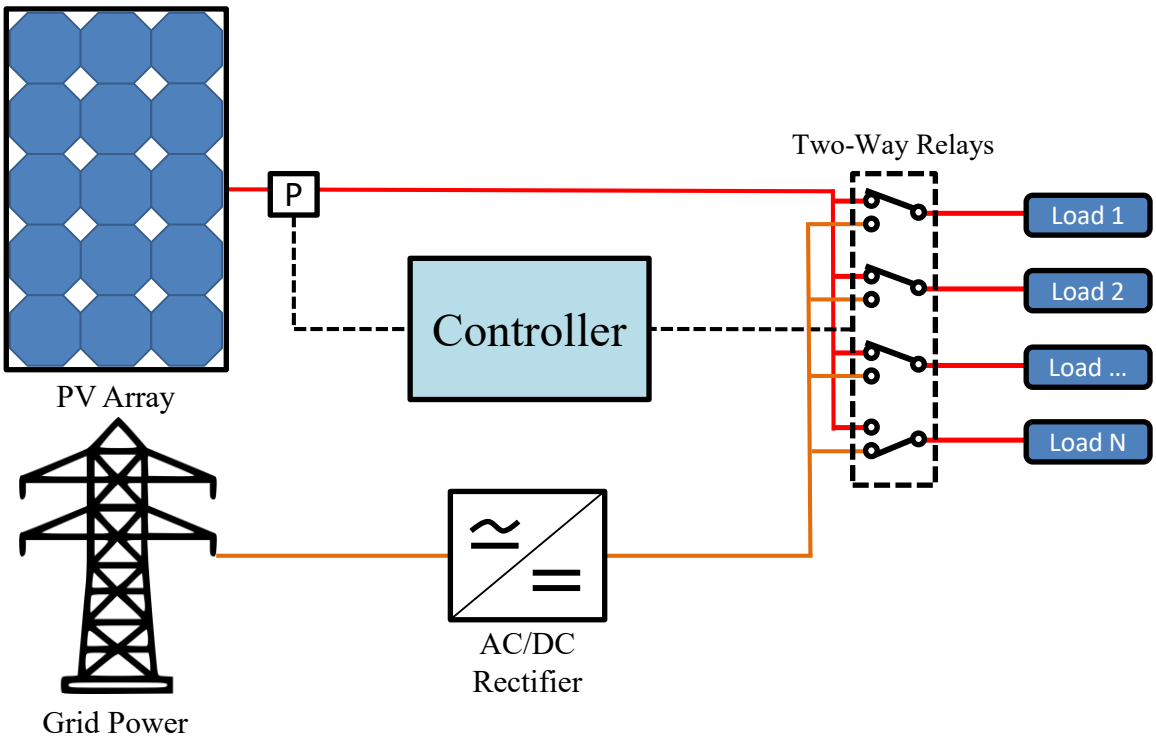

Figure 5.1. Grid-backed LMPV System for DC Applications.

The LMPV system in Figure 5.1 incorporates the load-matching MPPT controller, but can also route power from the grid to certain loads if the PV array output is insufficient to power all the loads on its own. This system still utilizes the maximum available power from the PV array, but takes supplemental power from the grid or another secondary power source, if necessary. For example, in Figure 5.1, the load-matching MPPT controller determined there was enough PV power to support the first three loads, while the last load was being powered by the grid. Overall, the ability to incorporate a secondary power source into the LMPV system increases the flexibility of the system and allows for even more potential applications to be explored.

While the LMPV system can be modified in several ways to support different types of loads and applications, the modifications may infringe upon the inherent benefits of the

LMPV system. For example, the grid-backed LMPV system in Figure 5.1 only requires a few supplemental components that would only marginally increase the initial cost of the system, without affecting the energy yield of the LMPV system, because the supplemental power is only flowing in one direction—from the secondary source to the loads. In contrast, if a grid-connected inverter was to be added to the system to provide excess PV power to the grid, implementing a conventional PV system topology may be more economical. Therefore, applications that require few, if any, modifications are generally more compatible with LMPV systems.

Applications that are best suited for LMPV systems have several characteristics in common: the application can be powered by DC electricity, can tolerate a wide range of operating voltages, and can tolerate intermittent access to power. Applications that rely on electrochemical processes, like battery charging and electrolysis, are therefore highly compatible with the LMPV system, in theory. Moreover, both battery charging and electrolysis have the potential to play an increasing role in the decarbonization of the global energy infrastructure—electric vehicles (EVs) with large battery banks offer an alternative to vehicles with internal-combustion engines and electrolysis can be used to produced hydrogen fuel for long-term energy storage.

While battery charging, for either EVs or storage batteries, is certainly an interesting and relevant application of the LMPV system, the implementation does require several significant modifications to the underlying LMPV system. These modifications are discussed in Chapter 5.1. The application of the LMPV system for powering electrolytic

processes does not require any modifications and was therefore investigated in more detail through additional modeling and simulation, presented in Chapter 5.2.

5.1 Electric Vehicle and Storage Battery Charging

Cars and trucks contribute 22% to total carbon emissions in the U.S. and 17% globally (Roston, 2016). The electric vehicle is one potential solution to this problem. However, the environmental benefit of EVs is arguable when charged by the electric grid, as 67% of grid electricity is currently derived from fossil fuels in the U.S. (EIA, 2020). Therefore, significant carbon reduction can be achieved if electric vehicles are charged directly with photovoltaics. Specifically, LMPV systems could be implemented for EV charging to provide a cost-reduced alternative to conventional PV systems.

For this application, a grid-backed LMPV system would be better suited than a stand-alone system to ensure each EV receives as much charging as possible. Being that the performance of LMPV systems improves with the number of loads (or EVs in this case), a centralized charging station would be most beneficial. For instance, the grid-backed LMPV charging station could be located at the workplace or shopping centers. By adding a secondary power source, a full charge can be guaranteed to each vehicle by the end of the day.

To illustrate the benefits of this system, let us examine the example of EVs charging at the workplace. Most vehicles will stay until about 5:00 p.m. and therefore, not every vehicle needs to start charging as soon as they arrive in the morning. The load-managing system would manage the number of EVs connected to the PV array throughout the day as

the amount of available PV power changes. In the afternoon, when solar irradiance begins to decrease, the load-managing system can disconnect vehicles from the PV array and connect them to the grid instead. Therefore, any vehicles not being charged by the PV array are still being charged.

However, this application of the grid-backed LMPV system would likely require several significant modifications. First, the terminals for each charging port would have to be modified to incorporate electric isolation between the EV and the PV array, such that the power can only flow from the PV array to the EVs and not from one EV to another. Second, the LMPV system would have to include voltage regulation to ensure the PV voltage is always greater than the voltage across the terminals of the EV battery. Lastly, the controller would also need to include some logic to determine the order in which the EVs are connected to the PV array. The EVs could be prioritized by their state-of-charge or by the time in which they were connected to the charging port. The system should also be able to handle fluctuation in the number of EVs available to be managed. In Chapter 3 and Chapter 4, it was assumed that each of the loads was always available to be connected to the PV array, which may not be the case for charging EVs. In practice, the total number of EVs available to the LMPV system would likely change throughout the day as new EVs arrive and the fully charged EVs depart.

Overall, while EV charging does contain many of the characteristics that are generally compatible with LMPV systems, there are additional challenges that may infringe upon the inherent benefits of using an LMPV system compared to a conventional PV system installation. In this case, even though an LMPV system can theoretically be

modified to support EV charging, the modifications may increase the cost of the system beyond the point at which an LMPV system would be more economical than a conventional PV system.

A similar application of charging storage batteries may be more practical because the number of batteries can be controlled, and the system does not have to account for human behaviors. The fully charged storage batteries can then be swapped out at night and replaced with empty batteries before any PV power is available the following day. Such a system could theoretically be applied to EVs as well if the EV battery packs were standardized and designed to be easily removed. In this case, instead of having the LMPV system charge the EVs directly, a stockpile of EV battery banks would be charged by the LMPV system. Then, the depleted EV battery banks would be swapped out with a fully charged battery bank upon arrival at the charging station. However, this approach would require significant coordination and standardization amongst EV manufacturers, making it less likely to be adopted.

5.2 PV-Powered Electrolysis

Electrolysis is widely used in the chemical and metallurgical industries for the production and purification of many raw materials that enable our modern society. Examples of electrowon or electro-refined materials include chlorine (Cl_2), hydrogen (H_2), and caustic soda (NaOH) by the chloralkali process from an aqueous sodium chloride (NaCl) solution, which produces about 70,000,000 tons/year of NaOH (Botte, 2014). The electricity required to produce 1 kg of NaOH is about 2.5 kWh/kg, translating into a total electricity consumption of about 1.65×10^8 MWh/year for the electrolysis. In addition,

aluminum (Al) by the Hall–Heroult process from aluminum oxide (Al2O3) dissolved in molten salt, which is produced at about 50,000,000 tons/year (Aluminium, 2020). The electricity required to produce 1 kg of Al is about 14 kWh/kg, resulting in total electricity consumption of about 6.12×10^8 MWh/year for the electrolysis.

Of all the electrowon or electro-refined materials detailed above, Hydrogen likely has the greatest potential for future growth in demand due to its ability to be used as a fuel source for fuel-cells or hydrogen internal combustion engines. Therefore, the application of hydrogen production through electrolysis was selected for additional analyses, as detailed in (Azzolini, Tao *et al.*, 2020).

5.2.1 Motivation for PV-Driven Hydrogen Production

The demand for hydrogen is growing rapidly due to its potential use as a zero-emission fuel source and energy storage medium. Hydrogen fuel cells can already convert chemical energy to electrical energy at efficiencies up to 60% with the only byproduct being water (USDOE, 2020). Electric motors coupled with fuel cells are also 2-3x more efficient than an internal combustion engine running on gasoline ("Hydrogen basics," 2020).

However, nearly all the hydrogen being produced today relies on fossil fuels. In the United States, 95% of hydrogen is produced via the steam-methane reforming of natural gas ("Hydrogen production: Natural gas reforming," 2020). Globally, the production of hydrogen is responsible for 830 million tons of CO_2 per year (*The future of hydrogen*,

2019). Therefore, to truly benefit from the use of hydrogen, it must be produced from renewable energy resources.

One promising method for hydrogen production is through the electrolysis of water—a process that can be powered by renewable energy resources like photovoltaics. While the costs associated with this form of hydrogen production has been a major obstacle, certain geographic regions are becoming economically viable locations for low-cost hydrogen production due to the declining costs of PV (*The future of hydrogen*, 2019).

To further reduce the costs associated with hydrogen production through water electrolysis, an LMPV system can be implemented that eliminates the need for power electronic devices. The load-management approach provides maximum power point tracking and voltage regulation, typically provided by costly power electronics, by controlling the loads connected to the PV array throughout the day. In other words, the LMPV system can accomplish the same tasks conventionally performed by power electronic devices but at a reduced cost. Depending on the desired amount of hydrogen to be produced, a stand-alone or grid-backed LMPV system can be implemented. The grid-backed LMPV system would still utilize the maximum available energy from the PV array throughout the day but would allow for continuous production of hydrogen even during the nighttime hours if so desired.

The load-management approach is particularly well-suited to drive water electrolysis for hydrogen production. Electrolysis requires DC power, can accept a relatively wide range of voltages, and can tolerate intermittent access to power. These attributes are all synergistic with the characteristics of PV-derived electricity, even in an

off-grid setting. Moreover, converting an electrolyzer to operate in the proposed manner only requires some rewiring, as depicted in Figure 5.2.

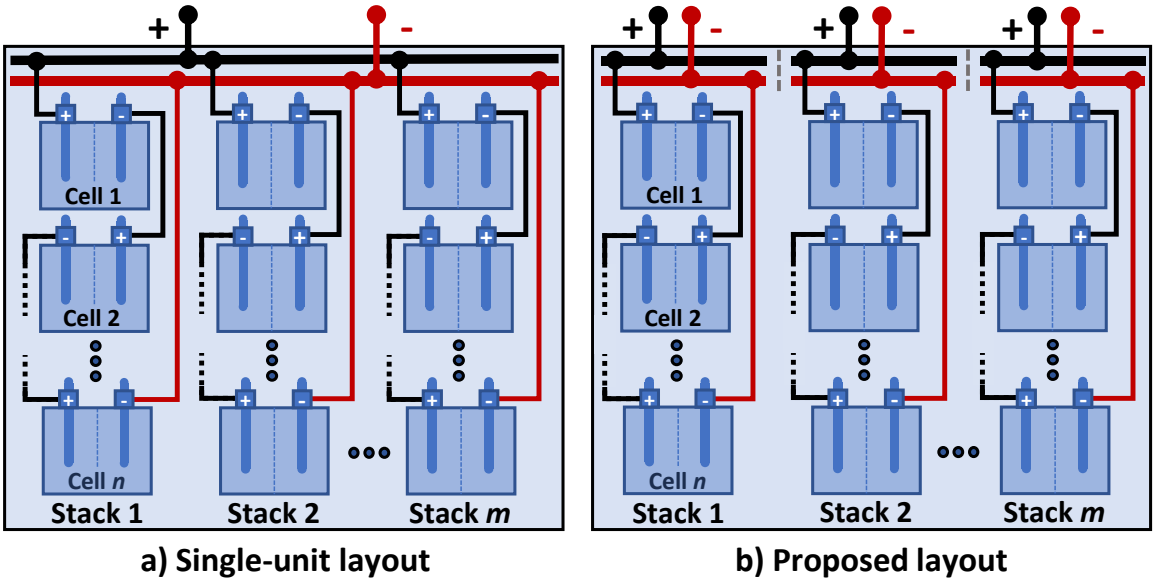

Figure 5.2. Conceptual Diagram for Operating the Electrolyzer as a Single Unit (a) or Using the Proposed Method (b).

Instead of conventionally operating the electrolyzer as a single unit, power is supplied to each electrolytic stack independently in response to changes in available PV power. Therefore, the load-managing system can be retrofitted to existing electrolyzers.

5.2.2 Electrolyzer Modeling

As depicted in Figure 5.2, an electrolyzer typically contains several parallel-connected "stacks," each of which contains a string of series-connected electrolytic cells. For this work, the Nel Hydrogen M200 and M400 PEM electrolyzers were selected. The M200 model contains 4 electrolyzer stacks with 100 electrolytic cells per stack (i.e., n = 100 and m = 4 in Figure 5.2), and each cell has an electrode surface area of 680 cm^2. The

M400 model contains 8 stacks with 100 cells per stack (i.e., n = 100 and m = 8 in Figure 5.2), and each cell has an electrode area of 680 cm^2. The polarization curve of a single electrolytic cell was obtained from Nel Hydrogen, following equation (7):

$$V = V_{on} + J \times R_i \tag{7}$$

where V is the voltage, J the current density, V_{on} the voltage threshold, and R_i the specific resistance of the cell. Fitting the data provided by Nel Hydrogen in Figure 5.3 reveals that V_{on} = 1.556 V and R_i = 0.2138 Ω-cm^2, with an R^2 value of 0.99848.

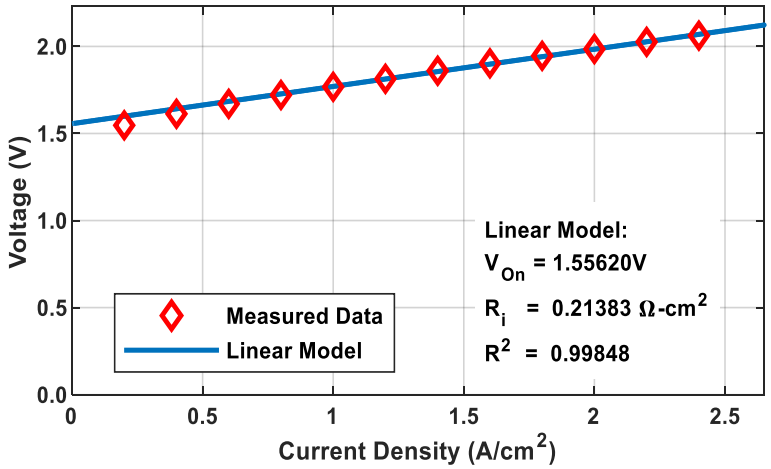

Figure 5.3. Linear Model of an Electrolytic Cell Derived from Measurements of a Typical Cell Used in the M200 Electrolyzer.

Using the fitting data from Figure 5.3, each of the stacks for the M200 and M400 electrolyzers were individually modeled, as shown in Figure 5.4. In this figure, the top lines represent the power-voltage relationship when all 4 stacks of the M200 and all 8 stacks of the M400, respectively, are connected in parallel, i.e., when the electrolyzer is operated as a single unit. When the electrolyzer is operated using the load-management approach, the system can operate on any parallel combination of stacks depending on the available PV power.

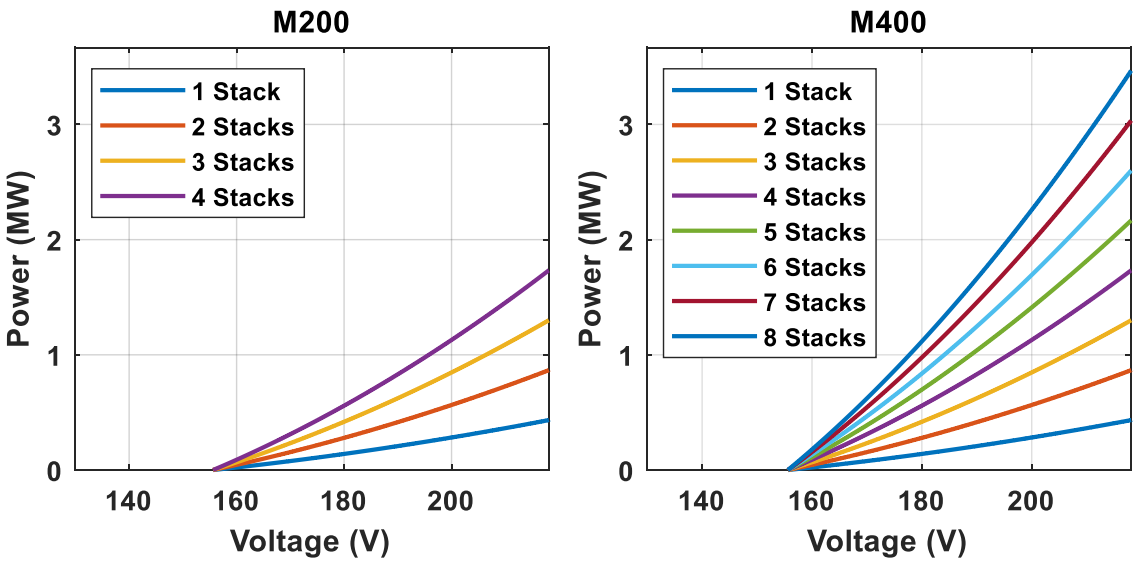

Figure 5.4. Relationship between Power and Voltage of Various Configurations of the M200 Electrolyzer.

The voltage threshold of an electrolyzer stack is equal to the sum of all its series-connected electrolytic cells. Since the M200 and M400 both have 100 cells per stack, the voltage threshold for both models is equal to 155.6 V. This threshold voltage can also be observed in Figure 5.4, where no power is consumed at voltages below 155.6 V. The only difference is that the M400 has twice as many stacks as the M200 model, so the total power required by the M400 is also twice as much as the M200 model.

5.2.3 PV Module Selection

Before the PV array can be modeled, the PV module must be selected according to the specifications of the electrolyzer. The most critical specification of the electrolyzer to consider is the voltage requirement. Electrolytic cells have a voltage threshold needed to activate the electrochemical reaction that produces hydrogen. In addition to the voltage

threshold value, Nel Hydrogen also provided a recommended voltage range and maximum voltage limit for the electrolyzer stacks. For both the M200 and M400 models, the manufacturer suggested an optimal operating range of 200 V to 210 V per stack and a limit of 260 V per stack.

The PV module database provided through NREL's SAM tool (Blair, DiOrio *et al.*, 2018) was used for selecting an appropriate PV module to power the M200 and M400 electrolyzers. The database was filtered to consider only 60-cell silicon modules from the top PV manufacturers. Any module that could not result in a maximum power point voltage within the suggested operating range of the electrolyzers was also disqualified. Ultimately, the Jinko JKM240P-60 module was chosen as it met all the criteria above.

5.2.4 PV Array and Irradiance Modeling

Since the voltage requirements were the same for both of the electrolyzers, the number of PV modules per string was also the same for both electrolyzers; only the number of parallel PV strings per array and total PV array power varied. The full PV array for the M200 electrolyzer consisted of 7 modules per string and 908 strings in parallel, resulting in a nominal output power of 1.527 MW_p, a maximum power point voltage of 210 V, and a maximum power point current of 7.273 kA. The full PV array for the M400 electrolyzer consisted of 7 modules per string and 1,815 strings in parallel, resulting in a nominal output power of 3.053 MW_p, a maximum power point voltage of 210 V, and a maximum power point current of 14.54 kA.

Using the PV_Lib toolbox developed by Sandia National Laboratories (Stein, 2012), the PV arrays were modeled and analyzed in MATLAB under a variety of atmospheric conditions. It was assumed that the PV arrays were located in Phoenix, Arizona with a tilt angle of 33.42° (equal to the latitude angle of the site) and an azimuth angle of 180°. A clear-sky irradiance profile was calculated for the site's location on 06/21/2019 (summer solstice) and translated to the plane-of-array (POA) irradiance for the tilted surface. The temperature was assumed to be at a constant 25°C resulting in a maximum incident irradiance of 952 W/m^2 on that day.

Figure 5.5 shows the current-voltage and power-voltage relationships of the simulated PV arrays for the maximum irradiance experienced on 06/21/2019. It can be observed that the maximum power reached by both PV arrays on that day was slightly less than their corresponding nameplate power ratings due to the difference in irradiance; the PV array ratings are based on 1000 W/m^2 compared to the maximum POA irradiance of 952 W/m^2 on 06/21/2019.

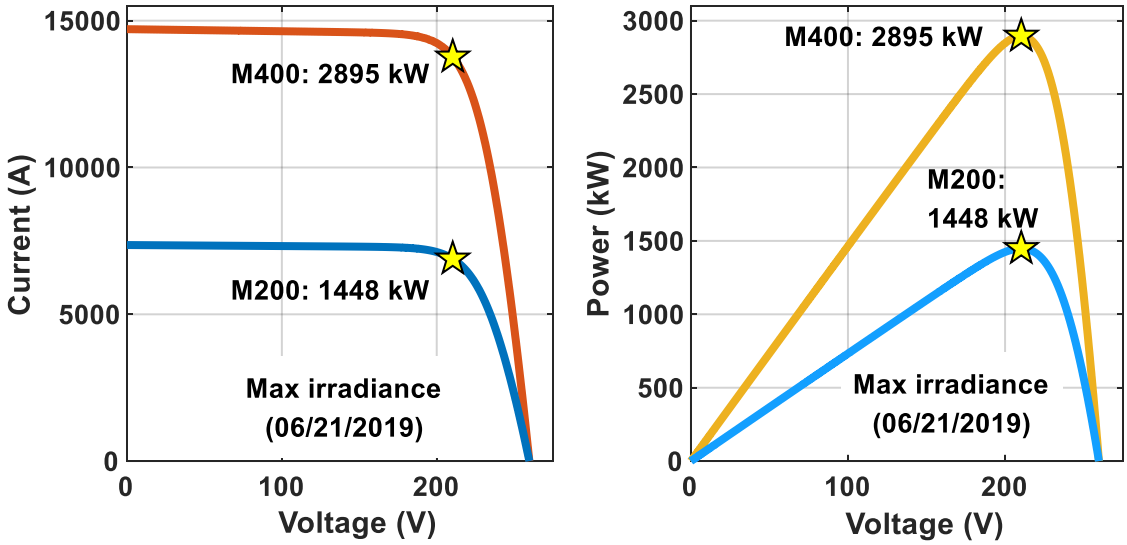

Figure 5.5. Current-voltage Plot (Left) and Power-voltage Plot (Right) of the Simulated PV Array under Maximum Irradiance on June 21st, 2019 Each with a Star to Highlight the Maximum Power Point.

5.2.5 M200 Simulation Results

The irradiance profile described in Chapter 5.2.4 was used to determine the maximum power available from the PV arrays throughout the day of 06/21/2019. Using those results as a baseline, additional simulations were conducted with the proposed system to determine its performance when powering each of the electrolyzer stacks individually. Since the load-managing system can supply power to each electrolyzer stack independently, a simulation was conducted to determine all the potential operating points of the system throughout the day on 06/21/2019. The results of this simulation are presented in Figure 5.6.

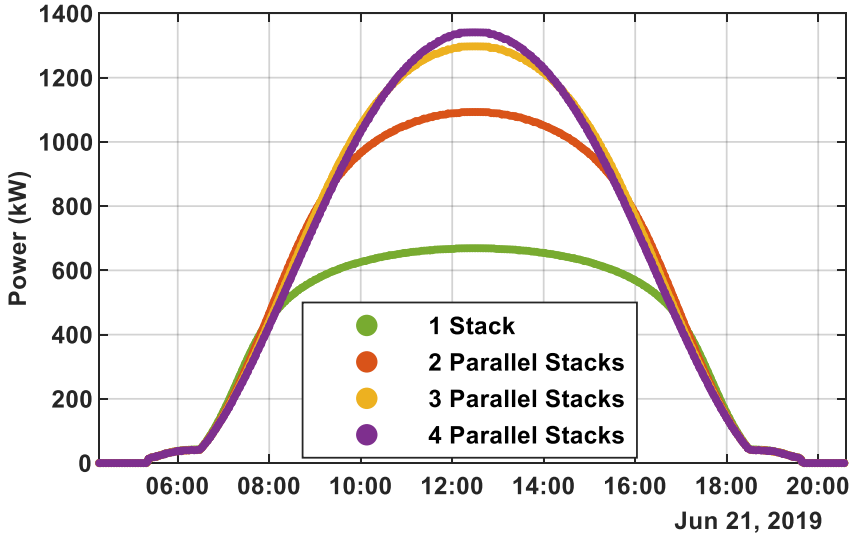

Figure 5.6. All Potential Operating Points for Each of the 4 Electrolyzer Stacks of the M200 Electrolyzer.

The optimal operating points of this system were then found by taking the maximum value at each time point for the results in Figure 5.6. In Figure 5.7, the optimal operating points are plotted alongside the maximum available power from the baseline simulation. The energy yield of 99.5% in Figure 5.7 was achieved without using a conventional MPPT or any power converters. The energy yield was quantified by comparing the delivered energy to the total available energy throughout the day using (3).

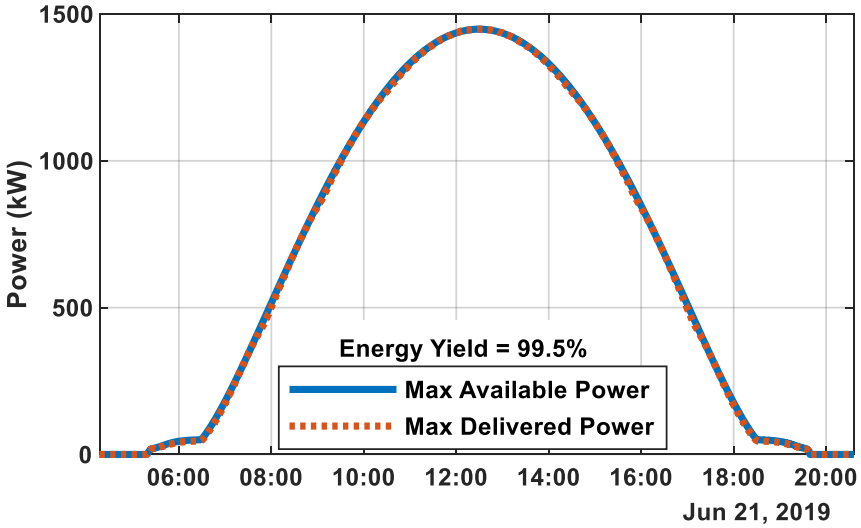

Figure 5.7. Optimal Operating Points of the Proposed System Compared to Maximum Available Power throughout the Day.

Figure 5.7 shows that even with just 4 stacks available to be managed, the energy yield of the system was above 99%. In contrast, most PV inverters have peak efficiencies of 95% to 98% (Pearsall, 2017); when taking into account inverter efficiencies over their range of expected operating conditions (i.e., their weighted efficiencies), the overall inverter efficiencies are further reduced. Also, inverters output AC electricity that would have to be converted back to DC to power the electrolyzers, introducing even more power loss into the system. Therefore, the proposed approach provides a significant improvement in energy yield compared to implementing a conventional inverter-based PV system design. Compared to the results of powering 4 purely resistive loads with the load-managing system presented in (Azzolini & Tao, 2018) that had an energy yield of 97.12%, the 4 electrolyzer stacks had an improved energy yield (with an absolute change of +2.38%) due to the proximity of their power-voltage curves to the actual P_{MP} values. Thus, the results in Figure 5.7 indicate that the load characteristics of the electrolytic stacks are better suited to the LMPV system than ohmic loads.

Figure 5.8 presents an alternative means for analyzing the simulation results by plotting the optimal operating points (in red) and the actual maximum power points (P_{MP}) of the PV array (in black) on top of the power-voltage curves of the M200 electrolyzer stacks (from Figure 5.4) and PV array curves. The power-voltage curves of the PV array in the background depict how this relationship shifts upward as irradiance increases. Overall, Figure 5.8 shows that the number of electrolyzer stacks being powered must change throughout the day to track the maximum power point since the optimal operating points appear on each of the 4 combinations of parallel stacks.

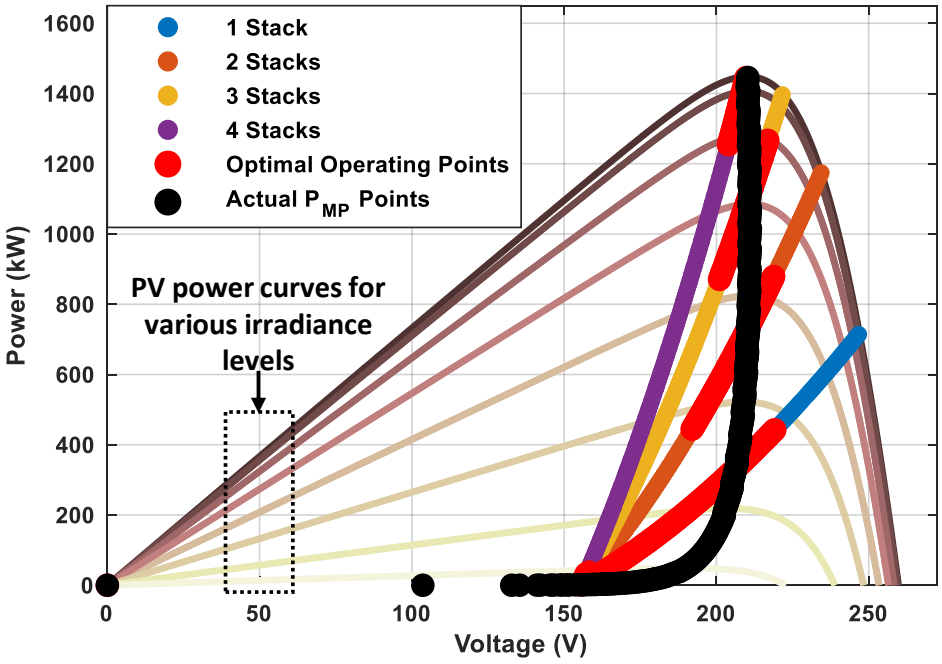

Figure 5.8. Optimal Operating Points (Red) and Actual Maximum Power Points (Black) for the Power-voltage Curves of both the Electrolyzer and PV Array.

Figure 5.9 presents the time-series results of the voltages applied to the electrolyzer stacks throughout the day, corresponding to the operating points in Figure 5.7. It can be observed that each time an additional stack was connected to the PV array throughout the

morning, there was a discrete reduction in the voltage; the opposite was also true in the afternoon when the stacks were disconnected from the PV array.

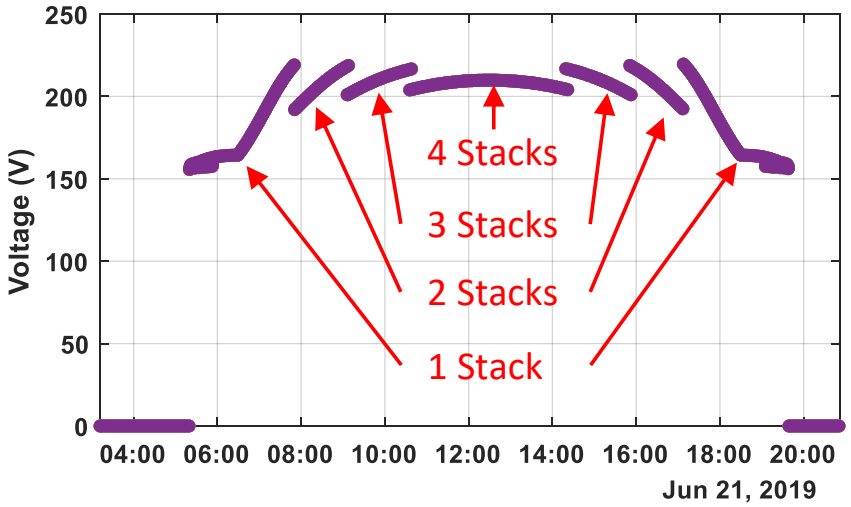

Figure 5.9. Voltage Time-series for the Simulation of the M200 Electrolyzer.

Figure 5.10 presents the same voltage results from Figure 5.9 but as a histogram to show the amount of time spent at each of the voltage levels. Only the lowest bin in the histogram, with edges of 154 V to 156 V, contained voltage values less than the voltage threshold of the electrolyzer, accounting for just 0.11% of the time the PV array was producing power. In other words, the electrolyzer was producing hydrogen for 99.89% of the time that the PV array was producing power. Figure 5.10 also shows that the applied voltages are well below the maximum limit of 260 V. For most of the day, the voltage was either within or just above the optimal range of 200 V to 210 V recommended by Nel Hydrogen.

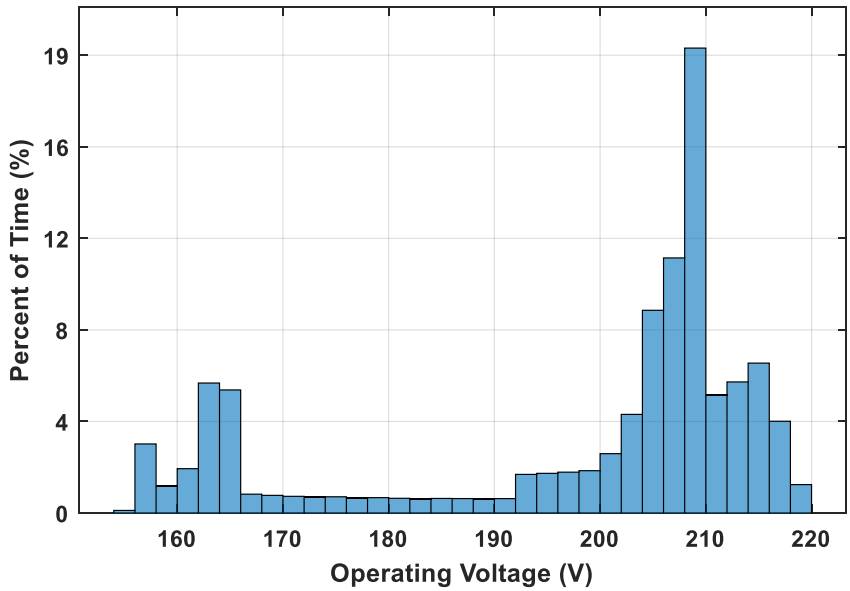

Figure 5.10. Histogram of Operating Voltages Applied throughout the Day for Optimal Operating Points of the Proposed System.

In Figure 5.2, it was shown that power can be supplied to an electrolyzer operating as a single unit or supplied to each stack independently using the proposed approach. When operating the electrolyzer as a single unit, a conventional PV system design could be implemented that utilizes an inverter (with MPPT functionality) and an AC/DC rectifier to power the electrolyzer, but this approach was already determined to underperform the proposed approach. Another alternative would be to implement a direct-coupled PV system (without any MPPT or voltage regulation).

For the case of implementing a direct-coupled PV system, the M200 electrolyzer would be operated as a single unit, where all 4 stacks of the electrolyzer would always remain connected to the PV array, i.e., there would be no load management. To compare the performance of this direct-coupled PV system to the proposed load-management approach, the same PV array (from Figure 5.5) was simulated for the M200 electrolyzer on

06/21/2019. The results of this simulation are presented in Figure 5.11, where the energy yield of the system was found to be 96.9%.

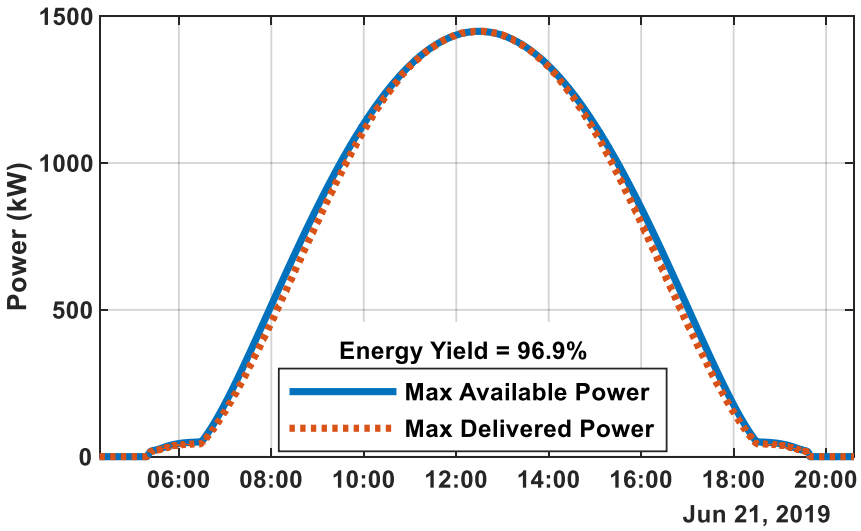

Figure 5.11. Optimal Operating Points of the Direct-coupled System for Powering the M200 Electrolyzer as a Single Unit Compared to Maximum Available Power.

The results in Figure 5.11 show that the energy yield of the direct-coupled system was less than that of the proposed system, with an absolute reduction of –2.52%. Therefore, the proposed load-management approach provided a greater energy yield than both the conventional power electronics-based PV system and the direct-coupled PV system.

Another advantage of the load-management approach for powering the M200 electrolyzer is that the applied voltages were more closely aligned with the optimal operating range provided by the manufacturer. While the applied voltages of the direct-coupled system, shown in Figure 5.12, were still within the acceptable range, the voltage spent significantly less time in the optimal 200 V to 210 V range compared to Figure 5.10.

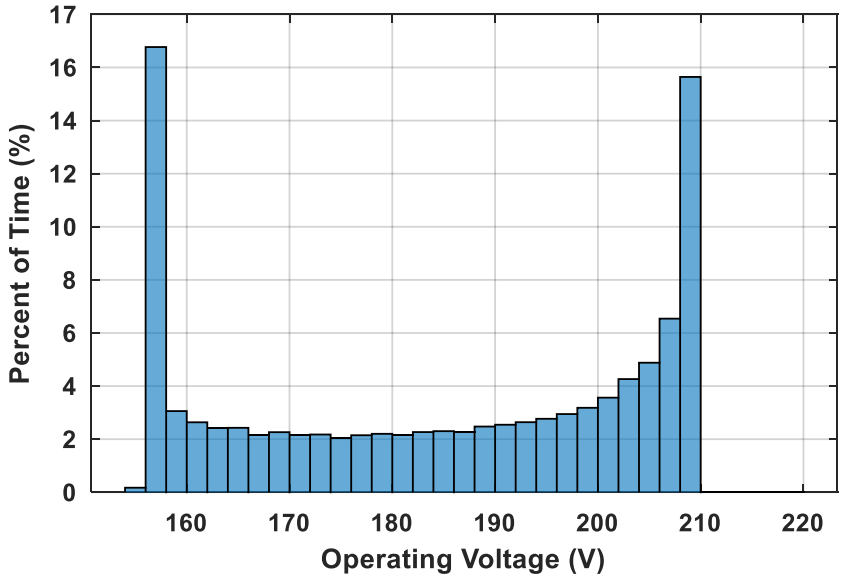

Figure 5.12. Histogram of Operating Voltages Applied throughout the Day to the M200 Electrolyzer, Operated as a Single Unit for the Direct-coupled System.

5.2.6 M400 Simulation Results

The simulations conducted on the M200 electrolyzer were repeated for the M400 electrolyzer. In these simulations, the proposed system had 8 stacks to manage throughout the day compared to the 4 stacks available for the M200 electrolyzer. Therefore, operating the M400 electrolyzer with the proposed load-management approach provided twice as many potential operating points than the M200 system, as shown in Figure 5.13.

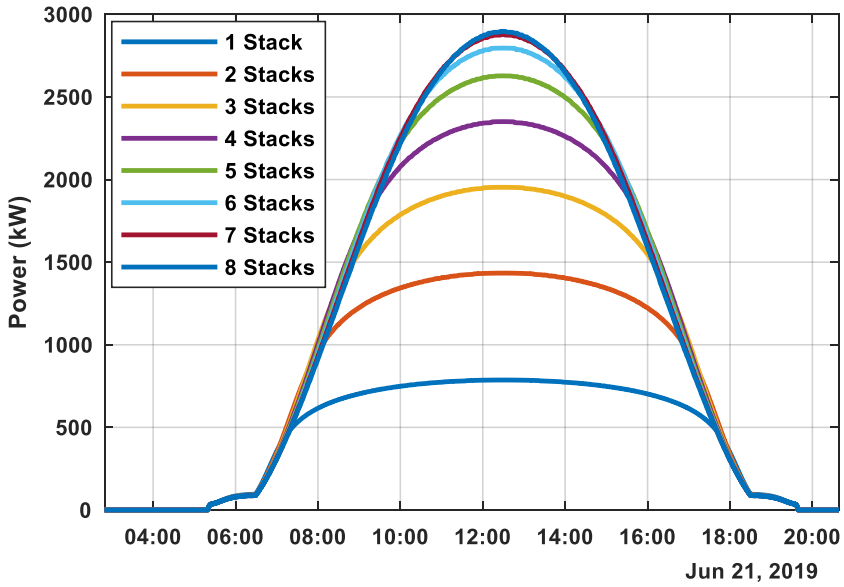

Figure 5.13. All Potential Operating Points for each of the 8 Electrolyzer Stack Combinations of the M400 Electrolyzer.

With more potential operating points, the proposed system resulted in an energy yield of 99.8%, as shown in Figure 5.14, when applied to the M400 electrolyzer compared to the energy yield of 99.5% when applied to the M200 electrolyzer. However, since the energy yield for the M200 system was already close to 100%, the absolute improvement in energy yield was only +0.36%. This result suggests that there is not much of an incentive to scale up the system since doubling the number of electrolyzer stacks only provided a marginal increase in energy yield.

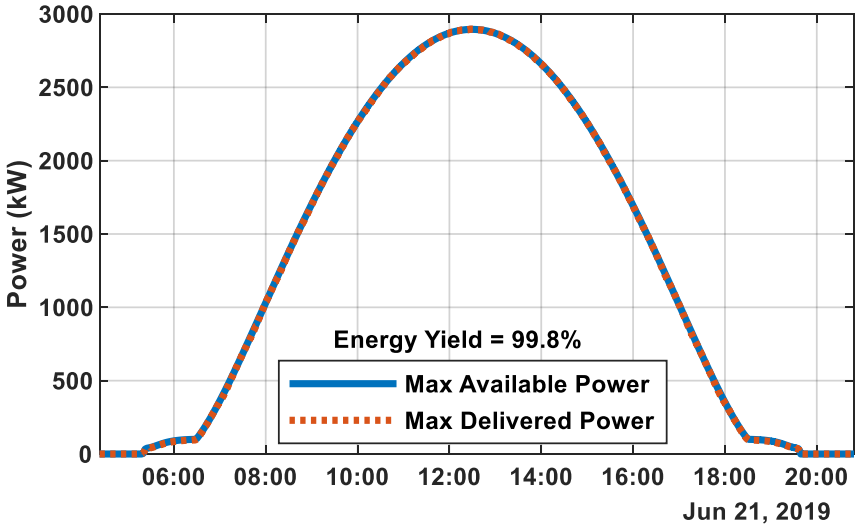

Figure 5.14. Optimal Operating Points of the Proposed System for Powering the M400 Electrolyzer Compared to Maximum Available Power.

The voltage performance of the M400 system was also comparable to that of the M200 system, as seen in Figure 5.15. The operating voltage of the system remained within or just above the optimal range for the majority of the day and never exceeded the 260 V limit. Similar to the M200 system, the M400 system was producing hydrogen for nearly the entire duration for which the PV array was producing power; only the lowest bin in the histogram contained voltage values less than the voltage threshold of the electrolyzer.

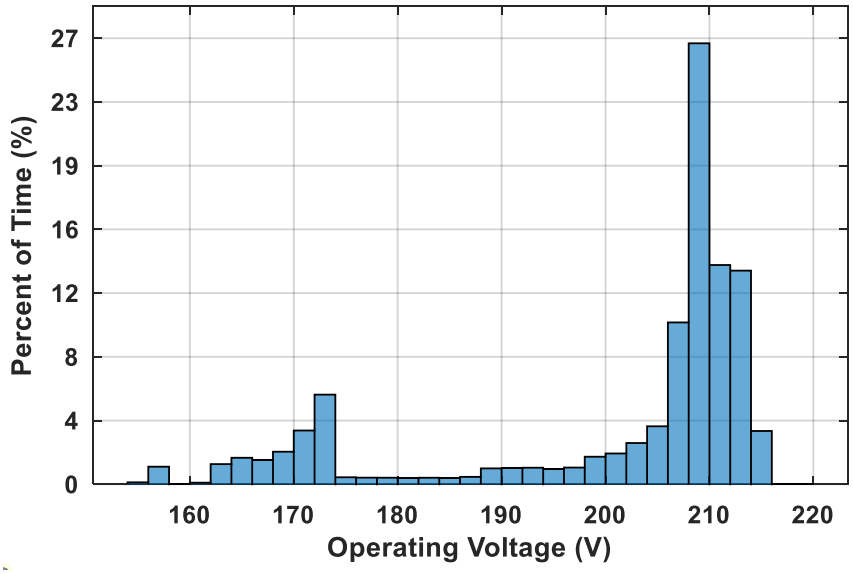

Figure 5.15. Histogram of Optimal Operating Voltages Applied throughout the Day to the M400 Electrolyzer with the Proposed System.

An additional experiment was conducted to investigate the performance of a direct-coupled PV system approach for the M400 electrolyzer, operating the electrolyzer as a single unit without load management, using the same PV array as in Figure 5.5. The results from this simulation revealed that the energy yield dropped to 96.9%, representing an absolute reduction in energy yield of –2.88% compared to using the load management approach. Overall, the LMPV approach provided a greater energy yield than both the conventional power electronics-based PV system and the direct-coupled PV system.

5.2.7 Discussion of Simulation Results

The simulation results in Chapter 5.2.5 and Chapter 5.2.6 revealed that an LMPV system could be implemented to drive commercially available electrolyzers for hydrogen production. By simply rewiring the terminals of the electrolyzer to allow the LMPV system to control the flow of power to each of the four electrolytic stacks independently, the system

was able to track the maximum power point of the PV array throughout the day, resulting in energy yields of 99.5% and 99.8% for the M200 and M400 electrolyzers, respectively. The proposed method performs maximum power point tracking by controlling the number of electrolyzer stacks connected to the PV array throughout the day without the use of any power electronics, reducing both the cost of the system and the power losses.

The proposed system was applied to two different Nel Hydrogen PEM electrolyzers, one with 4 stacks (M200) and one with 8 stacks (M400), resulting in energy yields of 99.5% and 99.8%, respectively. The energy yield of the M200 system with 4 stacks represented an absolute increase of 2.38% compared to an LMPV system powering 4 ohmic loads. The energy yields of both the M200 and M400 systems represented a significant improvement over conventional power electronics-based PV systems that require inverters with peak efficiencies of 95% to 98% and require additional AC/DC rectifiers to be compatible with the production of hydrogen through electrolysis. The load-management approach also resulted in an absolute energy yield increase of +2.88% when compared to the implementation of a direct-coupled PV system to power the electrolyzers as a single unit. The load-management approach was able to maintain the operating voltages of the electrolyzers within the acceptable range without ever exceeding the maximum voltage limit. Furthermore, the majority of the voltages applied to the electrolyzers were within the optimal range recommended by the manufacturer.

Overall, the results presented in this chapter support the viability of implementing a load-management approach for driving hydrogen production with photovoltaics. The LMPV system was found to provide a greater energy yield than both power electronics-

based PV systems and direct-coupled PV systems while maintaining the electrolyzer operating voltage within the acceptable range. Since the LMPV system does not require any power electronics, the cost of the system would be significantly less than a conventional PV system. Given promising simulation results and minimal modifications required, there is significant potential for the LMPV system to reduce the energy costs and carbon footprints associated with the production of hydrogen and other raw materials outlined in Chapter 5.2.

6 FUTURE WORK

The results from the hardware implementations of the LMPV system, along with the modeling and analysis of the hydrogen production application, provide abundant evidence of the potential for LMPV systems to reduce the costs of photovoltaic-derived electricity for various applications. Throughout the analyses of the simulation and hardware results, several paths for future work were identified that could improve both the performance and analysis of the system.

The ability to accurately determine the optimal P_{SP} values for each of the loads being managed by the LMPV system is directly related to the overall energy yield of the system, as inaccurate P_{SP} values can cause the system to under-utilize the power available from the PV array. There are several ways in which the determination of optimal P_{SP} values can be improved.

First, the signal chains of the voltage and current measurements can be modified to reduce the level of noise in the signal by pairing each sensor with a dedicated ADC. Not only does digitizing the signal earlier provide more resilience to noise, but the input range of each ADC can also be optimized for each sensor, as opposed to using an off-the-shelf DAQ to handle multiple analog input signals. By improving the signal-to-noise ratio of the voltage and current measurements, the software-defined time-delays can be removed, which improves the response time, and thus the accuracy, of the load-matching MPPT control algorithm.

Second, the load-matching MPPT control algorithm can also be improved. Through the analysis of the simulation and hardware results, it was determined that the optimal P_{SP}

values are negatively correlated with the operating temperature of the PV array. Therefore, if the temperature values were being measured and stored, the load-matching MPPT algorithm would be able to correct the P_{SP} values for each of the loads as the temperature changed over time, which would likely result in fewer unsuccessful control actions. Also, other more sophisticated MPPT algorithms, like the IncCond method or genetic optimization algorithms, could be modified and implemented with the framework of the load-matching MPPT algorithm to improve its performance as well.

The load-matching MPPT controller could be modified to provide regulation of the PV output voltage, which may be required by certain applications. Being that the controller already has access to the voltage measurements of the PV array, the voltage regulation capability can be implemented as a software upgrade without requiring any additional hardware components. For example, the code within the algorithm that is used to determine if a control action was successful can be modified to also check if the output voltage is within the acceptable range for the application.

The experimental set up for the hardware implementation of the LMPV system can also be modified to validate the application of hydrogen production. Instead of using variable resistors as the loads, an equivalent electrical model of an electrolyzer can be implemented. As discussed in Chapter 5.2.2, the loading characteristics of an electrolyzer are determined by its internal resistance and its turn-on voltage. Therefore, a Zener diode can be used to provide the turn-on voltage and a resistor can be placed in series to represent the internal resistance of the electrolytic cell. This electrically-equivalent model can be combined several times in series to represent a stack of electrolytic cells. The load-

matching MPPT algorithm would then control the flow of power to each "stack" independently, as was done in simulation.

The analysis of the results from the hardware implementation of the LMPV system could also benefit from a comparison to a conventional PV system that has a power electronics-based MPPT. Several identical PV modules, or PV modules with very similar characteristics, could be installed side by side where one module would be connected to a conventional PV system (with an off-grid or grid-tied inverter) and the other would be connected to the LMPV system, as shown in Figure 6.1.

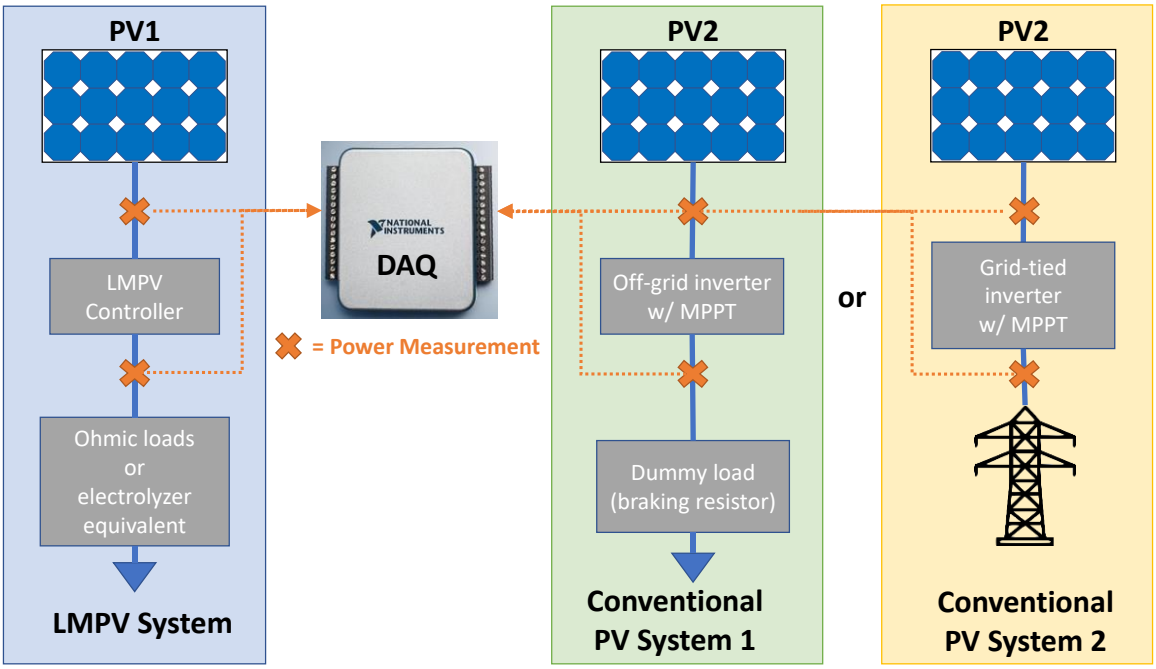

Figure 6.1. Proposed Experimental Setup to Compare the Energy Yield of the LMPV System to a Conventional PV System

At the end of the day, the energy yields from the two systems could be compared and the results could be extrapolated to estimate the performance on full-sized PV arrays. The experimental setup in Figure 6.1 would also allow for the efficiency of the inverter to

be calculated since power is being measured on either side. Other inverter metrics could be determined as well, such as the amount of energy under-utilized by the inverter due to clipping or due to the PV power required for the inverter to turn on. The module to which each system is connected could also be switched each day to adjust for any differences in energy yield due to the underlying PV module characteristics. In addition, this experimental setup would provide a quantitative basis for future techno-economic analyses.

7 CONCLUSION

Through extensive modeling, simulation, and analyses the LMPV system was shown to have significant benefits over conventional PV systems for many practical applications. In Chapter 3, the fundamental components of an LMPV system were presented as well as the concept of performing maximum power point tracking and voltage regulation through load-matching. The LMPV system was modeled in MATLAB to quantify the theoretical energy yield of the system under a variety of different system parameters. It was revealed that the energy yield of the LMPV system increases with the number of loads being managed and that over 99% of the energy from the PV array can be extracted when the system was managing just 8 ohmic loads of equal resistance. Furthermore, it was shown that the LMPV system could perform voltage regulation, whereby the effect on the theoretical energy yield of the system was minimized as more loads were being managed by the system.

The first hardware implementation of the LMPV system utilized a photodetector-based control system to perform the load-matching MPPT functionality. For this iteration of the system, the photodetector provided an estimate of the maximum available power from the PV array throughout the day that was used by the controller to determine the optimal number of loads to connect to the PV array. The controller was able to successfully manage the loads connected to the PV array throughout the day and instantaneously respond to changes in irradiance due to cloud coverage. This initial hardware implementation of the LMPV system provided key insights into the performance of the system and highlighted practical challenges of the system, including the impact of temperature and the need for direct power measurements of the output PV power to ensure

the control actions were valid. The identification of these practical challenges led to the improved control algorithm presented in Chapter 4.

Instead of using a photodetector to estimate the maximum available power from the PV array throughout the day, a feedback-based control algorithm, similar to the P&O MPPT approach, was developed to correct for invalid control actions taken by the LMPV system. The improved load-matching MPPT control algorithm, presented in Chapter 4, was modeled in Simulink and testing under a variety of PV array operating conditions, such as variable irradiance and temperature profiles with multiple step-changes. By monitoring the output voltage and current of the PV array, the improved load-matching MPPT algorithm was able to correct for unsuccessful control actions and update its estimates of the optimal P_{SP} values for each of the loads throughout the day, resulting in a more robust LMPV system.

The improvements made to the LMPV control algorithm were tested in hardware to validate the simulation results. Current and voltage sensors were designed and fabricated on printed circuit boards to provide measurements of the actual PV array output power throughout the day. This second iteration of the LMPV system in hardware was tested and validated over multiple two-day experiments, which revealed that the load-matching MPPT algorithm was able to successfully learn the P_{SP} values of each of the loads regardless of when the experiment was initiated (either early morning or mid-afternoon) and regardless of the weather conditions (clear-sky or cloudy weather). Although the temperature varied significantly throughout each two-day experiment, the controller was able to track the changes in optimal P_{SP} values successfully.

In Chapter 5, several practical applications of the LMPV system were identified and discussed. The stand-alone LMPV system can be implemented for off-grid remote power applications, like irrigation and refrigeration systems, that are in high demand in many developing countries that lack widespread electricity access. The LMPV system can also be modified to incorporate a secondary power supply for applications that require constant access to power, like electric vehicle charging. One of the most compatible applications of the LMPV system, powering electrolytic processes, was explored in detail in Chapter 5 for the production of hydrogen through water electrolysis. The NEL Hydrogen M200 and M400 electrolyzers were modeled in MATLAB after being matched to corresponding PV arrays—the process for which was discussed in detail. The simulation results of the LMPV system for hydrogen production revealed that the energy yield of the system would exceed 99% when managing just 4 electrolytic stacks, which was an improvement over the simulation results for ohmic loads in Chapter 3.3.1. The LMPV system also outperformed the conventional power electronics-based PV system approach and the direct-coupled PV system approach.

This work explored the development and implementation of a novel load-managing PV system topology that includes the same critical functions of conventional PV systems, like an MPPT and voltage regulation capability, without the need for any power electronics. While this work analyzed the fundamental concepts and benefits of an LMPV system, future work is still needed in several key areas, such as improvements to the load-matching MPPT algorithm and a comparison of its performance to that of commercially available power electronics-based MPPTs. Overall, the LMPV system was shown to have significant potential for reducing the cost of PV-derived electricity for multiple practical applications.

REFERENCES

Ahmed, J., & Salam, Z. (2015). An improved perturb and observe (P&O) maximum power point tracking (MPPT) algorithm for higher efficiency. Applied Energy, 150, 97-108. doi:https://doi.org/10.1016/j.apenergy.2015.04.006

Aluminium, W. (2020). Primary aluminium production. Retrieved from http://www.world-aluminium.org/statistics/

Applebaum, J. (1987). The quality of load matching in a direct-coupling photovoltaic system. IEEE Transactions on Energy Conversion, EC-2(4), 534-541. doi:10.1109/TEC.1987.4765889

Armstrong, K. O., Das, S., & Cresko, J. (2016, 7-9 Nov. 2016). Wide bandgap semiconductor opportunities in power electronics. Paper presented at the 2016 IEEE 4th Workshop on Wide Bandgap Power Devices and Applications (WiPDA).

Atlam, O., Barbir, F., & Bezmalinovic, D. (2011). A method for optimal sizing of an electrolyzer directly connected to a PV module. International Journal of Hydrogen Energy, 36(12), 7012-7018. doi:https://doi.org/10.1016/j.ijhydene.2011.03.073

Azzolini, J. A., & Tao, M. (2018). A control strategy for improved efficiency in direct-coupled photovoltaic systems through load management. Applied Energy, 231, 926-936. doi:https://doi.org/10.1016/j.apenergy.2018.09.198

Azzolini, J. A., Tao, M., Ayers, K., & Vacek, J. (2020). A load-managing photovoltaic system for driving hydrogen production. Paper presented at the IEEE Photovoltaics Specialists Conference.

Benghanem, M., Daffallah, K. O., Joraid, A. A., Alamri, S. N., & Jaber, A. (2013). Performances of solar water pumping system using helical pump for a deep well: A case study for Madinah, Saudi Arabia. Energy Conversion and Management, 65, 50-56. doi:https://doi.org/10.1016/j.enconman.2012.08.013

Blair, N., DiOrio, N., Freeman, J., Gilman, P., Janzou, S., Neises, T., et al. (2018). System Advisor Model (SAM) general description (version 2017.9.5). Retrieved from https://www.nrel.gov/docs/fy18osti/70414.pdf

Boden, T. A., Andres, R. J., & Marland, G. (2017). Global, regional, and national fossil-fuel co2 emissions.

Botte, G. G. (2014). Electrochemical manufacturing in the chemical industry. Interface magazine, 23(3), 49-55. doi:10.1149/2.f04143if

Bowman, M. (2019). EIA projects that renewables will provide nearly half of world electricity by 2050. Retrieved from https://www.eia.gov/todayinenergy/detail.php?id=41533

Chandel, S. S., Naik, M. N., & Chandel, R. (2017). Review of performance studies of direct coupled photovoltaic water pumping systems and case study. Renewable and Sustainable Energy Reviews, 76, 163-175. doi:https://doi.org/10.1016/j.rser.2017.03.019

Clarke, R. E., Giddey, S., Ciacchi, F. T., Badwal, S. P. S., Paul, B., & Andrews, J. (2009). Direct coupling of an electrolyser to a solar PV system for generating hydrogen. International Journal of Hydrogen Energy, 34(6), 2531-2542. doi:https://doi.org/10.1016/j.ijhydene.2009.01.053

Daraban, S., Petreus, D., & Morel, C. (2014). A novel mppt (maximum power point tracking) algorithm based on a modified genetic algorithm specialized on tracking the global maximum power point in photovoltaic systems affected by partial shading. Energy, 74, 374-388. doi:https://doi.org/10.1016/j.energy.2014.07.001

EIA. (2019). Tracking power 2019. Retrieved from https://www.iea.org/reports/tracking-power-2019

EIA, U. S. (2020). What is U.S. electricity generation by energy source? Retrieved from https://www.eia.gov/tools/faqs/faq.php?id=427&t=3

Fu, R., Feldman, D., & Margolis, R. (2018). U.S. Solar photovoltaic system cost benchmark: Q1 2018. Retrieved from https://www.nrel.gov/docs/fy19osti/72399.pdf

The future of hydrogen. (2019). Retrieved from https://www.iea.org/reports/the-future-of-hydrogen

García-Valverde, R., Espinosa, N., & Urbina, A. (2011). Optimized method for photovoltaic-water electrolyser direct coupling. International Journal of Hydrogen Energy, 36(17), 10574-10586. doi:https://doi.org/10.1016/j.ijhydene.2011.05.179

Gibson, T. L., & Kelly, N. A. (2008). Optimization of solar powered hydrogen production using photovoltaic electrolysis devices. International Journal of Hydrogen Energy, 33(21), 5931-5940. doi:https://doi.org/10.1016/j.ijhydene.2008.05.106

Golnas, A. (2013). PV system reliability: An operator's perspective. IEEE Journal of Photovoltaics, 3(1), 416-421. doi:10.1109/JPHOTOV.2012.2215015

Green, M. A. (1982). Accuracy of analytical expressions for solar cell fill factors. Solar Cells, 7(3), 337-340. doi:https://doi.org/10.1016/0379-6787(82)90057-6

Hussein, K. H., Muta, I., Hoshino, T., & Osakada, M. (1995). Maximum photovoltaic power tracking: An algorithm for rapidly changing atmospheric conditions. IEEE Proceedings - Generation, Transmission and Distribution, 142(1), 59-64. doi:10.1049/ip-gtd:19951577

Hydrogen basics. (2020). Alternative Fuels Data Center. Retrieved from https://afdc.energy.gov/fuels/hydrogen_basics.html

Hydrogen production: Natural gas reforming. (2020). Retrieved from https://www.energy.gov/eere/fuelcells/hydrogen-production-natural-gas-reforming

Jiang, L. L., Maskell, D. L., & Patra, J. C. (2013). A novel ant colony optimization-based maximum power point tracking for photovoltaic systems under partially shaded conditions. Energy and Buildings, 58, 227-236. doi:https://doi.org/10.1016/j.enbuild.2012.12.001

Klise, G. T., Lavrova, O., & Gooding, R. (2018). PV system component fault and failure compilation and analysis. Retrieved from https://prod-ng.sandia.gov/techlib-noauth/access-control.cgi/2018/181743.pdf

Kolhe, M., Joshi, J. C., & Kothari, D. P. (2004). Performance analysis of a directly coupled photovoltaic water-pumping system. IEEE Transactions on Energy Conversion, 19(3), 613-618. doi:10.1109/TEC.2004.827032

Kou, Q., Klein, S. A., & Beckman, W. A. (1998). A method for estimating the long-term performance of direct-coupled PV pumping systems. Solar Energy, 64(1), 33-40. doi:https://doi.org/10.1016/S0038-092X(98)00049-8

Lave, M., & Kleissl, J. (2013). Cloud speed impact on solar variability scaling – application to the wavelet variability model. Solar Energy, 91(0), 11-21. doi:http://dx.doi.org/10.1016/j.solener.2013.01.023

Leibson, S. (2018). Fundamentals of current measurement: Part 1 - current sense resistors. Retrieved from https://www.digikey.com/en/articles/fundamentals-of-current-measurement-part-1-current-sense-resistors

Maeda, T., Ito, H., Hasegawa, Y., Zhou, Z., & Ishida, M. (2012). Study on control method of the stand-alone direct-coupling photovoltaic – water electrolyzer. International Journal of Hydrogen Energy, 37(6), 4819-4828. doi:https://doi.org/10.1016/j.ijhydene.2011.12.013

Maroufmashat, A., Sayedin, F., & Khavas, S. S. (2014). An imperialist competitive algorithm approach for multi-objective optimization of direct coupling photovoltaic-electrolyzer systems. International Journal of Hydrogen Energy, 39(33), 18743-18757. doi:https://doi.org/10.1016/j.ijhydene.2014.08.125

Mey, A. (2019). Average U.S. construction costs for solar generation continue to decrease. Retrieved from https://www.eia.gov/todayinenergy/detail.php?id=41153

Mokeddem, A., Midoun, A., Kadri, D., Hiadsi, S., & Raja, I. A. (2011). Performance of a directly-coupled PV water pumping system. Energy Conversion and Management, 52(10), 3089-3095. doi:https://doi.org/10.1016/j.enconman.2011.04.024

Nagarajan, A., Thiagarajan, R., Repins, I., & Hacke, P. (2019). Photovoltaic inverter reliability assessment. Retrieved from https://www.nrel.gov/docs/fy20osti/74462.pdf

Pattabiraman, D., Lasseter, R. H., & Jahns, T. M. (2018, 5-10 Aug. 2018). Comparison of grid following and grid forming control for a high inverter penetration power system. Paper presented at the 2018 IEEE Power & Energy Society General Meeting (PESGM).

Pearsall, N. M. (2017). 1 - introduction to photovoltaic system performance. In N. Pearsall (Ed.), The performance of photovoltaic (PV) systems (pp. 1-19): Woodhead Publishing.

Radjai, T., Rahmani, L., Mekhilef, S., & Gaubert, J. P. (2014). Implementation of a modified incremental conductance MPPT algorithm with direct control based on a fuzzy duty cycle change estimator using DSpace. Solar Energy, 110, 325-337. doi:https://doi.org/10.1016/j.solener.2014.09.014

Ram, J. P., Babu, T. S., & Rajasekar, N. (2017). A comprehensive review on solar PV maximum power point tracking techniques. Renewable and Sustainable Energy Reviews, 67, 826-847. doi:https://doi.org/10.1016/j.rser.2016.09.076

Roston, E. (2016). Electric cars can help clean up the grid. Retrieved from https://www.bloomberg.com/news/articles/2016-04-29/electric-cars-can-help-clean-up-the-grid

Santhoshi, B. K., Sundaram, K., M., Padmanaban, S., Holm-Nielson, J. B., & Prabhakaran, K. K. (2019). Critical review of PV grid-tied inverters. Energies, 12(10). doi:https://doi.org/10.3390/en12101921

Sayedin, F., Maroufmashat, A., Sattari, S., Elkamel, A., & Fowler, M. (2016). Optimization of photovoltaic electrolyzer hybrid systems; taking into account the effect of climate conditions. Energy Conversion and Management, 118, 438-449. doi:https://doi.org/10.1016/j.enconman.2016.04.021

Stein, J. S. (2012, 3-8 June 2012). The photovoltaic performance modeling collaborative (PVPMC). Paper presented at the 2012 38th IEEE Photovoltaic Specialists Conference.

Su, Z., Ding, S., Gan, Z., & Yang, X. (2016). Analysis of a photovoltaic-electrolyser direct-coupling system with a v-trough concentrator. Energy Conversion and Management, 108, 400-410. doi:https://doi.org/10.1016/j.enconman.2015.10.078

Sundareswaran, K., Peddapati, S., & Palani, S. (2014). Mppt of PV systems under partial shaded conditions through a colony of flashing fireflies. IEEE Transactions on Energy Conversion, 29(2), 463-472. doi:10.1109/TEC.2014.2298237

Syafaruddin, Karatepe, E., & Hiyama, T. (2009). Artificial neural network-polar coordinated fuzzy controller based maximum power point tracking control under partially shaded conditions. IET Renewable Power Generation, 3(2), 239-253. doi:10.1049/iet-rpg:20080065

Tiwari, A. K., & Kalamkar, V. R. (2016). Performance investigations of solar water pumping system using helical pump under the outdoor condition of Nagpur, India. Renewable Energy, 97, 737-745. doi:https://doi.org/10.1016/j.renene.2016.06.021

USDOE. (2020). Fuel cells. Retrieved from https://www.energy.gov/eere/fuelcells/fuel-cells

Wang, Y., Ji, J., Sun, W., Yuan, W., Cai, J., Guo, C., et al. (2016). Experiment and simulation study on the optimization of the PV direct-coupled solar water heating system. Energy, 100, 154-166. doi:https://doi.org/10.1016/j.energy.2016.01.022

Wasynezuk, O. (1983). Dynamic behavior of a class of photovoltaic power systems. IEEE Transactions on Power Apparatus and Systems, PAS-102(9), 3031-3037. doi:10.1109/TPAS.1983.318109

World-Bank. (2020). Off-grid solar market trends report. Retrieved from https://www.lightingglobal.org/wp-content/uploads/2020/03/VIVID%20OCA_2020_Off_Grid_Solar_Market_Trends_Report_Full_High.pdf

Yeong-Chau, K., Tsorng-Juu, L., & Jiann-Fuh, C. (2001). Novel maximum-power-point-tracking controller for photovoltaic energy conversion system. IEEE Transactions on Industrial Electronics, 48(3), 594-601. doi:10.1109/41.925586